T.R.
GEBZE TECHNICAL UNIVERSITY
GRADUATE SCHOOL OF NATURAL AND APPLIED SCIENCES

DESIGN AND IMPLEMENTATION OF MAGNETIC PARTICLE IMAGING (MPI) SCANNER FOR MEDICAL APPLICATIONS

MUHAMMAD IRFAN
A THESIS SUBMITTED FOR THE DEGREE OF
DOCTOR OF PHILOSOPHY
DEPARTMENT OF ELECTRONICS ENGINEERING

GEBZE
2021

T.R.
GEBZE TECHNICAL UNIVERSITY
GRADUATE SCHOOL OF NATURAL AND APPLIED SCIENCES

DESIGN AND IMPLEMENTATION OF MAGNETIC PARTICLE IMAGING (MPI) SCANNER FOR MEDICAL APPLICATIONS

MUHAMMAD IRFAN
A THESIS SUBMITTED FOR THE DEGREE OF
DOCTOR OF PHILOSOPHY
DEPARTMENT OF ELECTRONICS ENGINEERING

THESIS SUPERVISOR
ASSOC. PROF. DR. FUAD ALIEW
II. THESIS SUPERVISOR
ASSOC. PROF. DR. AYHAN BINGOLBALI

GEBZE
2021

T.C.
GEBZE TEKNİK ÜNİVERSİTESİ
FEN BİLİMLERİ ENSTİTÜSÜ

MEDİKAL UYGULAMALAR İÇİN MANYETİK PARÇACIK GÖRÜNTÜLEME (MPI) TARAYICI TASARIMI VE UYGULAMASI

MUHAMMAD İRFAN
DOKTORA TEZİ
ELEKTRONİK MÜHENDİSLİĞİ ANABİLİM DALI

DANIŞMANI
DOÇ. DR. FUAD ALİEW
II. DANIŞMANI
DOÇ. DR. AYHAN BİNGOLBALİ

GEBZE
2021

DOKTORA JÜRİ ONAY FORMU

GTÜ Fen Bilimleri Enstitüsü Yönetim Kurulu’nun 18/11/2021 tarih ve 2021/55 sayılı kararıyla oluşturulan jüri tarafından 24/11/2021 tarihinde tez savunma sınavı yapılan Muhammad İrfan’ın tez çalışması Elektronik Mühendisiği Anabilim Dalında DOKTORA tezi olarak kabul edilmiştir.

JÜRİ

ÜYE
(TEZ DANIŞMANI) : Doç. Dr. Fuad ALİEW

ÜYE : Doç. Dr. Emine Ülkü SARITAŞ ÇUKUR

ÜYE : Prof. Dr. Faik MİKAİLZADE

ÜYE : Dr. Öğr. Üyesi Köksal HOCAOĞLU

ÜYE : Dr. Öğr. Üyesi Bülent İRFANOĞLU

ONAY

Gebze Teknik Üniversitesi ………………. Enstitüsü Yönetim Kurulu’nun
……./……./...…. tarih ve …..…/…... sayılı kararı.

SUMMARY

Magnetic particle imaging (MPI) is a novel imaging technique presented in 2005 with great promise for various applications, such as vascular imaging, oncology imaging, lung imaging, neuro imaging, drug targeting, cell-based therapy, and thermal therapy. Real-time imaging of the MPI technique with a high spatio-temporal resolution of superparamagnetic iron oxide nanoparticles (SPIONs) opened a window to innovative biomedical applications. Under the scope of this thesis firstly, a magnetic particle relaxometer (MPR) was designed and implemented at 4.6 kHz and 9.9 kHz for the characterization of the magnetic nanoparticles (MNPs). In-house MPR was used to help the synthesis process of the novel tracer agents for MPI applications. Secondly, an MPI scanner was designed and implemented with a gradient field of 4.3 T/m for phantom imaging with a bore size of 28 mm. A solenoid drive and receive coils were constructed at 9.3 kHz with an excitation field of 15 mT (peak amplitude). The spatial resolution of 5.04 mm was achieved for Perimag tracer at 15 mT drive field at 9.3 kHz. The dependence of spatial resolution on instrumentation and tracer agents was thoroughly studied. Thirdly, a medium bore size MPI scanner was also developed with a 6.2 T/m gradient field using field-free point (FFP) spatial encoding. Solenoid drive and receive coils at 9.2 kHz along the bore axis (scanning axis) with an excitation field of 15 mT were used. Saddle drive and receive coils at 9 kHz perpendicular to the bore axis with an excitation field of 15 mT were utilized.

Key Words: Field Free Point (FFP), Magnetic Nanoparticles (MNPs), Magnetic Particle Imaging (MPI), Magnetic Particle Relaxometer (MPR), Superparamagnetic Iron Oxide Nanoparticles (SPIONs).

ÖZET

2005 yılında sunulan manyetik parçacık görüntüleme (MPG=MPI), vasküler damar görüntüleme, onkoloji görüntüleme, akciğer görüntüleme, beyin görüntüleme, ilaç hedefleme, hücre temelli terapi ve termal terapi gibi çeşitli uygulamalar için büyük umut vaat eden yeni bir görüntüleme tekniğidir. Süperparamanyetik demir oksit nanoparçacıklarının (SDON=SPION'lar) uzaysal-zamansal olarak yüksek çözünürlüğüyle birlikte, MPI tekniğinin gerçek zamanlı görüntülenmesi, yenilikçi biyomedikal uygulamalara yeni bir pencere açmıştır. Bu tez kapsamında ilk olarak, manyetik nanoparçacıkların (MNP'ler) karakterizasyonu için 4.6 kHz ve 9.9 kHz'de çalışan bir manyetik parçacık relaksometre (MPR) tasarlanmış ve uygulanmıştır. Özel tasarım MPR, MPI uygulamaları için yeni izleyici ajanların tasarlanma sürecine yardımcı olmak için kullanıldı. İkinci olarak, fantom görüntüleme için 28 mm oyuk büyüklüğüne sahip 4.3 T/m gradyan alanına sahip bir MPI tarayıcı tasarlanmış ve uygulanmıştır. 15 mT'lik bir eksitasyon alanıyla (tepe genliği) 9.3 kHz'de bir solenoid sürücü ve alıcı bobinler tasarlandı. Perimag referans izleyici için 9.3 kHz'de 15 mT sürücü alanında 5.04 mm'lik uzaysal çözünürlük elde edildi. Uzaysal çözünürlüğün donanımsal kısımlara ve izleyici ajanlara bağlılığı kapsamlı bir şekilde incelendi. Üçüncü olarak, uzaysal kodlama için manyetik alansız nokta (MAN=FFP) kullanılarak 6.2 T/m gradyan alanıyla orta çapta oyuk büyüklüğüne sahip bir MPI tarayıcısı da geliştirildi. 15 mT eksitasyon alanı ile oyuk ekseni (tarama ekseni) boyunca 9.2 kHz için solenoid sürücü ve alıcı bobinler kullanıldı. 15 mT'lik bir eksitasyon alanı ile oyuk eksenine dik 9 kHz'de eyer tipi (saddle) sürücü ve alıcı bobinler kullanıldı.

Anahtar Kelimeler: Manyetik Alansız Nokta (MAN=FFP), Manyetik Nanoparçacıklar (MNP), Manyetik Parçacık Görüntüleme (MPG=MPI), Manyetik Parçacık Relaksometre (MPR), Süperparamanyetik Demir Oksit Nanoparçacıklar (SDON=SPION).

ACKNOWLEDGEMENTS

First and foremost, I would like to express my deepest appreciation to Assoc. Prof. Dr. Nurcan Dogan for giving me the opportunity to be part of her research group. I am thankful to Assoc. Prof. Dr. Nurcan Dogan to share her valuable knowledge and experience with me throughout my thesis research at the applied medical imaging lab (AMIL) at the physics department. She always supported and encouraged me to overcome challenges during my Ph.D. research.

I am thankful to my supervisor, Assoc. Prof. Dr. Fuad Aliew for unconditional support throughout my doctoral studies. He always stayed behind me and provide all kinds of assistance. I am also thankful to my co-supervisor, Assoc. Prof. Dr. Ayhan Bingolbali to provide me partial financial support from the Tubitak project. I am grateful to the Scientific and Technological Research Council of Turkey through TUBITAK Grant No: 115E776 & 115E777 for my thesis work. I would like to thank TURKEY SCHOLARSHIPS for granting me a P.h.D scholarship between 2017-2021.

I am extremely thankful to my thesis monitoring committee and thesis jury member, Assoc. Prof. Dr. Emine Ülkü Sarıtaş for her guidance and support throughout my thesis period. Her feedbacks and comments on my thesis work were very valuable and helpful. I would like to thank other thesis monitoring committee members and jury members, Assist. Prof. Köksal Hocaoğlu, Prof. Dr. Faik Mikailzade and Assist. Prof. Bulent Irfanoglu for valuable remarks.

I would like to thank my past colleagues at Applied Medical Imaging Lab (AMIL), Tarık Sapmaz, and Özge Mercan Doğan for their support. I am also grateful to Dr. Erdem Demirci, Dr. Yavuz Ozturk, and Fahreddin Fatih Ongul.

Finally, I am thankful to my family for their support and confidence in me. I want to express my greatest gratitude to my parents for their patience and for allowing me to pursue my post-graduate studies thousands of miles away from them. It was a dream of my mother to see me as a successful person on the academic ladder. I am thankful to her for always motivating me to achieve big goals throughout my life.

TABLE of CONTENTS

LIST of ABBREVIATIONS and ACRONYMS

Abbreviations and Acronyms		**Explanations**
AC	:	Alternating current
B	:	Magnetic field
BSF	:	Band stop filter
CA	:	Citric acid
CT	:	Computed tomography
DAQ	:	Data acquisition
DC	:	Direct current
EM	:	Electromagnets
ESR	:	Electron spin resonance
ESR	:	Equivalent series resistance
FFL	:	Field free line
FFP	:	Field free point
FFT	:	Fast fourier transform
FOV	:	Field of view
FWHM	:	Full width at half maximum
G	:	Gradient field
LNA	:	Low noise amplifier
LSI	:	Linear shift and invarient
MNPs	:	Magnetic nanoparticles
MPI	:	Magnetic particle imaging
MPR	:	Magnetic particle relaxometer
MPS	:	Magnetic particle spectrometer
MRI	:	Magnetic resonance imaging
PAA	:	Polyacrylic acid
PET	:	Positron emission tomography
PNS	:	Peripheral nerve stimulation
PM	:	Permanent magnet
PPMS	:	Physical properties measurement system
PSF	:	Point spread function

RMS : Root mean square

ROI : Region of interest

SAR : Specific absorption rate

SNR : Signal-to-noise ratio

SPECT : Single photon emission computed tomography

SPIONs : Superparamagnetic iron oxide nanoparticles

VSM : Vibrating sample magnetometry

LIST of FIGURES

LIST of TABLES

1. INTRODUCTION

Magnetic Particle Imaging (MPI) was invented in 2005 as a tomographic technique [1]. The development of medical imaging and diagnostic tools, and therapeutic treatments are interrelated. Magnetization of the positive contrast agent utilized in MPI outperforms the proton magnetization in Magnetic Resonance Imaging (MRI) which becomes the source of this invention [2].

1.1. Brief Literature Review of MPI

Biological tissues do not generate background signals for the MPI technique. Hence, MPI is a zero-depth attenuation technique. It is fundamentally distinct from other imaging tools such as MRI, Computed Tomography (CT), but resembles Positron Emission Tomography (PET) [3]. A comparison of some medical imaging modalities adapted from the reference [5-16] is presented in Table 1.1.

Table 1.1: Comparison among magnetic particle imaging (MPI) and other imaging techniques.

Modality	**Ultrasound**	**CT**	**MRI**	**SPECT**	**PET**	**MPI**
Spatial Resolution	1 mm	<1 mm	1 mm	3-10 mm	4 mm	< 1 mm
Acquisition time	< 1 s	1 s	10 s- 30 min	1 min	1 min	<0.1 s
Sensitivity	low	mM/10000	mM/10000	pM/10000	pM/10000	0.1µM/10-200
Quantifiability	No	Yes	No	Yes	Yes	Yes
Harmfulness	Heating and cavitation	Ionizing radiation	Heating and PNS	Ionizing radiation	Ionizing radiation	Heating and PNS
Contrast agents/tracers	Microbubbles (contrast agent)	Iodine (contrast agent)	Gadolinium, SPIO (contrast agent)	Radionuclide (radioactive tracer)	Radionuclide (radioactive tracer)	SPIO (Magnetic tracer)
Imaging method	Structural imaging	Structural imaging	Structural imaging	Tracer imaging	Tracer imaging	Tracer imaging

The high spatio-temporal resolution, nano molar sensitivity, super contrast agent capability of MPI makes it a potential candidate for the advancement of pre-clinical and clinical applications [4]. MPI has advanced at tremendous speed since its invention [16-18], with versatile biomedical applications such as stem cell labeling and tracking [19], vascular and perfusion imaging [14], lung imaging [20], and magnetic hyperthermia [21, 22].

A large fraction of the inspection object can be "switch off" with a static field to investigate a specific region by using the non-linear nature of the magnetic nanoparticles (MNPs) as tracer agents [2]. Field-free point (FFP) and field-free line (FFL) are prominent spatial encoding schemes that are static and spatially inhomogeneous. Both selection fields are implemented with NdFeB permanent magnets and/or electromagnets to achieve high gradient field strength (T/m). FFP is scanned through the target object using an alternating excitation field (i.e., drive field). Extreme limits of the FFP (as forward and backward motion) define a field of view (FOV). Forward and backward motions of the FFP over SPIONs inside the FOV induce a signal in a receive coil due to a change in magnetization of SPIONs. FOV has a direct relation with drive field strength (mT) and an inverse relation with gradient field strength. Specific absorption rate (SAR) and peripheral nerve stimulation (PNS) restrict the amplitude of the excitation field [23–25]. However, enlarge FOV for human size can be achieved with the integration of a focus field at low frequency [14, 26].

Image reconstruction time and image quality are trademarks of the post-processing techniques. A linear relationship between particle concentration and measured signal is the main assumption in all reconstruction techniques. Mainly two reconstruction approaches such as frequency domain-based system matrix, and time-domain based X-space are widely used for image reconstruction [27]. The system function can be measured from calibration-based, model-based, and hybrid approaches. The Time-domain X-space technique offers fast image reconstruction of the particle concentrations [28].

1.2. Motivation

In this thesis, the MPI technique was thoroughly studied to develop a new prototype medical imaging device. Mainly, it has three major parts such as synthesis of optimized MNPs as a tracer agent, hardware implementation for specific applications, and post-processing and reconstruction of the recorded data. Three MPI scanners of distinctive specifications were built in this thesis work.

Firstly, a magnetic particle relaxometer (MPR) was implemented commonly known as a zero-dimension (0D) MPI scanner for the characterization of potential tracer material for MPI applications. Point spread function (PSF), effective relaxation time, frequency signature, and relative signal of the magnetic nanoparticle samples were aimed to be studied at 4.6 kHz and 9.9 kHz, respectively.

Secondly, an MPI scanner with moderate gradient field strength and bore size was targeted for phantom imaging using commercial and locally synthesized MNPs. The spatial resolution of the MPI scanner was the key aspect to explore with high sensitivity.

Lastly, another MPI scanner with 2D FOV with a medium bore size suitable for small animals like rats and mice was also planned to construct. To improve temporal resolution drive and receive coils for two perpendicular axes were operated simultaneously. In addition to this, gradient field strength was targeted to increase the spatial resolution of the MPI scanner with 2D FOV. Lissajous scanning sequence ensures high temporal resolution as compared to cartesian scanning sequence.

1.3. Outline of the Thesis

In this thesis, three distinctive devices based on the physics of magnetic particle imaging (MPI) are implemented. MPI is a novel medical imaging tool that promises higher spatio-temporal resolution as compared to other imaging modalities briefly discussed in the first chapter. Novel magnetic nanoparticles have the potential to be used in the diagnosis and treatment of cancer detection and other human diseases as mentioned in the second chapter. MPR was implemented for the characterization of the MNPs, and it figures out optimized nanoparticles for MPI applications thoroughly discussed in the third chapter.

MPR does not differentiate signals from different parts of the region of interest (ROI). Therefore, spatial encoding was inevitable for more accurate diagnostics. The design and implementation of the spatial encoding scheme are thoroughly explained in the fourth chapter. NdFeB permanent magnets and/or electromagnets can be used for the realization of the selection field. An MPI scanner was designed and implemented for phantom imaging as discussed in the fifth chapter.

Image reconstruction techniques are elaborated in the sixth chapter. Mainly, system function and X-space techniques are dominant techniques so far in MPI. X-space reconstruction is applied for the post-processing of the MPI scanner data.

Finally, a large-bore size MPI scanner with 2D FOV was designed and developed for small animals and thoroughly discussed in the seventh chapter followed by the results and discussion section of the thesis.

2. MAGNETIC NANOPARTICLES FOR MPI

Magnetic nanoparticles have a long history in medical imaging. MNPs with different magnetic core and hydrodynamic coating are used for various medical applications. SPIONs have been used in MRI [29] as a negative contrast agent to suppress the background signal. However, MPI does not have a background signal. So, SPIONs also called tracer agents are used as signal sources [1] to carry out a scan of objects (phantoms, in-vitro, and in-vivo applications). SPIONs have been widely used in other biomedical applications such as hyperthermia therapy [30, 31], tissue repair [32, 33], drug delivery [34, 35], and stem cell tracking [36, 37]. Single domain nanoparticle with possible functionalities adapted from reference [38] is pictorially represented in Figure 2.1. The thickness of the coating layers ensures the minimum particle-to-particle interaction that prevents agglomeration phenomena.

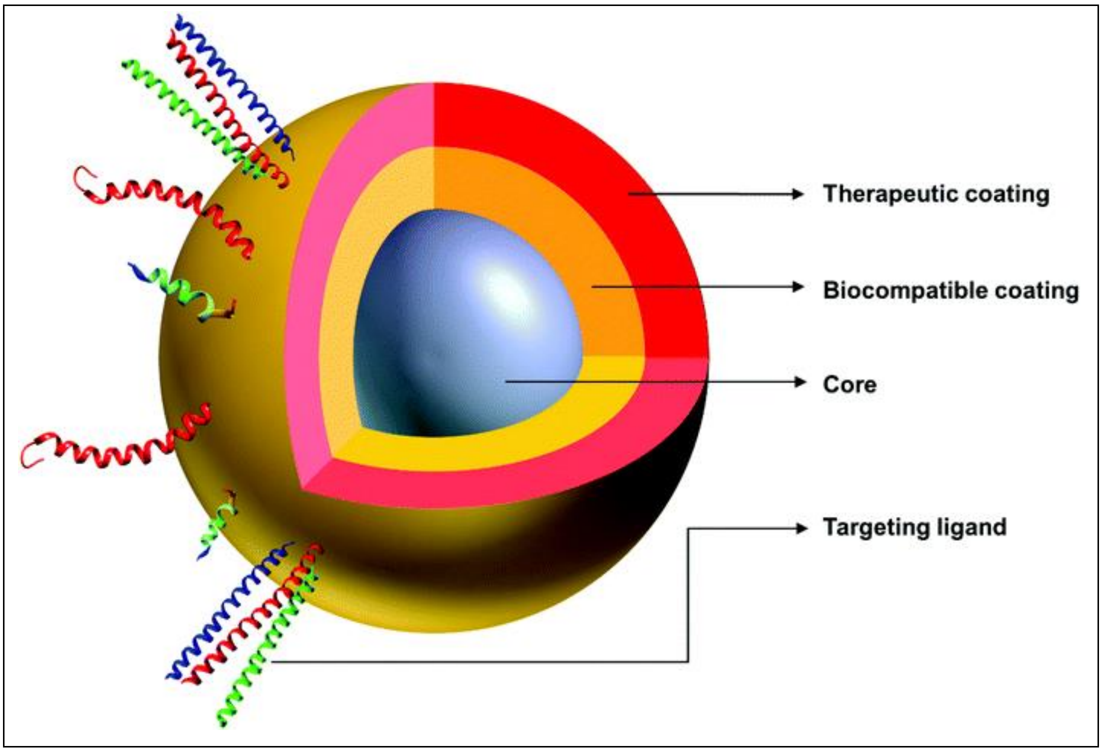

Figure 2.1: Magnetic core, coatings, and targeting ligand representations of SPIONs.

Ideally, SPIONs do not have any hysteresis that makes them perfect tracer material for imaging tasks. Remanence and coercivity do not exist in SPIONs and they are non-toxic as well [39]. MPI community uses versatile iron oxides among them well-known tracer agents adapted from [40-46] are presented in Table 2.1.

Table 2.1: Commonly used magnetic nanoparticles as tracer agents in MPI.

Iron Oxide/Developer	Core material	Core diameter	Coating material	Hydrodynamic diameter	Normalized to Resovist
Resovist/BayerPharma AG	Fe_2O_4, Fe_2O_3	5.5 nm (24nm, 30%)	Carboxydextran	62 nm	1
Vivotrax/magnetic Insight	Fe_2O_4, Fe_2O_3	4.2 nm	Carboxydextran	62 nm	1
UW/University of Washington	Fe_3O_4	17 nm	PMAO-PEG	86 nm	2x
Perimag/Micromod	Fe_2O_4	19 nm	Dextran	130 nm	2x
Nanomag/Micromod	Fe_2O_4	5-15 nm (19nm, 80%)	Dextran	100 nm	2x
FluidMAG-D/Chemicell GmbH	Fe_2O_3	n/a	Dextran	50 nm	n/s
MCP3/ Charité-Universitätsmedizin	Fe_2O_4, Fe_2O_3	31.72 nm	Carboxymethyl dextran	24.4-122.4 nm	5x

2.1. Magnetization Response

Superparamagnetic behavior is observed in Fe_3O_4 (magnetite) and γ-Fe_2O_4 (maghemite) that are fundamental SPIONs with magnetization similar to their bulk materials [47]. The magnetization and applied field of SPIONs have non-linear relations instead of linear relationships for paramagnetic materials. The magnetization behavior changes abruptly at low applied magnetic fields and stays at fixed magnetization levels at higher magnetic fields as shown in Figure 2.2. As the magnetic field increases magnetization becomes saturated after a certain point, so applying a higher magnetic field does not enhance particle magnetization. In MPI, non-linear response in the dynamic range is utilized.

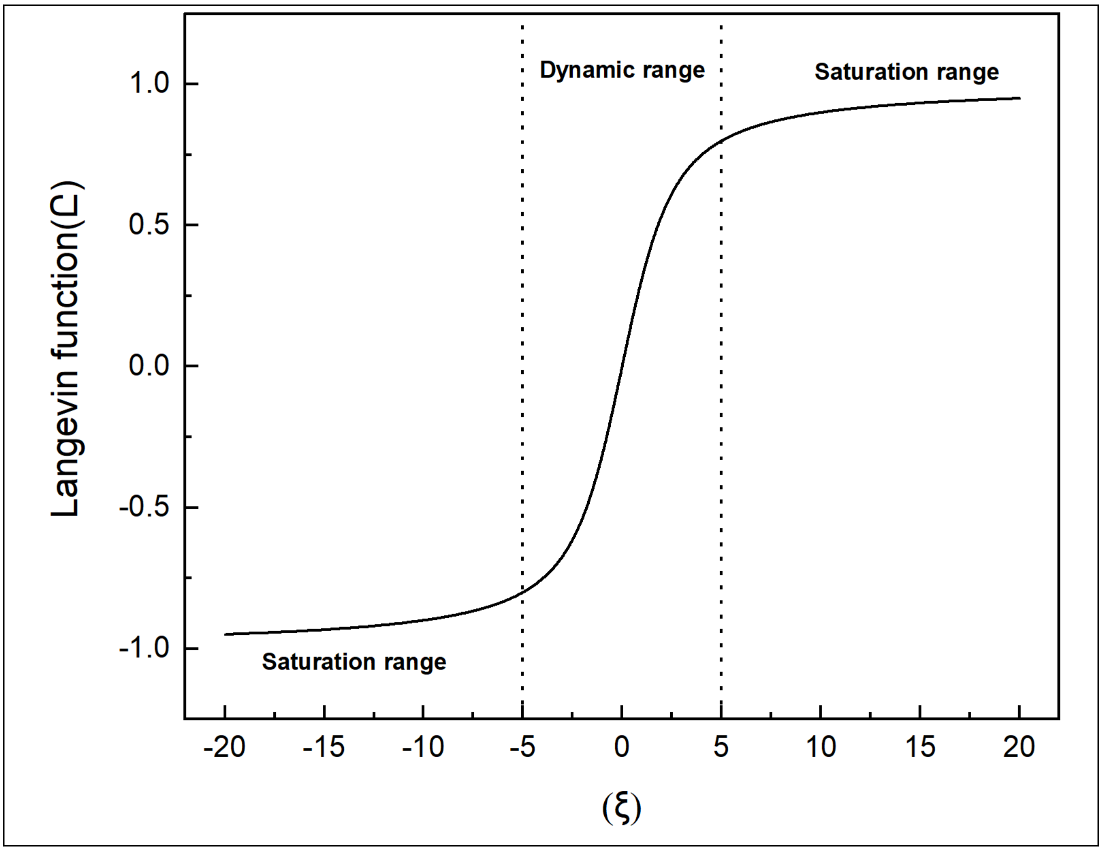

Figure 2.2: Langevin function for magnetization of the SPIONs. It is abruptly changing from -5 to 5 (dynamic range). As the applied magnetic field increases, the Langevin function becomes saturated after a certain point.

The relationship between the applied magnetic field and magnetization response of the SPIONs can be mathematically expressed using Langevin function [15];

$$\mathfrak{L}(\xi) := \begin{cases} \left(\coth(\xi) - \frac{1}{\xi}\right) & \xi \neq 0 \\ 0 & \xi = 0 \end{cases} \tag{2.1}$$

All the nanoparticles are assumed at thermal equilibrium.

SPIONs are composed of nanoscale magnetic nanoparticles. The magnetic moment of an individual particle is represented by m. Due to Brownian motion, the magnetic moments of the samples are randomly oriented. Hence, the net magnetic movement of the sample is zero. Overall, the magnetization (M) of the sample is expressed as [15];

$$M \coloneqq \frac{1}{\Delta V} \sum_{i=0}^{N^P-1} m_i \tag{2.2}$$

MNPs follow the direction of the applied magnetic field. In the saturation range, nanoparticles are fully aligned to the applied field direction. If the relaxation time phenomenon is ignored, then magnetization at the applied magnetic field is easily expressed as [15];

$$\boldsymbol{M}(\boldsymbol{H}) = M(H)e_H \tag{2.3}$$

The magnetization response of the MNPs based on Langevin function can be calculated as [15];

$$M(H) = cm\mathfrak{L}(\alpha H) \tag{2.4}$$

$$\alpha \coloneqq \frac{\mu_0 m}{k_B T} \tag{2.5}$$

Here, T represents the temperature of the nanoparticles, while k_B is the Boltzmann constant. In the meantime, c in equation (2.4) represents the particle concentration. Similarly, m in equation (2.4) denotes the magnetic moment which can be calculated as [15];

$$m = V_c M_s \tag{2.6}$$

Here, V_c is the volume of the particle core, while M_s is the saturation level of the magnetization. If the particles have diameter D_c then the volume of the spherical particle can be calculated as [15];

$$V_c = \frac{1}{6}\pi D_c^3 \tag{2.7}$$

Practically, the iron concentration of the sample is more important as compared to particle concentration. If the iron concentration is kept constant, then particle concentration has an inverse relation with its particle volume. Saturation magnetization can be expressed as [15];

$$M_s = cm \tag{2.8}$$

Magnetization is independent of particle size as presented in Figure 2.3. Magnetization response of SPIONs with core diameter from 5 nm to 45 nm have the same saturation level.

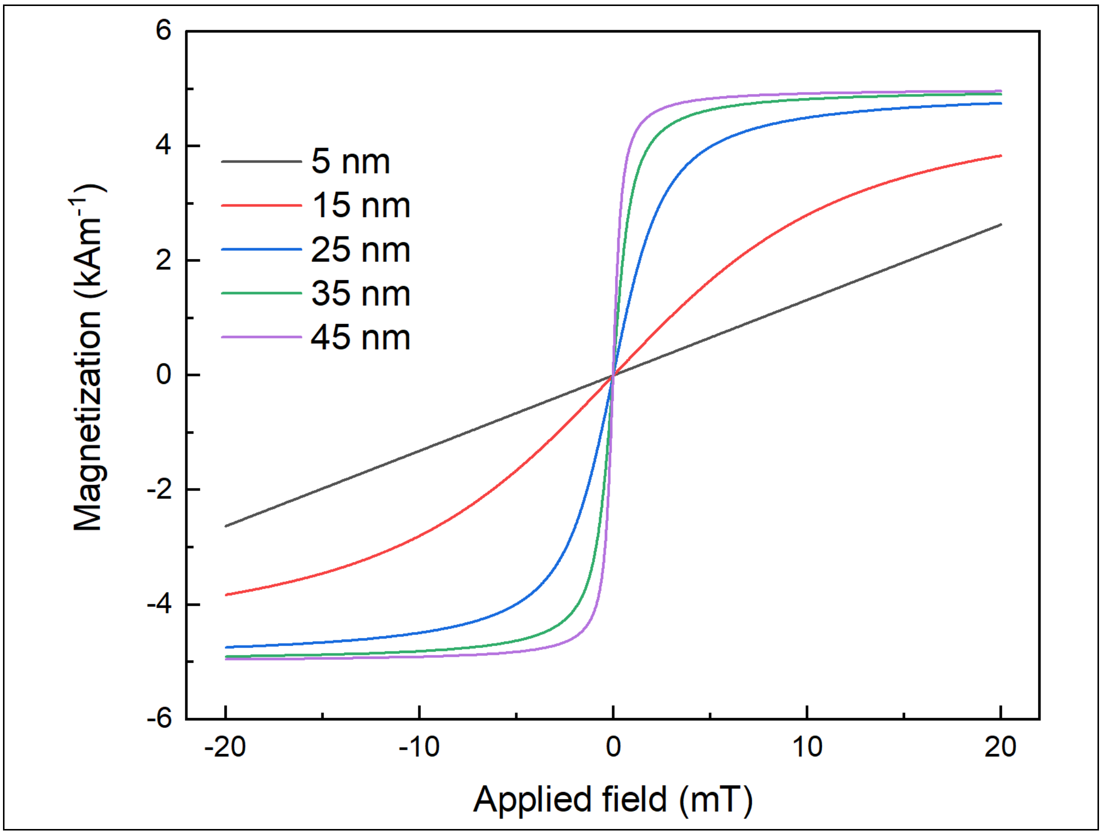

Figure 2.3: SPIONs magnetization for a core diameter of 5 nm to 45 nm. In the meantime, iron concentration was kept constant.

2.2. Width of Dynamic Range

The dynamic range of the magnetization response has a crucial role in the physics of MPI. It is different for different particle sizes. The width of the dynamic range can easily obtain from the derivative of the magnetization curves. The full width at half maximum (FWHM) is a more classic approach to measure the width of the dynamic range.

$$M'(H) = cm\mathfrak{L}'(\beta H) \tag{2.9}$$

Similar to the magnetization response, the derivative of the magnetization response depends upon the derivative of the Langevin function [15];

$$\mathfrak{L}'(\xi) := \begin{cases} \left(\frac{1}{\xi^2} - \frac{1}{sinh^2(\xi)}\right) & \xi \neq 0 \\ \frac{1}{3} & \xi = 0 \end{cases} \tag{2.10}$$

FWHM of the Langevin function derivative is 4.16 (fixed) as shown in Figure 2.4.

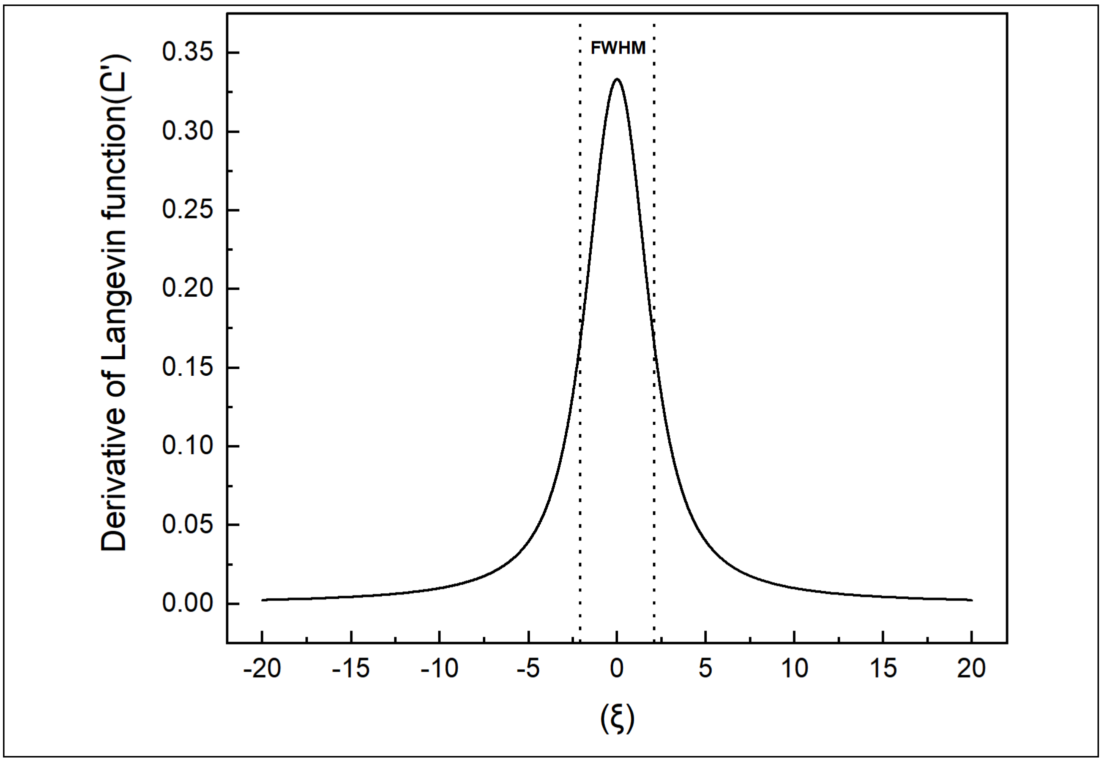

Figure 2.4: The width of the Langevin function is obtained from its derivative function.

The width of the particle magnetization with core diameter from 15 nm to 45 nm is drawn from their derivative respectively. As the particle size increases, FWHM of the MNPs is decreases as shown in Figure 2.5. It is obvious that FWHM of the MNP sample directly affects the spatial resolution. Similarly, signal-to-noise ratio (SNR) of the received signal directly increases with the steepness of the derivative curves. The width of the dynamic range can be calculated with the help of Langevin derivative width as expressed as [15];

$$\Delta H_{FWHM} = 4.16\frac{k_B T}{\mu_0 m} \tag{2.11}$$

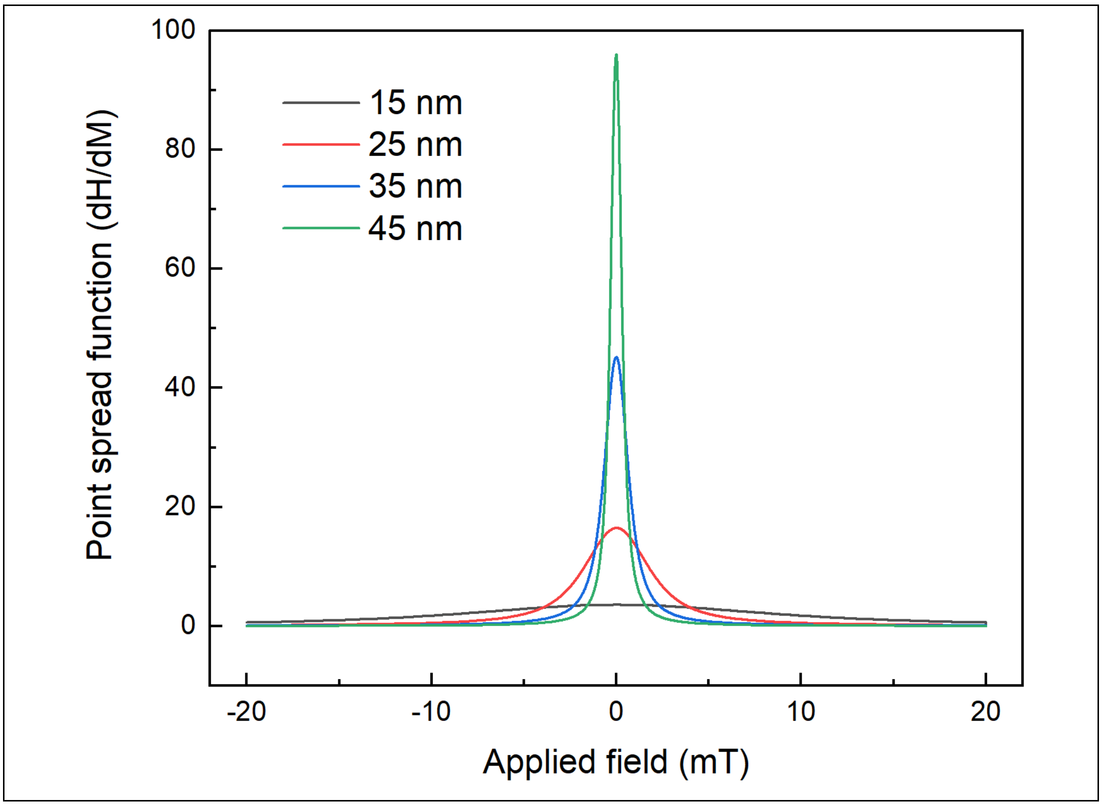

Figure 2.5: Point spread functions of the SPIONs at different core diameters. The width of the curves is elaborated from FWHM.

2.3. Relaxation Concept of Magnetic Nanoparticles

The instantaneous response of the magnetic nanoparticles is strictly valid at the static field. However, magnetization response to the oscillating magnetic fields brings a certain delay. The behavior of magnetic nanoparticles to the oscillating magnetic field is modeled by the Langevin function [48].

$$M_{ideal}\big(H(t)\big) = mc\left(\coth\big(\alpha H(t)\big) - \frac{1}{\alpha H(t)}\right) \tag{2.12}$$

Here, all nanoparticles are assumed of similar size (monodisperse) which is not quite easy to achieve. Practically, MNPs of different diameters (polydisperse) are synthesized comfortably, such as Vivotrax (Magnetic Insights, USA) tracer has 4.2 nm diameter (70%) and nanoparticles of 19 nm diameter (30%) play a crucial role in MPI [42]. To achieve overall magnetization, polydisperse nanoparticles' magnetization should be averaged [29].

$$\widetilde{M}(H(t)) = \int_{D_{min}}^{D_{max}} \rho(D) M_{ideal}\big(H(t)\big) dD \tag{2.13}$$

where $\rho(D)$ is the probability of the polydisperse MNPs.

The magnetization response of the small-diameter (D_c < 30 nm) nanoparticles can track the applied field without any significant delay. However, large-diameter nanoparticles (30 nm ≤ D_c ≤ 100 nm) respond after a certain time delay to the applied magnetic field. Debye model [49] considers the relaxation effect in addition to the Langevin function for accurate modeling.

$$\frac{dM_{real}(H(t))}{dH(t)} = -\frac{M_{real}\big(H(t)\big) - M_{ideal}(H(t))}{\tau_{eff}} \tag{2.14}$$

where $M_{ideal}(H(t))$ is the ideal magnetization calculated with the Langevin model, $M_{real}(H(t))$ is the real magnetization that covers the relaxation effect. τ_{eff} is an effective relaxation time constant results of Neel and Brownian relaxation effects.

The relation between ideal and real magnetizations can be deducted by solving Debye differential equation (2.14);

$$M_{real}\big(H(t)\big) = M_{ideal}(H(t)) * \frac{1}{\tau_{eff}} \exp\left(-\frac{t}{\tau_{eff}}\right) u(t) \tag{2.15}$$

where the symbol, $*$, is the temporal convolution, and $u(t)$ is the Heaviside step (unit step) function.

The rotation of the magnetic moment concerning a crystalline lattice in a fixed particle happens when thermal energy becomes higher than the anisotropy energy barrier. This is known as Neel relaxation and zero-field relaxation time is expressed as;

$$\tau_{N0} = \tau_0 \exp\left(\frac{KV_c}{k_B T}\right) \tag{2.16}$$

where V_c is the volume of the magnetic core, K is the crystalline anisotropy constant, τ_0 is the time constant (10^{-10}s).

Thermal and viscous drag forces of the magnetic nanoparticles oppose the magnetic torque (because of the applied field) which pushes the net magnetic moment to align with an applied field direction. SPIONs' crystal shape (e.g., spherical, cubical), environmental properties, and measurement parameters define the thermal and viscous forces. The physical rotation of SPIONs is known as Brownian relaxation [55] as shown in Figure 2.6 and zero-field Brownian relaxation time [50] can be described as;

$$\tau_{B0} = \frac{3\eta V_h}{k_B T} \tag{2.17}$$

where V_h is the hydrodynamic volume of the iron nanoparticle, and η is the dynamic viscosity of the environment.

The zero-field Brownian and Neel relaxation time constants in equations (2.16) and (2.17) are oversimplified. Neel and Brownian relaxation times vary as a function of the applied excitation field. Neel relaxation time decreases at a faster rate instead of Brownian relaxation time. Higher magnetic field effects on Neel and Brownian relaxation times were discussed in detail by the references [51, 52]. A numerical approach was followed to investigate Neel and Brownian relaxation times dependence with applied magnetic field strength [52] while in another research work analytical approach was utilized [51]. Brown modeled Neel relaxation [55] time as shown in Figure 2.6 using high-barrier approximation as given by [53];

$$\tau_{N,H} = \frac{\sqrt{\pi}\left({}^{\alpha_K}\!/_2\right)^{-3/2}}{(1-h^2)} \tau_{NH0}\left[(1+h)e^{\left({}^{\alpha_K}\!/_2\right)(1+h)^2} + (1-h)e^{\left({}^{\alpha_K}\!/_2\right)(1-h)^2}\right]^{-1} \tag{2.18}$$

where $h \equiv {}^{M_s B}\!/_{(2K)} = {}^{\alpha}\!/_{\alpha_K}$, $\tau_{NH0} \equiv \frac{\beta(1+\alpha'^2)M_s}{2\gamma\alpha'}$, $\alpha_K \equiv 2K\beta = \frac{2KV_c}{kT}$, and γ is the electron gyromagnetic ratio.

Similarly, Yoshida and Enpuku presented an empirical model by using the Fokker-Planck equation for magnetic nanoparticles with thermally blocked assumption presented by the reference [54]. Brownian relaxation time at a higher alternating magnetic field is described as;

$$\tau_{B,H} = \frac{\tau_{B0}}{\sqrt{1 + 0.126\xi^{1.72}}} \tag{2.19}$$

Where $\xi = {}^{mB}/_{k_B T}$, τ_{B0} is the zero-field Brownian relaxation time previously mentioned in equation (2.17).

Brownian and Neel relaxation times at higher excitation fields are evaluated individually so far. The combined effect of both relaxation times is very challenging to model. However, a simplified form of both relaxation times is widely used by MPI community.

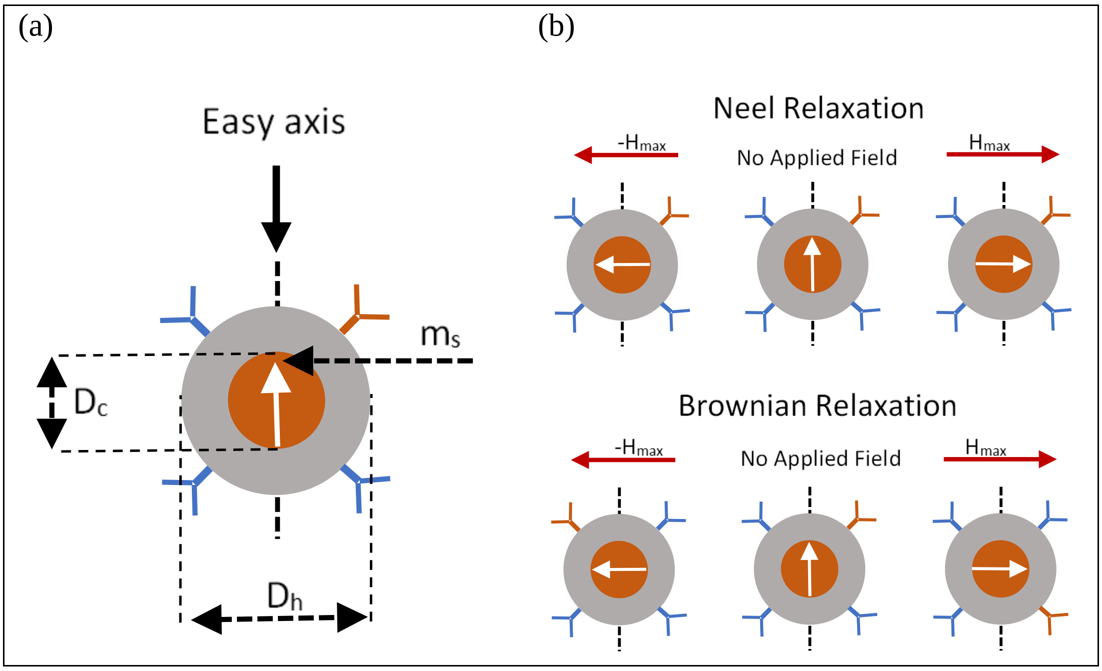

Figure 2.6: (a) Single domain superparamagnetic iron oxide particle structure (D_c: Diameter of the iron core, D_h: Diameter of hydrodynamic coating, and m_s: magnetic moment). (b) Neel and Brownian relaxation of the magnetic nanoparticles at different directions (right direction for positive and left direction for negative magnetic applied fields) of an applied field.

The effective relaxation time constant (τ_{eff}) is a combined effect of Brownian relaxation constant (τ_{B0}) and Neel relaxation constant (τ_{N0}), and can be expressed as [15];

$$\tau_{eff} = \frac{\tau_{B0}\tau_{N0}}{\tau_{B0} + \tau_{N0}} \tag{2.20}$$

Brownian and Neel relaxation time constants vary as a function of applied magnetic field and frequency. Relaxation kernel [56] can be defined as;

$$r(t) = \frac{1}{\tau_{eff}} \exp\left(-\frac{t}{\tau_{eff}}\right) u(t) \tag{2.21}$$

Hence, the real magnetization behavior of SPIONs can be easily modeled as;

$$M_{real}\big(H(t)\big) = M_{ideal}(H(t)) * r(t) \tag{2.22}$$

where $*$ is the temporal convolution parameter.

2.4. Magnetic Properties of SPIONs

SPIONs as a tracer agent plays an important role in the performance of MPI. Electron spin resonance (ESR), physical properties measurement system (PPMS), and magnetic particle spectrometer (MPS) are used as evaluation tools for the magnetic properties. Nickel ferrites ($NiFe_2O_4$) uncoated and coated with citric acid (CA) and polyacrylic acid (PAA) were synthesized as potential tracer agents for MPI applications by hydrothermal process under the scope of this thesis.

2.4.1. Physical Properties Measurement System (PPMS)

$NiFe_2O_4$ samples' magnetization response to the static magnetic field was analyzed by using physical properties measurement system (PPMS). Similar to the Langevin function, the PPMS tool applies a static magnetic field to measure saturation magnetization (M_s), remanent magnetization (M_r), and coercivity (H_c) of the samples. Relation between M and H has been investigated at 300 K and 400 K temperatures for all MNPs, and the results [57] are shown in Figure 2.7.

The fitting of experimental M(H) curves as shown in Figure 2.7 with equations (2.4) and (2.12) estimates the magnetic core diameters of the nanoparticles (D_c). The extracted values of D_c are given in Table 2.2 along with Ms, M_r, and H_c properties [57] of the samples.

Table 2.2: The magnetic properties were deduced from M-H data at 300 K and 400 K temperatures for nickel ferrite-based MNPs.

Tem. (K)	**Sample**	**M_s (emu/g)**	**M_r (emu/g)**	**H_c (Oe)**	**SQR (M_r/M_s)**	**K (J/m^3)**	**μ_B**	**D_c (nm)**
300	$NiFe_2O_4$	46	0.74	9.3	0.0161	668.5	1.947	14.760
	$NiFe_2O_4$@PAA	24	0.23	12	0.0096	450.0	1.016	20.151
	$NiFe_2O_4$@CA	5.9	0.12	20	0.0203	184.4	0.249	37.593
400	$NiFe_2O_4$	43	0.25	13	0.0058	873.4	1.820	17.027
	$NiFe_2O_4$@PAA	22	0.67	12	0.0305	412.5	0.931	21.995
	$NiFe_2O_4$@CA	4.61	0.04	18	0.0087	129.7	0.195	44.047

The coating materials significantly affect the magnetic properties of $NiFe_2O_4$ spinel ferrites. Stoner–Wohlfarth (S–W) approach was used [58, 59] to measure M_s values which are in the 5.9 - 46 emu/g range, M_r and H_c values are in the range 0.12 - 0.74 emu/g, and 9.3 - 20 Oe, respectively at room temperature of 300 K. All M-H curves of the nickel ferrite samples have *S*-like (shape of M-H curve) superparamagnetic behavior.

Magnetic properties observed with PPMS slightly change with the operating temperature. The fluctuations are minimum at low temperature (300 K), however, these fluctuations increased at 400 K. The minimum values of M_s and M_r are observed for coated samples as compared to uncoated samples. The coercivity of the MNPs depends on various parameters such as the magneto-crystallite anisotropy, morphology, shape and grains size, size distributions, collinear spins in the core [60].

Anisotropy constant (K) value provides the difference in magnetization between easy and hard directions. K can be expressed using Brown's equation;

$$K = \mu_o M_s . H_C/2 \tag{2.23}$$

where μ_o is Bohr magneton at zero applied magnetic field.

The calculated value of the anisotropy constant (K) at 300 K and 400 K temperatures is presented in Table 2.2. The coating materials might cause strains in the MNPs, therefore, a change in μ_B may have occurred. μ_B is also directly proportional to M_s, and molecular weight (M_w). The relation between μ_B and M_s is given by [61]:

$$\mu_B = \frac{M_W \times M_s}{5585} \tag{2.24}$$

Bohr magneton (μ_B) provides the cation distribution of the nickel ferrites. The net magnetic moment per unit cell for Ni is $2\mu_B$. A maximum value of 1.947 for the uncoated $NiFe_2O_4$ is achieved at 300 K. However, μ_B is mainly decreasing with coating as the M_s values of the coated (PAA, CA) samples are drastically decreased. This change in μ_B is associated with incomplete cation distribution of nickel ferrites.

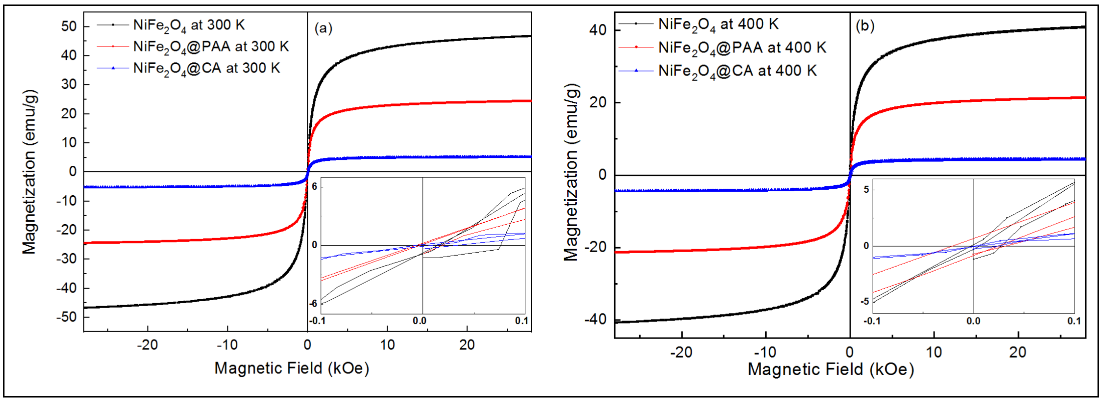

Figure 2.7: M-H curves of the nickel-based MPNs; (a) at 300 K, inset curves show magnified response at low fields (b) at 400 K, inset curves show magnified response at low fields.

Theoretically, SPIONs directly follow applied external field (DC) without any delay as they do not have remanent magnetization and low coercivity magnetic fields. Nickel ferrites prepared in this research have minimum M_r and H_c as presented in Table 2.2. PA and CA coated samples at 300 K show no hysteresis loop at low excitation fields which enable them to be potential tracer agents for MPI applications.

2.4.2. Magnetic Particle Relaxometer (MPR)

The magnetization response of the nickel ferrites (uncoated, PAA, and CA coated) at sinusoidal excitation fields up to 15 mT (peak amplitude) at 9.9 kHz was recorded with an in-house magnetic particle relaxometer (MPR). The slow decay of the odd harmonics of the coated sample is visible in Figure 2.8(a). The minimum FWHM of the NiFe2O4@PAA sample as shown in Figure 2.8(b) ensures high spatial resolution for MPI applications [57]. The results show that these nanoparticles might be potential tracer agents for MPI in the future.

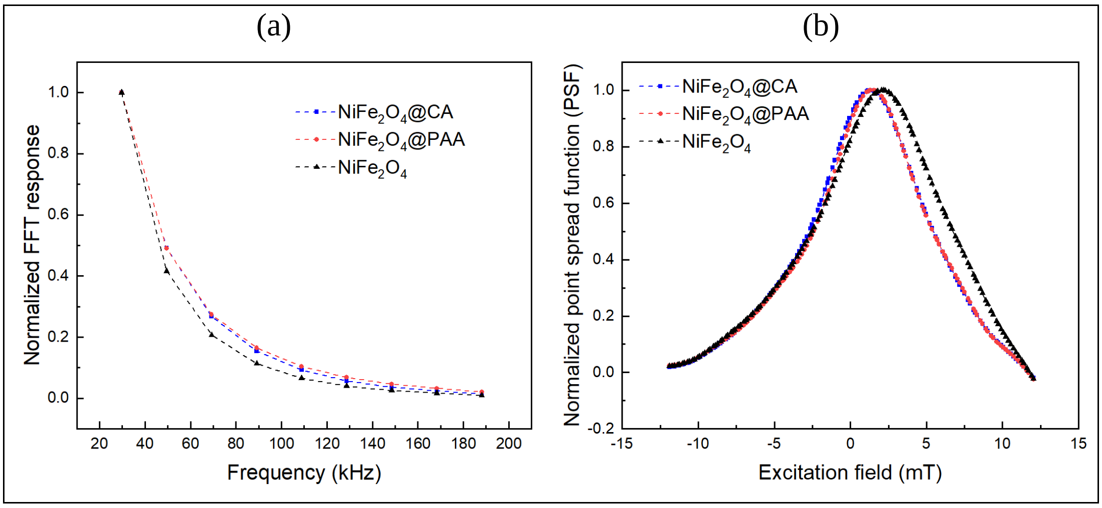

Figure 2.8: MPR characteristics of nickel-ferrites nanoparticles at 9.9 kHz with 15 mT (peak amplitude) excitation field; (a) Odd harmonics frequency spectrum of the nickel samples, (b) Resolution (FWHM, mT) of the nickel-based nanoparticles.

MPR is an especial tool to investigate key parameters for MPI applications. It is also known as a 0D MPI scanner. It works on alternating magnetic fields at approximately MPI scanner frequencies instead of the direct magnetic field in PPMS. MPR is designed and implemented for the characterization of magnetic nanoparticles. MPR is utilized to determine frequency spectrum, point spread function (PSF), relaxation time, relative signal, and magnetization curves at alternating magnetic fields under the scope of this thesis. A thorough discussion will be carried out on MPR in the next chapter.

3. MAGNETIC PARTICLE RELAXOMETER (MPR)

Magnetization response of the SPIONs at constant magnetic fields are measured with various devices such as AC magnetometry for low applied magnetic fields [62,63]. Saturation magnetization, coercitivity, and remanent magnetic fields are investigated with Vibrating Sample Magnetometry (VSM). Unfortunately, this device cannot characterize MNPs at alternating magnetic fields at specific frequencies for MPI. Since the invention of MPI in 2005, versatile tracer characterization tools such as MPS and/or Magnetic Particle Relaxometer (MPR) have been designed and implemented [41, 64-66]. Moreover, MPS (based on frequency domain) and MPR (based on time-domain) methods use the same hardware but different post-processing data analysis techniques.

MPR and MPS are commonly known as zero-dimensional MPI special tools. These tools are utilized to figure out potential tracer agents for MPI applications. Effective relaxation time and magnetic core diameter of the MNPs were evaluated with an MPI relaxometer [66]. In another study, sensitive characterization of the MNPs was performed with an eddy current shielded relaxometer [41]. In the meantime, tabletop nature (compact) empowered them to easily integrate with synthesis tools.

An in-house MPR tool was designed and implemented under the scope of this thesis. It is used for the identification of induced odd harmonics up to 20th harmonics, relaxation time (τ_{eff}), FWHM of PSFs as resolution, and relative signal strength of the MNPs. Vivotrax (Magnetic Insight, USA), Perimag (micromod, Germany), and Synomag (micromod, Germany) commercially available SPIONs were evaluated in this thesis.

3.1. MPR Hardware Setup

Sinusoidal excitation field at a specific frequency is applied to MNPs in MPR. The magnetization response of the MNPs is recorded for the post-processing. A cylindrical drive coil was used to generate a homogenous excitation field (drive field). A cylindrical receive coil (i.e., pick-up coil) was an ideal solution to record MNPs' response to the excitation field. Receive coil was placed symmetrically inside the drive coil. The sample was placed at the middle of the setup as shown in Figure 3.1. The measurement system was enclosed cylindrically with a copper shield of 10 mm (thickness) to reduce the environmental effects on the measurements. Relaxation of the tracer agents is the major cause of image blurring which reduces spatial resolution. Blurring can be minimized with a proper investigation of relaxation time and performing deconvolution in the post-processing of signals. MPR hardware setup adapted from [55] is shown in Figure 3.1.

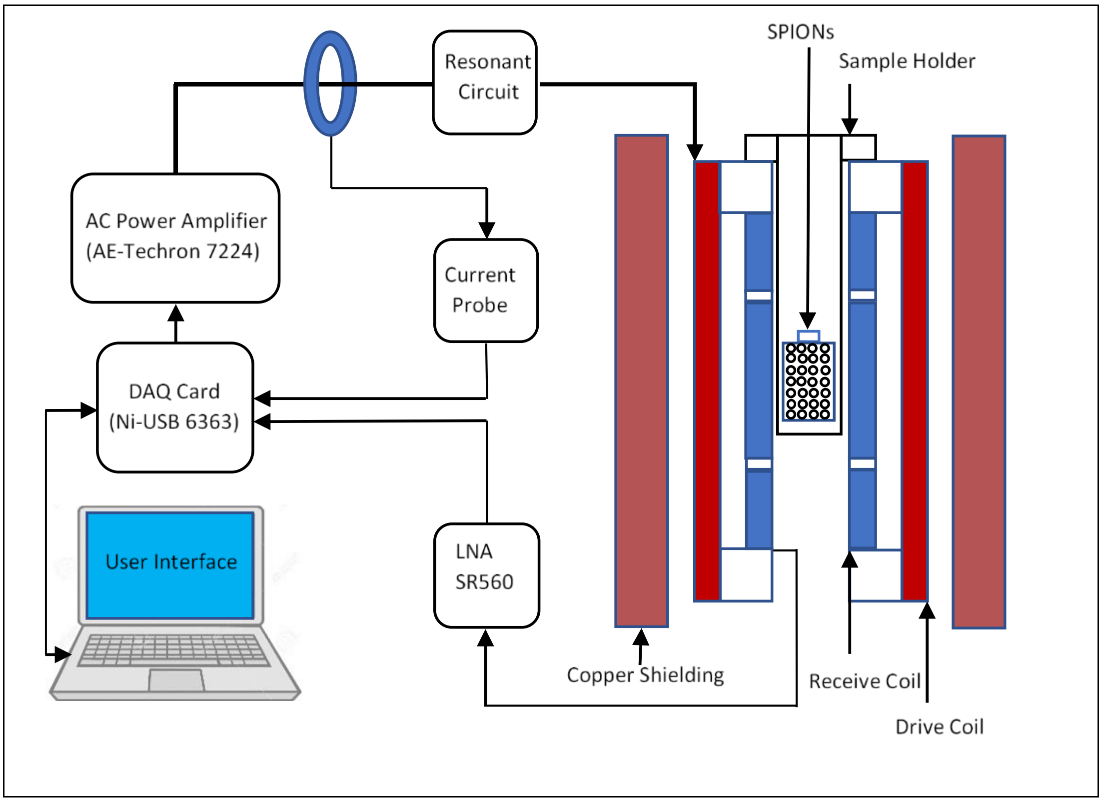

Figure 3.1: Hardware setup of the Magnetic Particle Relaxometer. The excitation field at a specific frequency is generated with a data acquisition (DAQ) card using a MATLAB environment. A power amplifier (AE-Techron 7224) is used to amplify the source signal to a higher power level to achieve desired excitation field. A resonant filter (impedance matching) is employed in the drive chain to achieve low power consumption. A current probe is utilized to measure the magnitude and phase of the applied alternating current. MNPs at the middle of the setup induce voltage signal on the receive coil that is filtered with a low noise amplifier (LNA 560) and then recorded with the same DAQ device for post-processing.

The drive and receive coils were wound with litz wire to mitigate the skin effects at high frequencies (4.6 kHz and 9.9 kHz). Both coils are inductively coupled so the fundamental component of the excitation frequency also induces on the receive coil without the presence of the SPIONs, known as the direct feedthrough effect. Geometric-based cancelation techniques are quite easy to implement, however, it is very challenging to remove the direct feedthrough completely. Three interconnected sections receive coil was built to minimize the feedthrough effect [55] as shown in Figure 3.2. Outer sections have half the number of turns with opposite winding directions.

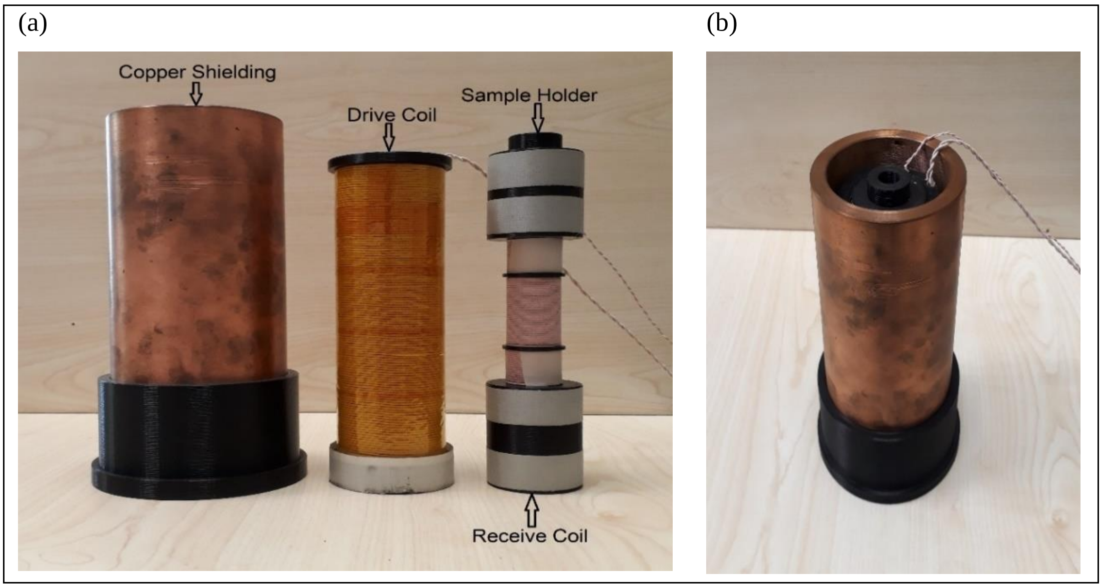

Figure 3.2: (a) Relaxometer components (shielding, drive and receive coil), (b) Single unit device.

The number of layers, physical dimensions (length and diameter), and electrical parameters (resistance and inductance) [55] are given in Table 3.1.

Table 3.1: Key parameters of the Magnetic Particle Relaxometer.

	Drive Coil	Receive Coil
Number of layers	2	5
Number of Turns	244	25:50:25
Length (mm)	165	80
Internal diameter (mm)	50	20
Resistance (Ω)	2.15	2.7
Inductance (μH)	411.15	855.7

3.2. Drive and Receive Coil Sensitivity

Drive coil was developed to generate an excitation field of 20 mT (peak amplitude). Litz wire was preferred instead of single-core wire to mitigate skin effects at higher frequencies of 4.6 kHz and 9.9 kHz. The appropriate diameter of the wire was chosen based on the maximum current capability. Receive coil was also built with the litz wire. Both coils were modeled and simulated in COMSOL® Multiphysics (COMSOL AB, Stockholm, Sweden).

Low electrical resistance and inductance are significant parameters in the design of a drive coil. The efficiency of the drive and receive coils can be investigated by applying 1A direct current (DC). The relation between magnetic flux density (mT) and applied current is known as sensitivity (i.e., transfer function). The drive coil has 1.75 mT/A sensitivity with 95.5% homogeneity in an 80 mm around the midpoint. The receive coil has 95% homogeneity in 12 mm range around the midpoint as shown in Figure 3.3. Magnetic flux density was measured with an axial probe (Lakeshore 475 DSP Gaussmeter). Numerical results obtained from COMSOL and experimental data are in good agreement [55] as shown in Figure 3.3. Magnetic field homogeneity of the drive coil helps receive coil design. Similarly, homogeneity of the receive coil reduces the fluctuation in the receive coil data.

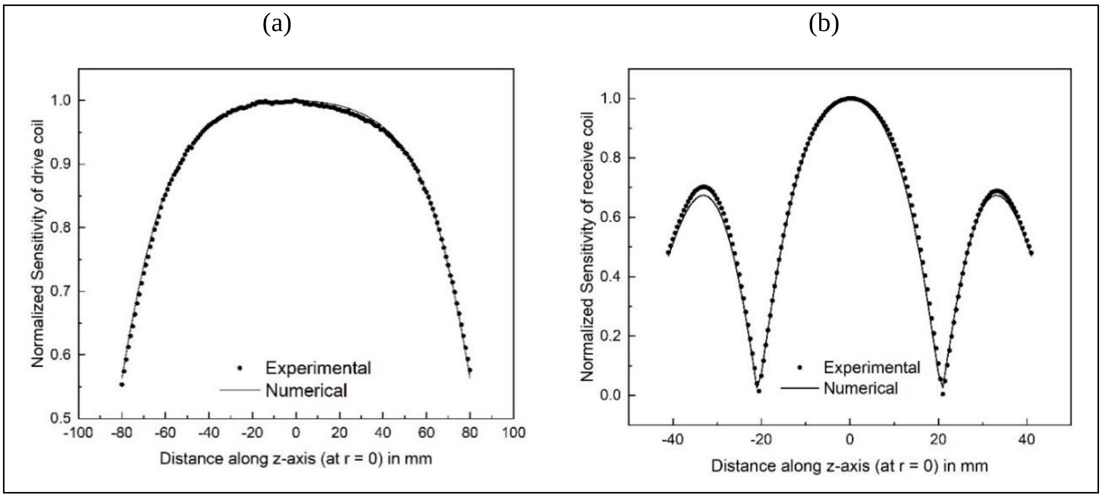

Figure 3.3: Normalized transfer functions of the drive and receive coils. (a) Drive coil sensitivity at 1A DC (b) Receive coil sensitivity at 1A DC.

A copper shielding of 10 mm thickness, a diameter of 70 mm, and a length of 200 mm was used to reject the environmental electromagnetic interferences. The copper shielding close to the drive coil increases the magnetic field homogeneity as it flattens the magnetic field lines. However, it reduces the sensitivity of the drive coil which demands more power to achieve the required excitation field. An Optimum air gap between drive coil and copper shielding was achieved with iterative numerical simulations with COMSOL® Multiphysics.

3.3. Data Acquisition and Effective Relaxation Time

Resonant impedance matched filters were integrated into the drive chain at 4.6 kHz and 9.9 kHz frequencies. Higher voltage rating capacitors (Cornell Dubilier) with high current capabilities were preferred. A data acquisition card (DAQ) (National Instruments, NI USB-6363, Austin, TX) was used for signal generation and data recording at 4.6 kHz, and 9.9 kHz frequencies, respectively. The receive coil voltage was passed through a low-noise amplifier (LNA) with a 100 Hz-300 kHz bandpass filter. All of these processes were controlled with a custom design MPR interface using MATLAB (Mathworks, Natick, MA). MPR data were recorded for 100 cycles with a repetition of 30 in a single run. A background signal was obtained before each experiment. At the post-processing stage, the background signal was subtracted from the MNPs' average data.

The excitation field generated by the drive coil is in phase with the current passing through the drive signal chain. Phases of the drive coil voltage, current and magnetic field at the excitation frequency are shown in Figure 3.4(a). The voltage across the drive coil was measured with LNA to keep a similar signal chain. The phase relation between the magnetization signal of the MNPs and the excitation field [55] is shown in Figure 3.4(b).

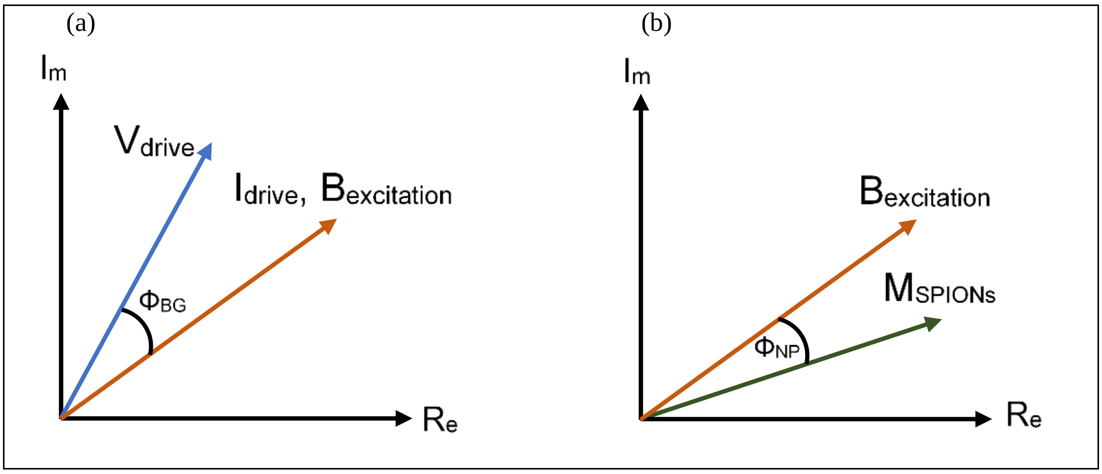

Figure 3.4: Phasor representation of current, excitation field, and the voltage across the drive coil (a) without sample, (b) with a sample at midpoint.

The system phase consists of transmit phase and delay of the drive chain, effective relaxation time (τ) can be evaluated with the phase sweep algorithm. The phase at which maximum values of the positive and negative PSF become symmetric at 0 mT of the applied field was searched with the algorithm.

$$System_{phase} = transmit_{phase} + transmit_{delay} \tag{3.1}$$

The phase difference of the specific MNPs sample can be represented as;

$$\Phi = Sweep_{phase} - System_{phase} \tag{3.2}$$

The relaxation time can be represented as;

$$\tau = \Phi/(180 \times f) \tag{3.3}$$

Here, f is the excitation frequency, Φ is in degrees and τ is the relaxation time of the sample in µs. Effective relaxation time and excitation frequency have an inverse relation.

3.4. Results and Discussions

Perimag® (micromod GmbH, Germany) coated with dextran (surface plain), Synomag (micromod GmbH, Germany) coated with dextran (surface, PEG 25000 OMe), and VivoTrax (Magnetic Insight, USA) coated with carboxydextran (surface plain) were evaluated at 4.6 kHz and 9.9 kHz under the scope of this thesis. Perimag® sample at 9.9 kHz with an excitation field of 15 mT was characterized [55] as shown in Figure 3.5. The odd frequency spectrum of the SPIONs at 9.9 kHz is displayed in Figure 3.5(a). The positive and negative time cycles of the received signal are shown in Figure 3.5(b). Due to the relaxation effect peaks of the positive and negative cycles are shifted from the midpoint of the time cycles. Velocity compensation was applied to positive and negative time signals to achieve positive and negative PSFs, respectively, as displaced in Figure 3.5(c).

Significant characteristics of the Perimag® sample at 9.9 kHz with a 15 mT excitation field are presented in Figure 3.5. Fast Fourier Transform (FFT) behavior of the induced voltage signal of SPIONs at odd multiples (below 20th harmonic) of the 9.9 kHz is displayed in Figure 3.5(a). The absolute voltage of the positive and negative cycles after partitioning with the phase sweep algorithm is shown in Figure 3.5(b). PSF of the sample can be determined from either a positive or negative cycle as presented in Figure 3.5(c). Magnetization response of the sample can be achieved with the integration of the PSF signals. The normalized magnetization output is shown in Figure 3.5(d) resembles the hysteresis loop of the magnetic materials. This hysteresis loop appears due to the relaxation effect of the sample nanoparticles.

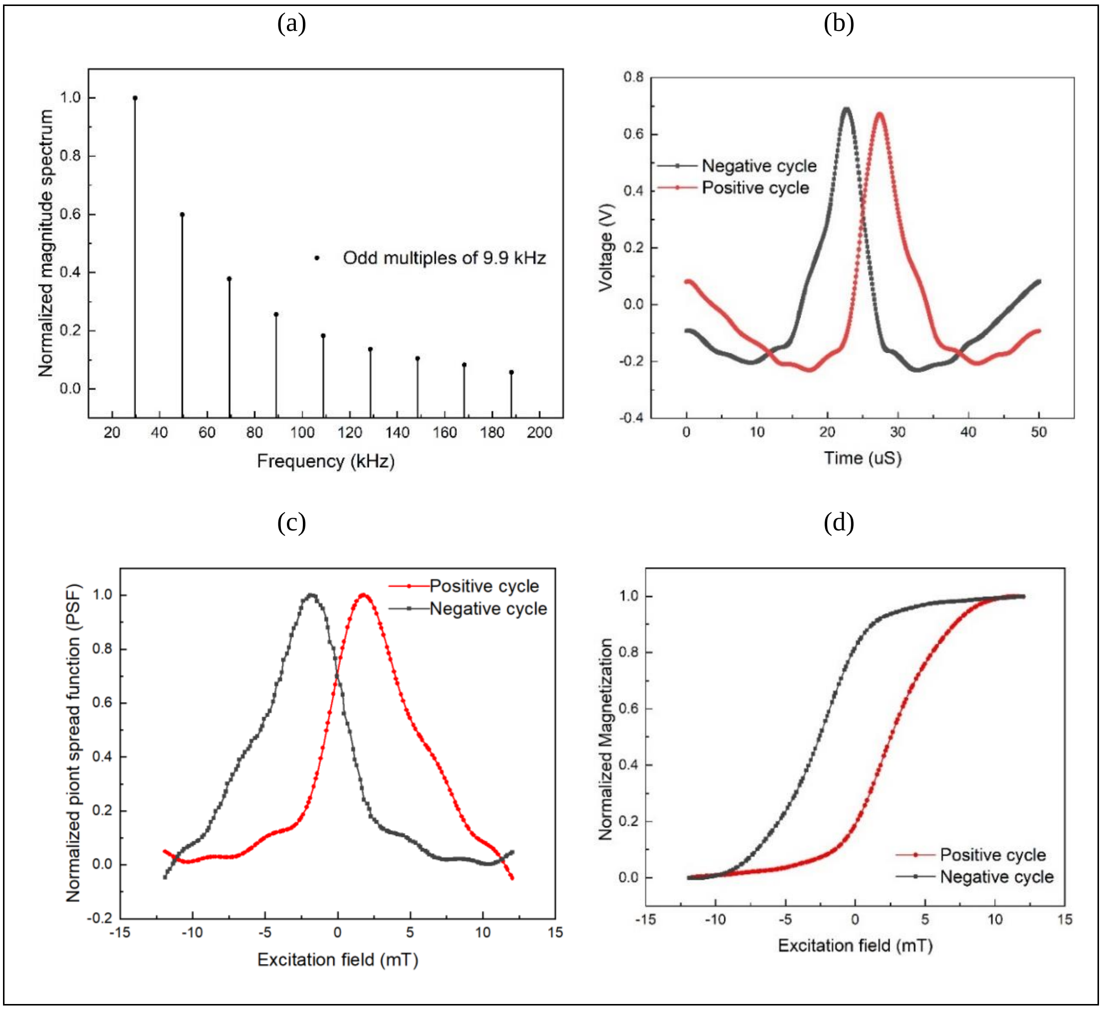

Figure 3.5: Evaluation of Perimag SPIONs at 9.9 kHz with 15 mT (peak amplitude) sinusoidal excitation field; (a) Frequency spectrum of odd harmonics, (b) Induced voltage (time-domain signals) for positive and negative cycles, (c) Normalized point spread functions (PSFs) and (d) Normalized magnetization of the sample.

Post-processing after data recording of the MPS technique uses frequency-domain (FFT response). However, the relaxometer uses the PSF to measure the resolution of the magnetic particles. Relaxation time, FWHM, and relative signal of the samples at 9.9 kHz with excitation field of 15 mT(peak amplitude) are presented in Table 3.2.

Table 3.2: The characteristics of SPIONs at 9.9 kHz with an excitation field of 15 mT.

	5th/3rd harmonic ratio	FWHM (mT)	Relaxation Time (µs)	Relative Signal (mV/mg)
Vivotrax	0.44	8.76	4.09	10.12
Perimag	0.59	6.13	4.06	33.82
Synomag	0.57	7.20	5.26	51.39

Perimag® has the highest 5th/3rd harmonic ratio as compared to the other SPIONs samples. The width of the dynamic range is measured in PSF (FWHM, mT). Excitation frequency was kept constant and magnetic field was reduced to 10 mT and all samples were re-assessed, as presented in Table 3.3. Synomag has the highest relative signal as compared to Vivotrax and Perimag samples.

Table 3.3: The characteristics of SPIONs at 9.9 kHz with an excitation field of 10 mT.

	5th/3rd harmonic ratio	FWHM (mT)	Relaxation Time (µs)	Relative Signal (mV/mg)
Vivotrax	0.38	6.16	4.09	5.39
Perimag	0.51	5.01	4.25	18.63
Synomag	0.46	5.60	5.85	27.78

As the excitation field is reduced, the width of the dynamic range is also reduced. However, relaxation time is not changed significantly with changing applied magnetic field. All samples were evaluated with an applied magnetic field of 5 mT as presented in Table 3.4.

Table 3.4: The characteristics of SPIONs at 9.9 kHz with an excitation field of 5 mT.

	$5^{th}/3^{rd}$ harmonic ratio	FWHM (mT)	Relaxation Time (µs)	Relative Signal (mV/mg)
Vivotrax	0.32	3.58	4.45	1.52
Perimag	0.36	3.33	5.10	5.49
Synomag	0.31	3.52	7.00	8.19

The frequency spectrum, FWHM, and relative signals of all samples increase with increasing of the excitation field strength and vice versa. To observe the excitation frequency effects on the evaluation parameter, the operating frequency was adjusted at 4.6 kHz. Characterization parameters with 15 mT (peak amplitude) are given in Table 3.5.

Table 3.5: The characteristics of SPIONs at 4.6 kHz with an excitation field of 15 mT.

	$5^{th}/3^{rd}$ harmonic ratio	FWHM (mT)	Relaxation Time (µs)	Relative Signal (mV/mg)
Vivotrax	0.43	9.04	9.74	4.89
Perimag	0.62	5.52	9.25	16.86
Synomag	0.56	7.04	11.13	25.42

Relaxation time has become almost double with the decreasing operating frequency by a factor of 2. In addition to this, the relative signal was also reduced by factors of 2 as compared to the relative signals at 9.9 kHz with 15 mT (peak amplitude) applied field strength. All samples were re-assessed at 10 mT excitation field as given in Table 3.6.

Table 3.6: The characteristics of SPIONs at 4.6 kHz with an excitation field of 10 mT.

	$5^{th}/3^{rd}$ harmonic ratio	FWHM (mT)	Relaxation Time (µs)	Relative Signal (mV/mg)
Vivotrax	0.34	6.36	9.68	2.53
Perimag	0.53	4.58	9.74	9.61
Synomag	0.44	5.58	11.91	14.10

As the excitation field is reduced, the width of the dynamic range is also reduced as compared to FWHM at 4.6 kHz with a 15 mT measurement. However, relaxation time is not changed significantly with changing the applied magnetic field. Lastly, all samples were evaluated with an applied magnetic field of 5 mT, as presented in Table 3.7.

Table 3.7: The characteristics of SPIONs at 4.6 kHz with an excitation field of 5 mT.

	$5^{th}/3^{rd}$ harmonic ratio	FWHM (mT)	Relaxation Time (µs)	Relative Signal (mV/mg)
Vivotrax	0.31	3.57	9.74	0.70
Perimag	0.38	3.29	10.76	2.79
Synomag	0.29	3.63	13.48	4.03

Relative signal, resolution (FWHM, mT), and relaxation time of the commercial SPIONs were investigated [55] in this thesis. The resolution in terms of mT range is reduced with increasing the applied magnetic field (5 mT to 15 mT) as presented in Figure 3.6(b). Relaxation times of the samples at 4.6 kHz slightly decreased with increasing the applied magnetic field as shown in Figure 3.6(a). Neel relaxation time reduces drastically with increasing the applied magnetic field. So, overall relaxation time is reduced. The findings of this research are in good agreement with the observation of the references [52, 67]. Perimag® has 3.29 mT FWHM at the lowest applied magnetic field that promises the highest spatial resolution for MPI. The increasing trend of the FWHM (mT) with the applied magnetic field is in good agreement with the observation of other studies [67, 68].

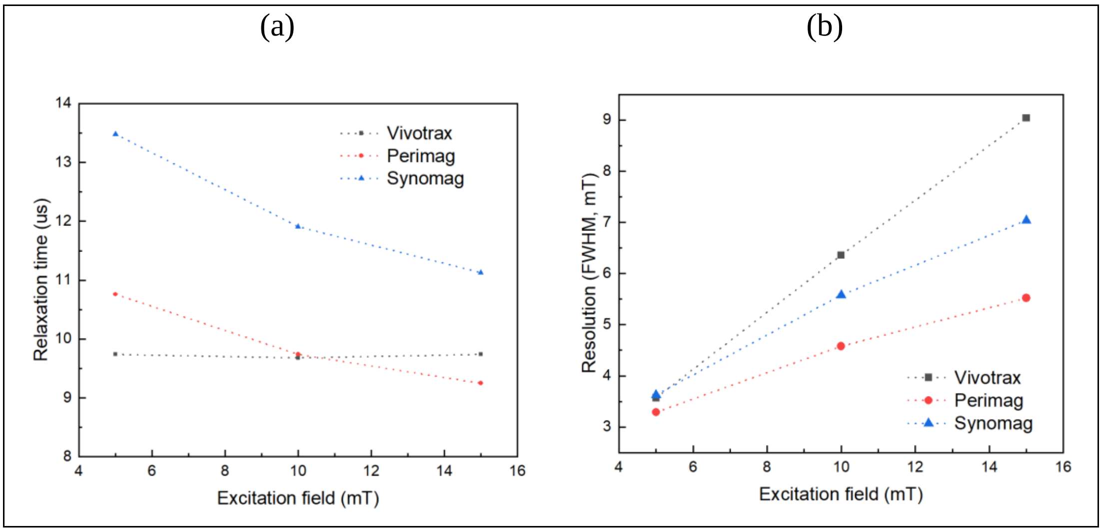

Figure 3.6: The comparison of the Vivotrax, Perimag, and Synomag SPIONs; (a) Effective relaxation time at 4.6 kHz, (b) Resolution (FWHM, mT) at 4.6 kHz.

The resolution of the SPIONs also depends on the bandwidth of the receive coil signal which can be improved by considering higher harmonics. In this study, the first 20 harmonics were used to measure resolution and relaxation time at 4.6 kHz and 9.9 kHz, respectively. The relaxation times at 9.9 kHz are reduced by a factor of 2 as compared to 4.6 kHz, as shown in Figure 3.7(a). Similar to the relaxation times at 4.6 kHz, the decreasing trend is observed at 9.9 kHz with an applied magnetic field (5 mT to 15 mT) as shown in Figure 3.7(b). The FWHM of the samples at 9.9 kHz also showed a similar trend to 4.6 kHz as provided in Figure 3.7(b). The resolution of the SPIONs does not significantly change with the frequency of the applied magnetic field. The resolution of the samples at 4.6 kHz is slightly better than at 9.9 kHz that matches well with the finding of another study for lower excitation fields [68]. Luckily, low excitation fields yield high spatial resolution in MPI because high excitation fields are not permissible due to PNS and SAR limitations.

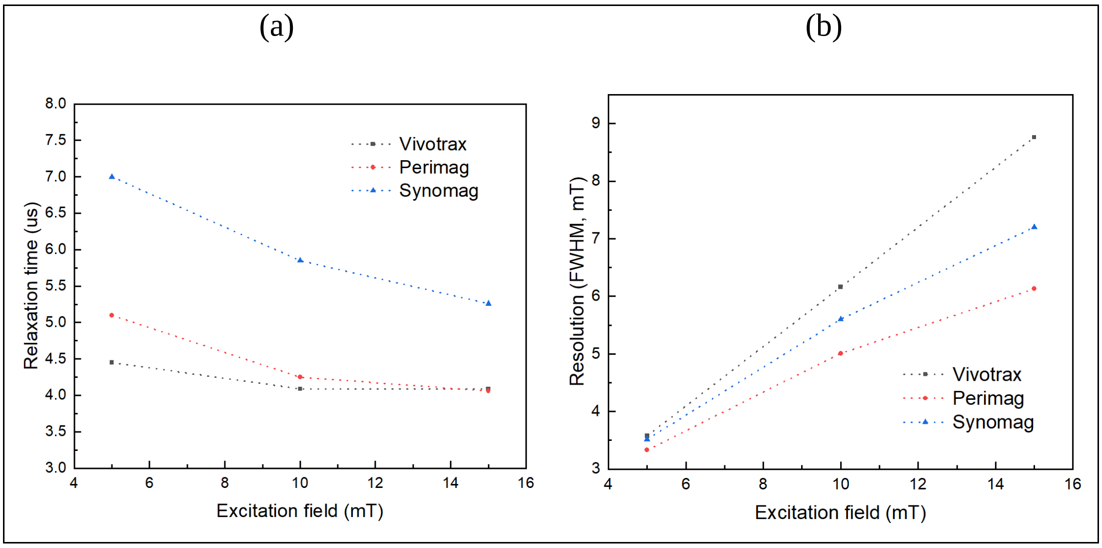

Figure 3.7: The comparison of the Vivotrax, Perimag, and Synomag SPIONs; (a) Effective relaxation time at 9.9 kHz, (b) Resolution (FWHM, mT) at 9.9 kHz.

The frequency response of all samples was compared at 9.9 kHz with a 15 mT excitation field as shown in Figure 3.8(a). Perimag® has the highest (0.59) 5th/3rd harmonics ratio among the other samples. In addition to this, Perimag® shows slow decay of the higher harmonics. The FWHM is minimum for Perimag® among the other samples which help to achieve high spatial resolution as shown in Figure 3.8(b). The results of the FFT response and PSFs of the SPIONs are in good agreement with an arbitrary waveform relaxometer [69].

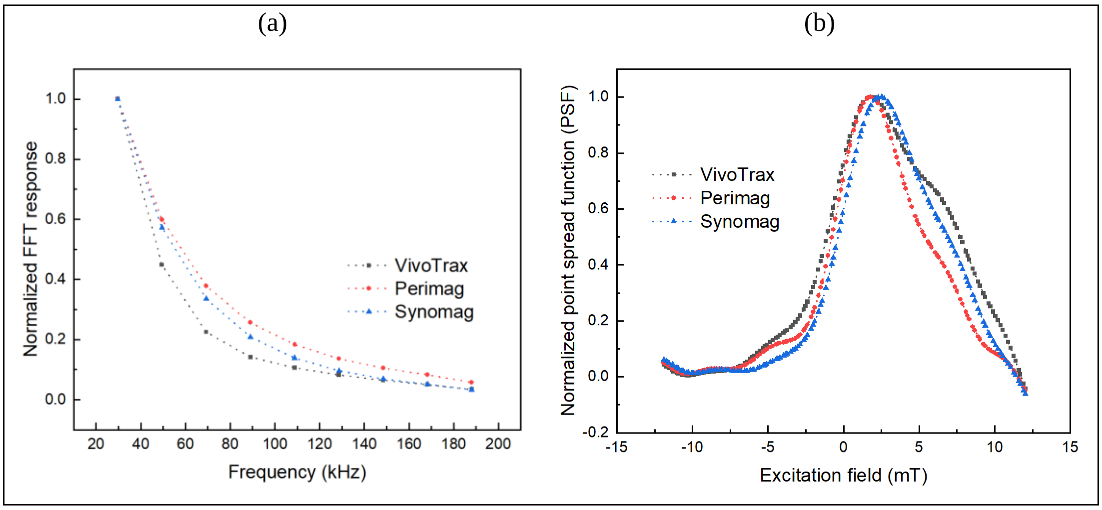

Figure 3.8: Comparison of the nanoparticles at 9.9 kHz with 15 mT (peak amplitude) alternating excitation field; (a) Odd harmonics magnitude response, (b) Resolution in FWHM (mT).

Moreover, the relative signal strength of the Vivotrax, Perimag®, and Synomag samples were normalized with the iron concentration of each sample at 4.6 kHz and 9.9 kHz excitation frequencies as given in Table 3.8. Synomag has the highest signal strength as compared to the other two samples. The relative signal of the tracer agents improves the SNR of the MPI. It is linearly increased with the operating frequency such that the relative signal at 9.9 kHz is twofold of the relative signal at 4.6 kHz.

Table 3.8: Relative signals of standard SPIONs at 9.9 kHz, and 4.6 kHz.

	Signal strength at 9.9 kHz (mV/mg)			Signal strength at 4.6 kHz (mV/mg)		
Excitation field (mT)	15	10	5	15	10	5
Vivotrax	10.10	5.39	1.52	4.89	2.53	0.70
Perimag	33.82	18.63	5.49	16.86	9.61	2.79
Synomag	51.39	27.78	8.19	25.42	14.10	4.03

An in-house MPR was developed for the characterization of the MNPs as a potential tracer agent for MPI usage. The finding of this device helps to optimize the synthesis process of the SPIONs. MPS and MPR are utilized for many applications such as viscosity and temperature mapping of the MNPs [56]. However, it cannot characterize the samples from the specific location of the test object. As it records data from everywhere inside the coaxial drive and receive coil, so it needs an additional mechanism for spatial characterization. In MPI, spatial encoding is utilized to switch off uninterested areas magnetically which will be thoroughly discussed in the 4th chapter.

4. SPATIAL ENCODING TECHNIQUES FOR MPI

Transmit and pick-up coils of MPI do not differentiate inductive signals from different positions as presented in MPR. Therefore, spatially inhomogeneous static magnetic field (also known as selection field) is applied in superposition to the alternating (sinusoidal) excitation field (also known as drive field) for the localization of the SPIONs as tracer agents. The selection field is used to switch off all regions except the region of interest (ROI). Pioneers of the MPI technology have utilized FFP based selection field of 3.4 T/m and 3 T/m gradients with electromagnetic coils [1,70], so the nanoparticles in the vicinity of the FFP (Figure 4.1(a,c)) generate full MPI signal while the nanoparticles at other regions/positions become saturated in the presence of the strong static magnetic field.

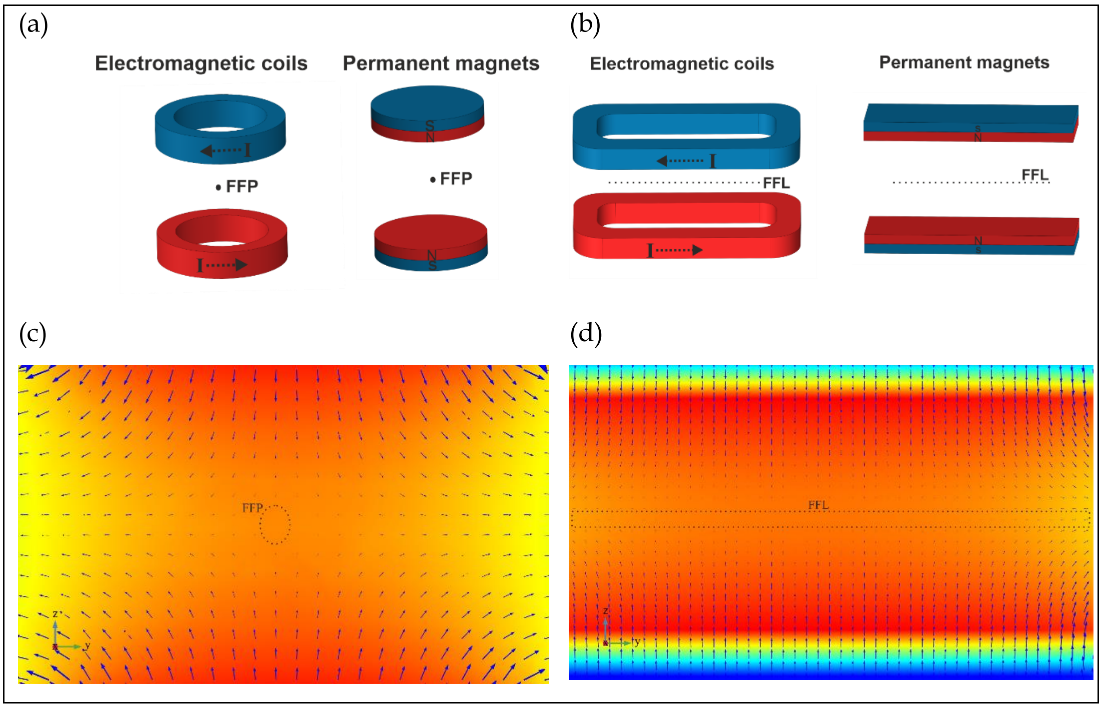

Figure 4.1: Selection fields for MPI scanners; (a) Disc-shaped permanent magnets and ring-shaped electromagnets are commonly used to generate FFP, (b) Rectangular shaped permanent magnets and electromagnets are usually used to achieve FFL, (c) Magnetic field strength pattern of FFP spatial encoding, (d) Magnetic field strength pattern of FFL spatial encoding.

Furthermore, field-free line (FFL) as shown in Figure 4.1(b,d) is another spatial encoding scheme that increases sensitivity, SNR, and temporal resolution of MPI scanners [71,72]. Likewise, a gradient field of 0.7 T/m was generated with permanent magnets to exercise a multi-frequency MPI scanner [73]. A maximum of 7 T/m gradient field has been implemented with permanent magnets so far to produce FFP based MPI scanner [74]. An adjustable gradient field of 3-5.5 T/m implemented with 3 T/m (permanent magnets) and dynamic 2.5 T/m controlled with direct current, was utilized to get a 3D image of the beating mouse heart [1]. Similarly, gradient fields of 4-7 T/m in the literature were used for the imaging of small animals like mice [75]. Moreover, projection-based scanning was carried out with a gradient field of 2.35 T/m (for FFL MPI) to enhance imaging speed [76].

4.1. FFP Spatial Encoding

A large-bore diameter (patient bed), scanning of a large field of view (FOV) in minimum time, and high spatial resolution are the key objectives of MPI scanners. In this thesis, the spatial homogeneity of three different selection fields (implemented with permanent magnets, electromagnets, and a combination of both) was evaluated at the fixed internal working space (distance between two magnet pairs) of 71 mm. The selection fields were modeled with an 11.25% enhanced ratio to the Maxwell configuration length using electromagnetic coils, permanent magnets, and a hybrid system. Spatial homogeneity of the selection fields was evaluated at a higher length than Maxwell configuration to achieve maximum bore size. The gradient field of 4.3 T/m strength was targeted for the MPI scanner that was implemented for phantom imaging. Each topology was analytically and numerically simulated for magnetic flux density and gradient field using MATLAB, and COMSOL Multiphysics, respectively. The relative gradient field strength error of each topology was also calculated. A home-built MPI scanner of permanent-based selection field was implemented, and results were compared with simulation models.

4.2. Selection Field Methods

Permanent magnets and/or electromagnets are used to generate a selection field for MPI scanner. In medical imaging, gradient field homogeneity has special importance for high resolution. Gradient field strength plays a major role to define the field of view (FOV) of a scanning object. A higher gradient field increases spatial resolution of medical imaging; however, it reduces the volume covered by FOV. Theoretically, gradient field (G) strength along the x and y-axes is half of the z-axis value with a negative sign, respectively. Gauss's law of electromagnetism describes the divergence of the magnetic field (B) as mentioned in equation (4.1).

$$G = G_x + G_y + G_z = \nabla \cdot \boldsymbol{B} = \frac{\partial B_x}{\partial x} + \frac{\partial B_y}{\partial y} + \frac{\partial B_{\boldsymbol{z}}}{\partial z} = 0 \qquad (4.1)$$

where $G_x := \frac{\partial B_x}{\partial x}$, $G_y := \frac{\partial B_y}{\partial y}$ and $G_z := \frac{\partial B_z}{\partial z}$

The relationship among three gradient strengths is stated as:

$$G_z = -2G_x = -2G_y \qquad (4.2)$$

The equations (4.1) and (4.2) clearly show the asymmetry of the selection field which has a considerable impact on the spatial resolution of MPI scanners. Asymmetry of the gradient field values produces an ellipsoid shape FOV to scan an object. The highest gradient field along the z-axis produces high spatial resolution. The spatial resolution of MPI scanners [77] along with the system dynamics also depends on a tracer material resolution (FWHM, mT) [78] is expressed in equations (4.3) and (4.4), respectively.

$$\Delta x_{FWHM} = \frac{k_B T}{\mu_0 m G} \Delta \varepsilon_{FWHM} \qquad (4.3)$$

$$\Delta \varepsilon_{FWHM} = 4.16\beta^{-1} \qquad (4.4)$$

where k_B is Boltzmann constant, T is temperature, μ_0 is the magnetic permeability of the vacuum, m is the magnetic moment, $\Delta\varepsilon_{FWHM}$ is the full width at half maximum (FWHM) of the point spread function of the magnetic nanoparticles (tracer material), and β depends on the third power of the core diameter of the magnetic nanoparticles. $\Delta\varepsilon_{FWHM}$ is measured from the derivative of the magnetization characteristics.

Practically, zero-dimensional MPI devices known as magnetic particle spectrometer (MPS) or relaxometer [55] are used to calculate $\Delta\varepsilon_{FWHM}$. The spatial resolution can also be calculated from the overall point spread function of MPI scanners with a point source scanning. Likewise, Δx_{FWHM} is the FWHM resolution of MPI imaging devices. The resolution of the device mainly depends on the gradient field strength (a higher value of the gradient field increases the resolution of MPI scanners). It also depends on the SNR of the imaging device (MPI scanner) and the deconvolution effect. However, in the scope of this research, only the FWHM approach is utilized. The resolution along the x and y-axis is at least two times lower than the z-axis, as presented in equation (4.2).

Permanent magnets (PM), electromagnets (EM), and hybrid (PM&EM) system-based selection fields were compared at an internal working space of 71 mm. Each selection field setup consists of two spatially separated parts and their magnetic fields are opposite to each other to form FFP spatial encoding. The size (radius R) and distance between two centers $\sqrt{3}R$ of the selection field pair were calculated based on Maxwell configuration [15]. Ring-shaped electromagnets were used with a different internal and outer radius, so average radius (R_{avg}) was utilized to calculate Maxwell length for the comparison among other setups. To achieve a wider working space, the distance between the selection field pair was enhanced based on the additional distance to the thickness ($d_a/2L$) ratio. The average radius of the ring-shaped electromagnets can be expressed as;

$$R_{avg} = \frac{R_{in} + R_{out}}{2} \tag{4.5}$$

where R_{in} and R_{out} are internal and external diameters of the ring-shaped electromagnets.

An internal working space (surface-to-surface distance) can be enhanced by placing permanent magnets and/or electromagnets at a larger distance than Maxwell length. So, additional distance (d_a) can be evaluated as:

$$d_a = 2d - \sqrt{3}R \tag{4.6}$$

where d is the distance between the center of the selection field setup and the midpoint of each-sided permanent magnet or electromagnet. R is the radius of the permanent magnets and the average radius of the electromagnets.

Physical dimensions of permanent magnets and/or electromagnets used in the selection field setups are presented in Table 4.1. In this study, an internal working space of 71 mm and an enhanced ratio ($d_a/2L$) of 11.25% were kept constant among the selection field topologies. Magnetic flux density and gradient field strength of each setup was evaluated over a 40 mm ROI with MATLAB and numerically simulated in COMSOL, respectively. Moreover, the selection field with disc-shaped permanent magnets was experimentally implemented.

Table 4.1: Physical dimensions of the selection field topologies.

Topology	Dimensions (mm)	Maxwell length (mm)	Practical length 2d (mm)	Enhanced ratio ($d_a/2L$)
PM	R = 50, L = 20	86.5	91	11.25%
EM	R_{in} = 52, R_{out} = 101.76	133	151	11.25%
	R_{avg} = 76.88, L = 80			
Hybrid	PM→ R = 50, L = 10	86.5	88.75	
	EM→ R_{in} = 52, R_{out} = 75.76	110.525	122	11.25%
	R_{avg} = 63.88, L=51			

4.2.1. Selection Field Design with Permanent Magnets

Two pairs of NdFeB permanent magnets were used to obtain a gradient field of 4.3 T/m for the phantom imaging MPI scanner. The permanent magnets of each having 0.88 T remanent flux density were utilized and mounted with opposite poles as shown in Figure 4.2. Each permanent magnet has a 100 mm diameter, and 10 mm thickness. Magnetic flux density was strengthened by combining these two magnets. One of the magnet pairs is placed at the +d (distance), and another at the -d symmetrically along the z-axis.

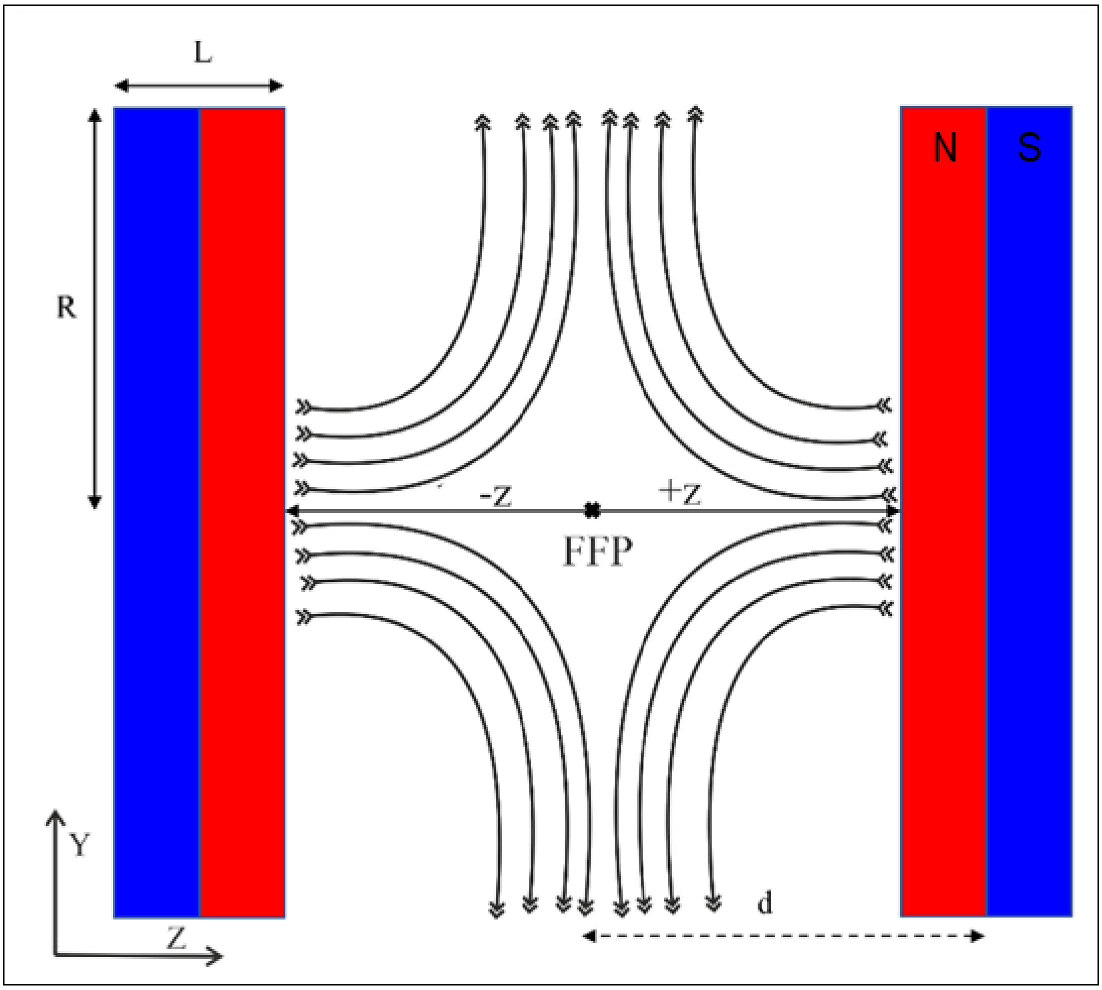

Figure 4.2: Arrangement of the permanent magnets design for the selection field. L is the length, and R is the radius of the permanent magnets.

The distance from the origin of the system to the midpoint of the permanent magnets is represented with d, and z donates the measurement variable from -30 mm to 30 mm. N and S represent the north and south poles of the permanent magnets, respectively. The permanent magnet pairs were placed along the z-axis at +45.5 mm and -45.5 mm from the center of the selection field setup, the distance between two magnet pairs (surface-to-surface) is 71 mm which is used to place copper shielding, transmit and receive coils, and experimental object in closed bore size of 40 mm diameter. The magnetic fields of the right and left magnet pairs cancel each other at the z = 0 (midpoint) due to the opposite pole placement. Consequently, a zero magnetic field point is produced at the middle of the setup that is the main source of FFP spatial encoding. MPI scanning is performed through the translation of FFP over ROI. The magnetic flux density of the disc shape permanent magnets (PM) is analytically simulated in MATLAB.

The magnetic flux density produced by the right-side magnets at +d distance from the midpoint is calculated [79] by using equation (4.7).

$$B_{PM-R}(z) = \frac{B_r}{2}\left[\frac{z-d+\frac{L}{2}}{\sqrt{R^2+(z-d+\frac{L}{2})^2}} - \frac{z-d-\frac{L}{2}}{\sqrt{R^2+(z-d-\frac{L}{2})^2}}\right] \quad \text{for } (-d+\tfrac{L}{2}) < z < (d-\tfrac{L}{2}) \tag{4.7}$$

where B_r is the remanent flux density, R is the radius, L is the thickness, and d is the distance from the center of the disc type permanent magnets from the midpoint.

The magnetic flux density produced by the left-side magnets at -d distance from the midpoint is expressed as:

$$\mathrm{B_{PM-L}(z)} = \frac{-\mathrm{B_r}}{2}\left[\frac{\mathrm{z+d+\frac{L}{2}}}{\sqrt{\mathrm{R^2+(z+d+\frac{L}{2})^2}}} - \frac{\mathrm{z+d-\frac{L}{2}}}{\sqrt{\mathrm{R^2+(z+d-\frac{L}{2})^2}}}\right] \quad \text{for } \left(-d+\frac{L}{2}\right) < z < \left(d-\frac{L}{2}\right) \tag{4.8}$$

The magnetic flux density of the magnets linearly decays on either side (towards the middle point) along the z-axis with peak values at |d|. Anti-symmetric responses from each side cancel the magnetic field in the middle of the system. Overall, the magnetic flux density of the system due to the permanent magnets (PM) is the sum of the B_{PM-R} (at the right side) and B_{PM-L} (at the left side) as given:

$$B_{PM}(z) = B_{PM-R} + B_{PM-L} \tag{4.9}$$

The gradient field strength due to the permanent magnets in the z-direction is given by;

$$G_z^{PM} = \frac{\Delta B_{PM}}{\Delta z} := \frac{\partial B_{PM}}{\partial z} \tag{4.10}$$

The selection field setup with the permanent magnets was numerically simulated in COMSOL Multiphysics. The magnets were enclosed in the air sphere of 200 mm with its edge thickness of 50 mm in COMSOL. The main aim of the air sphere is to ensure no magnetic fields in the surroundings of the permanent magnets. The air sphere less than 200 mm radius does affect the magnetic flux density produced by the magnet pairs. A free triangular mesh was used in the entire geometry with a maximum and minimum element size of 1 mm, and 0.011 mm, respectively. The magnetic flux density of the permanent magnets in the 2D axisymmetric space dimension with the revolved angle from -90° to 225° is shown in Figure 4.3(a). To elaborate on the FFP, the same setup was simulated in 3D space and the y-z plane image of magnetic flux density is presented in Figure 4.3(b).

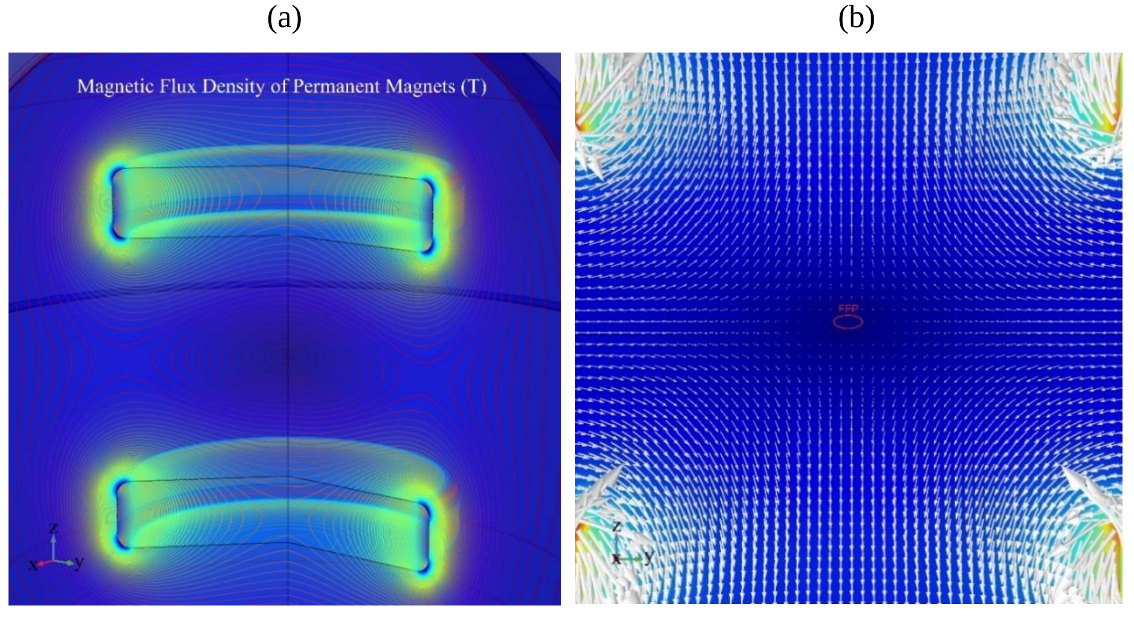

Figure 4.3: Magnetic flux density (T) of NdFeB permanent magnets. (a) 2D axisymmetric simulation of the setup and transparent view from -90° to 225°. (b) 3D simulation of the setup with arrow representation in the y-z plane. Field free point (FFP) is highlighted with a red oval shape in the y-z plane.

Magnetic flux density is linearly increasing on either side of the FFP as presented in Figure 4.5(a). The homogeneous excitation field of the drive coil is used to change the FFP location over a scanning object for diagnosis within defined FOV. Alternatively, an object can also be translated at the fixed FFP location of the gradient setup. The measured values of magnetic flux density are the same as the simulation results at the ROI, except the region near the outer surface of the magnet pairs (Figure 4.5(a)).

The gradient field strength is highly uniform (95%) in [-20, 20] mm interval along the x-axis which defines the homogeneity of the magnetic particle imaging system, as shown in Figure 4.5(b). MPI scanner of 4.3 T/m gradient field was implemented under the scope of this thesis as shown in Figure 4.4 and magnetic flux densities were evaluated.

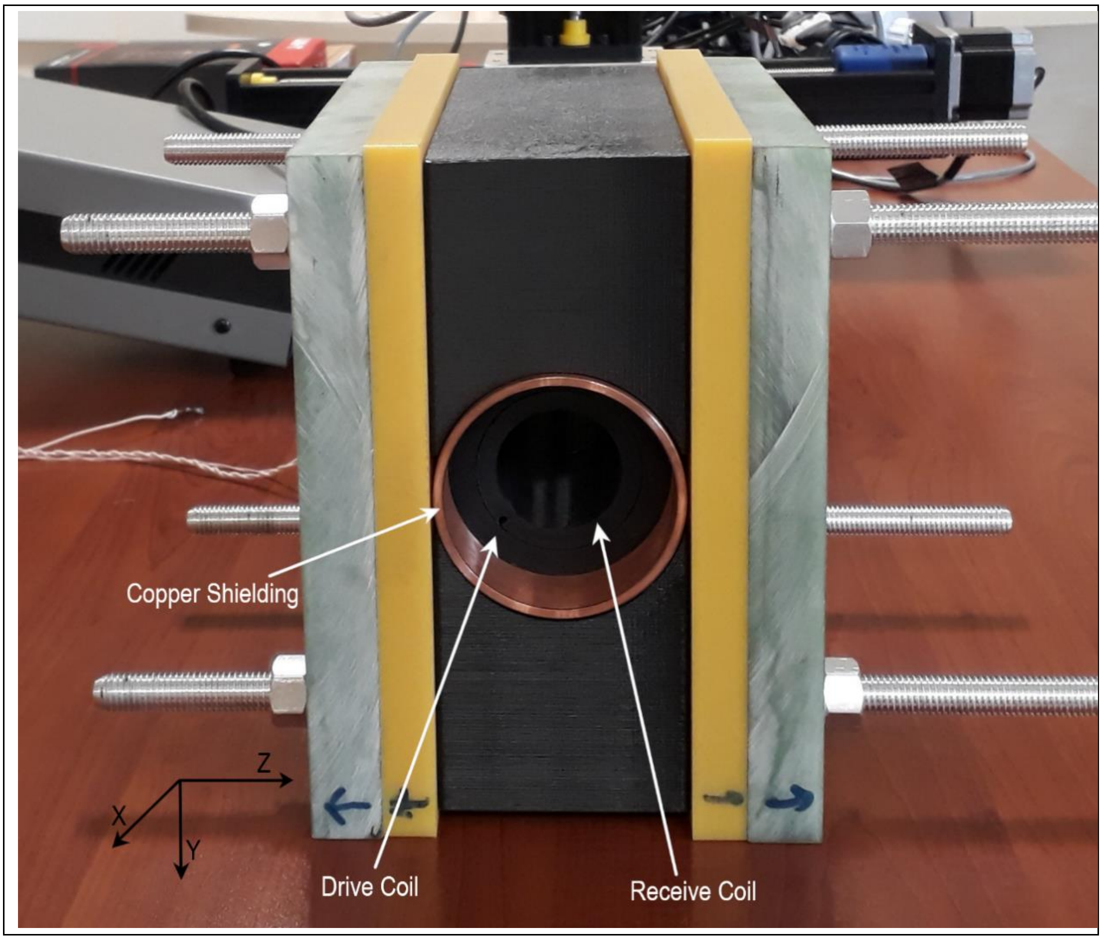

Figure 4.4: Magnetic particle imager hardware. Experimental hardware structure for the selection field (permanent magnets are hidden inside the holders).

The axial probe of DSP (Lakeshore) was used to measure the selection field values in the xz plane along the bore axis (x-axis) at y=0 as shown in Figure 4.6(a). Similarly, the transverse probe was used to measure the magnetic field in the x-z plane perpendicular to the bore axis (along the z-axis) as presented in Figure 4.6(b).

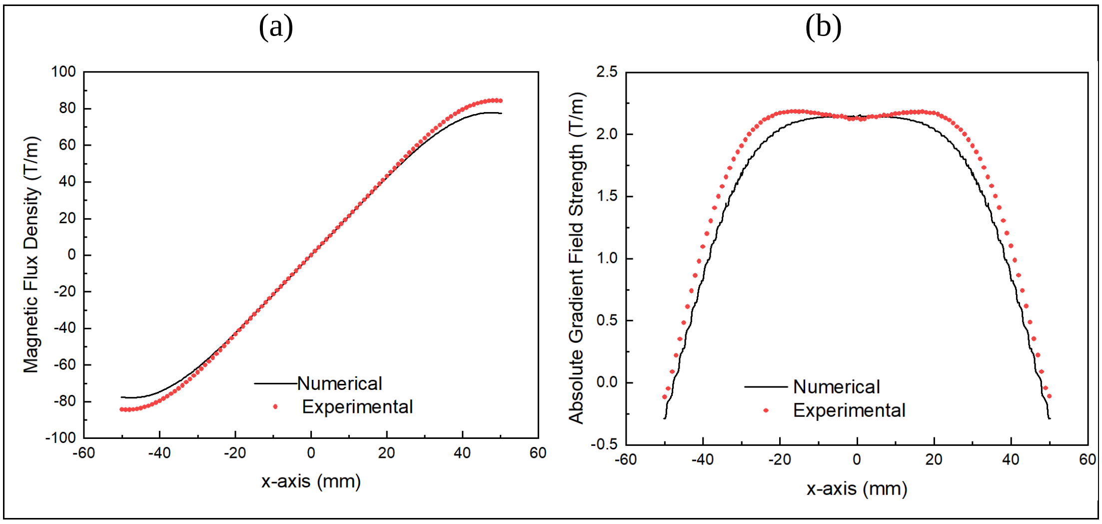

Figure 4.5: (a) Line graph of magnetic flux density along the x-axis. Zero magnetic field at x = 0 demonstrates the Field Free Point (FFP), (b) the gradient field strength of NdFeB magnets along the x-axis.

The magnetic field at the FFP position is theoretically zero, however, the experimental result shows a magnetic flux density of 4 µT which can be considered as zero. The magnetic gradient field of 2.144 T/m was obtained from COMSOL whereas 2.131 T/m was achieved experimentally for the same parameters. Hence, the relative gradient field strength error of 0.58% was observed in the simulation and experimental results at the FFP.

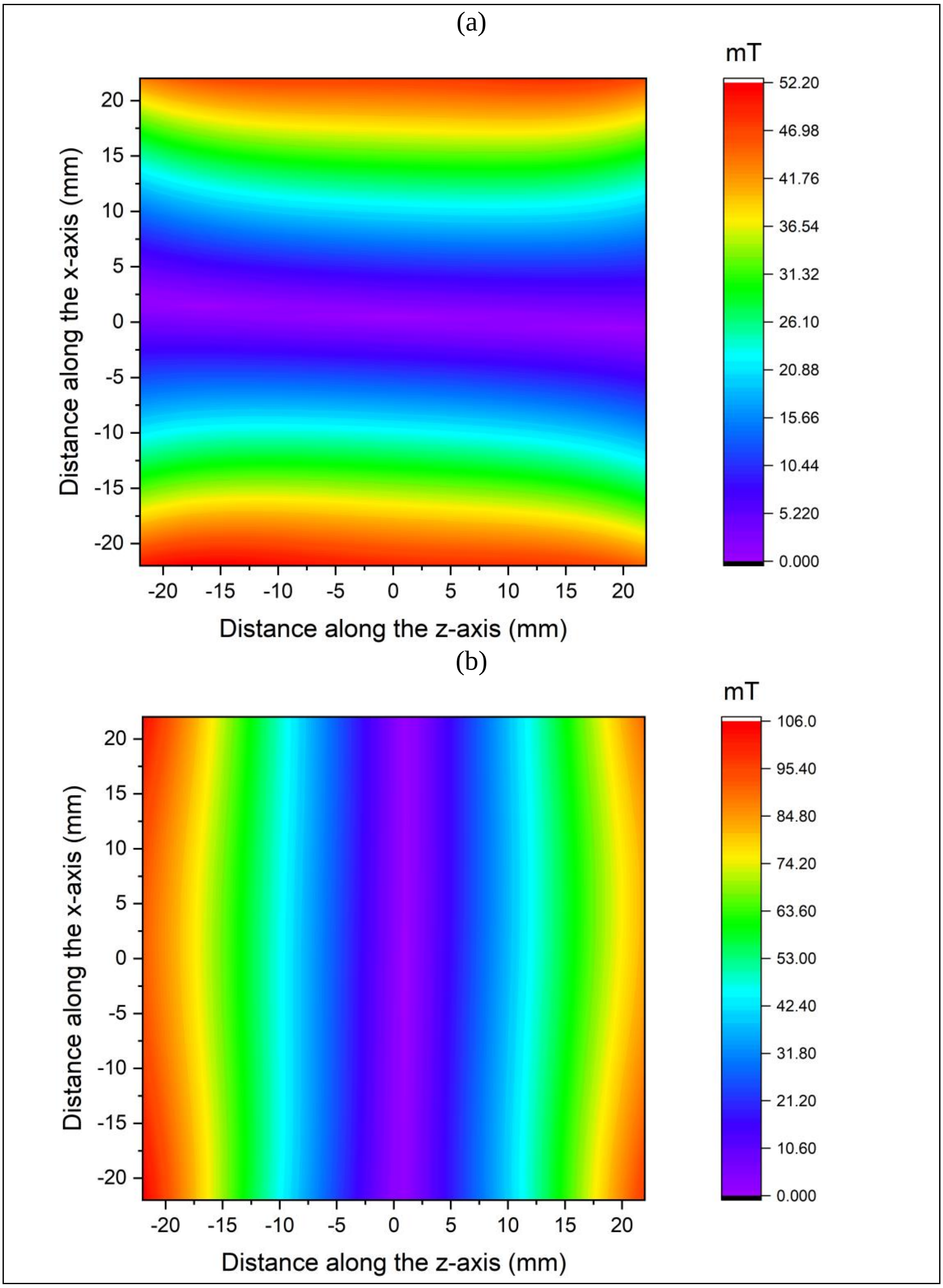

Figure 4.6: Experimental results of the permanent magnets-based selection field. (a) B_x magnetic field in xz plane at y=0, (b) B_z magnetic field in xz plane at y=0.

Overall, the magnetic flux density in the x-z plane is shown in Figure 4.7 and the oval shape of the color patterns shows the asymmetry of the selection field. To achieve a large uniform gradient field interval, the radius (or length) of the permanent magnet should be increased accordingly. The values of the magnetic and gradient fields along x and y are half of the z-axis values as mentioned in equations (4.1) and (4.2).

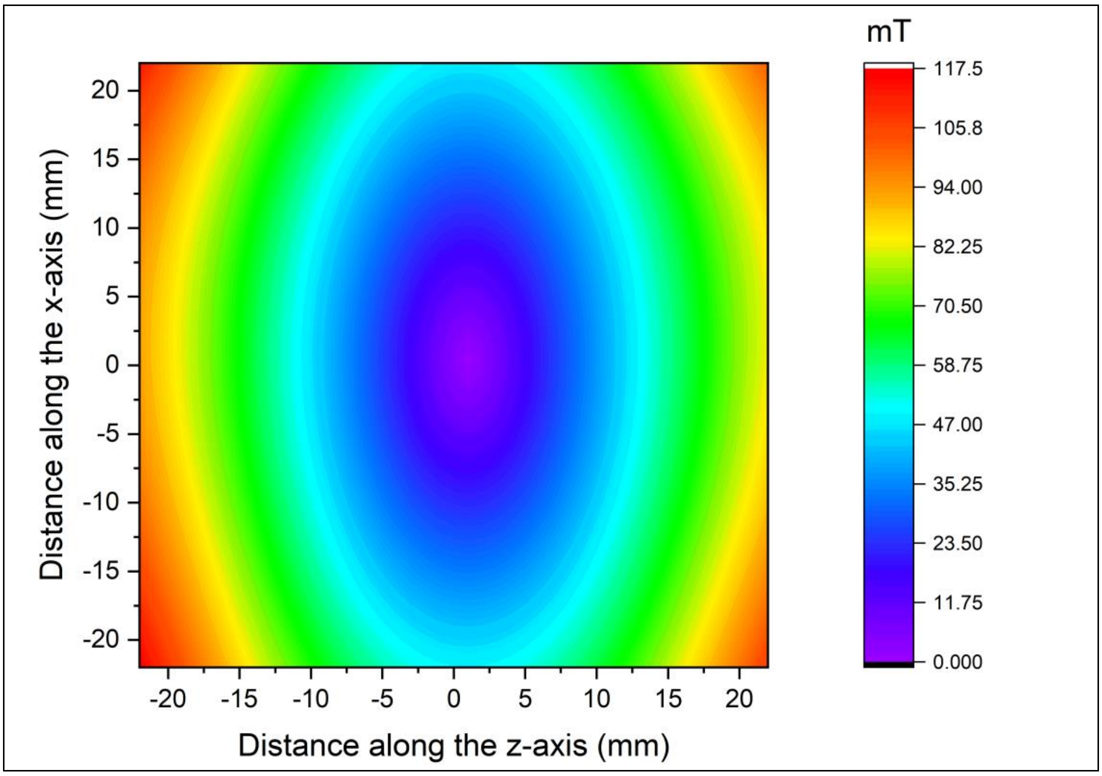

Figure 4.7: Magnetic flux density in xz plane at y=0, Field Free Point (FFP) is demonstrated at the middle-point with zero field.

4.2.2. Selection Field Design with Electromagnetic Coils

Ring-shaped electromagnetic coils were designed and simulated to generate a selection field for a new MPI scanner. The average radius of the electromagnetic coils was utilized, as mentioned in equation (4.5), to calculate Maxwell length. The coils were placed at ± 75.5 mm of practical length, as shown in Figure 4.8. The electromagnetic coil of the outer diameter of 203.52 mm, the inner diameter of 104 mm, and the thickness of 80 mm was designed based on the internal working space of 71 mm between these two electromagnetic coils. Each electromagnetic coil was made of 29 layers with 1363 turns of magnet wire (diameter of the magnet wire is 1.7 mm). The space between the coils was effectively used to place drive and receive coils, and also a cylindrical bore size of 40 mm. The coils were assembled on the z-axis symmetric around the center of the setup. A direct current (DC) of 26.75 A was applied in the opposite direction to each coil to produce FFP spatial encoding. The arrow signs in Figure 4.8 show the current directions in the electromagnetic coils. The FFP is generated when magnetic fields of the same magnitude with opposite directions cancel each other in the middle region. Similar to the permanent magnet design, the FFP lies at z = 0.

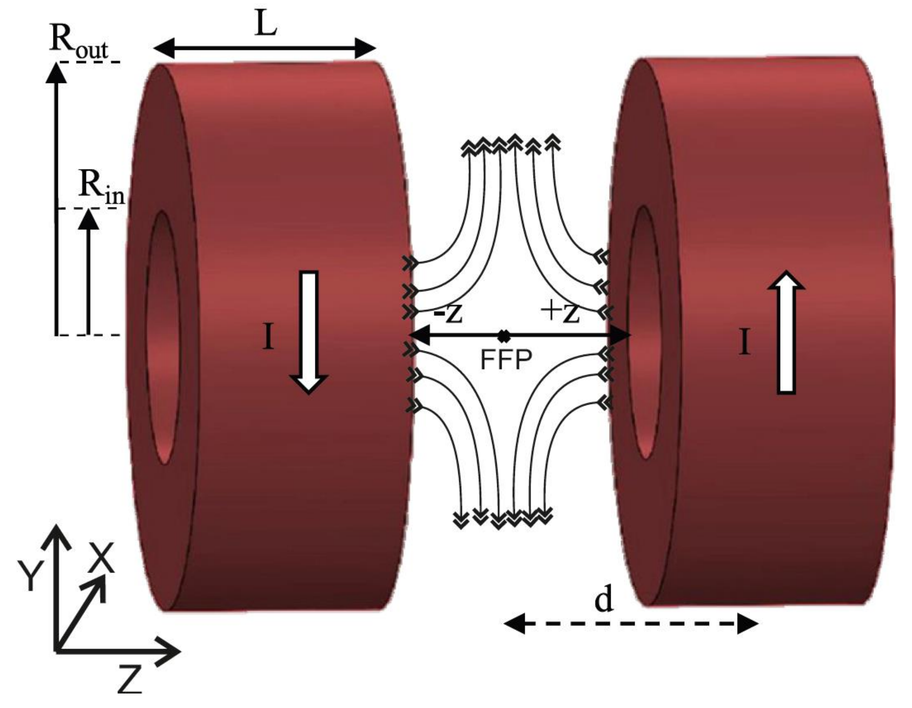

Figure 4.8: 3D view of the electromagnetic coils for the selection field. L is the thickness; R_{in} is the inner and R_{out} is the outer radius of the electromagnets. The current (I) direction in both electromagnets is represented with the arrow signs.

The magnetic flux density produced by the right-side multi-layer electromagnetic coil [80] at +d distance from the origin is theoretically calculated by using equation (4.11).

$$B_{EM\_R}(z) = \frac{\mu_0 N I}{2L(R_{out} - R_{in})}\left[A \ln\frac{R_{out} + \sqrt{R_{out}^2 + A^2}}{R_{in} + \sqrt{R_{in}^2 + A^2}} + B \ln\frac{R_{out} + \sqrt{R_{out}^2 + B^2}}{R_{in} + \sqrt{R_{in}^2 + B^2}}\right] \tag{4.11}$$

where $A = \frac{L}{2} - (z - d),\ B = \frac{L}{2} + (z - d)$, and $(-d + \frac{L}{2}) < z < (d - \frac{L}{2})$

R

R_{out} is the outer radius, R_{in} is the inner radius, L is the thickness, I is the current passing through the coil, N is the number of turns, and μ_0 is the permittivity of the air. The magnetic flux density produced by the left-side electromagnetic coil at -d distance from the origin is expressed as:

$$B_{EM\_L}(z) = \frac{\mu_0 N(-I)}{2L(R_{out} - R_{in})}[A\,ln\frac{R_{out} + \sqrt{R_{out}^2 + A^2}}{R_{in} + \sqrt{R_{in}^2 + A^2}} + B\,ln\frac{R_{out} + \sqrt{R_{out}^2 + B^2}}{R_{in} + \sqrt{R_{in}^2 + B^2}}] \tag{4.12}$$

where $A = \frac{L}{2} - (z - d)$, $B = \frac{L}{2} + (z - d)$, and $(-d + \frac{L}{2}) < z < (d - \frac{L}{2})$.

The magnetic flux density of the electromagnets linearly increases on either side (going away from the middle of the design) along the z-axis with peak values at |d|. Anti-symmetric responses from each side cancel the magnetic field at the central point of the geometry. Thus, the magnetic flux density of the electromagnet (EM) coils system is the sum of $B_{EM\text{-}R}$ and $B_{EM\text{-}L}$ like equation (4.9).

$$B_{EM}(z) = B_{EM\_R} + B_{EM\_L} \tag{4.13}$$

The gradient field strength due to the electromagnets in the z-direction is given by;

$$G_z^{EM} = \frac{\Delta B_{EM}}{\Delta z} := \frac{\partial B_{EM}}{\partial z} \tag{4.14}$$

The gradient field strength of the electromagnets was computed by applying equation (4.13) to equation (4.14). The magnetic flux density of the proposed setup is shown in Figure 4.9.

Similar to the previous topology, the electromagnetic coils were also spherically enclosed in the air with a radius of 400 mm, and a thickness of 30 mm. The radius of the sphere is very significant for an accurate evaluation of the selection field generated by the electromagnets. A free triangular mesh was placed in the entire geometry with a maximum and minimum element size of 1 mm, and 0.011 mm, respectively. The magnetic flux density of the electromagnets in the 2D axisymmetric space dimension with the revolved angle from -90° to 225° is shown in Figure 4.9(a). To elaborate on the FFP, the same setup was simulated in 3D space (spatial domain) and the y-z plane image of the magnetic flux density is presented in Figure 4.9(b). The magnetic flux density of the electromagnetic coils as mentioned in equation (4.13) along the z-axis and its gradient strength by applying equation (4.14) were also computed in MATLAB. The magnetic gradient field of 4.305 T/m was calculated in MATLAB whereas 4.299

T/m was achieved in COMSOL for the same parameters. Hence, the relative gradient field error of 0.13% was observed in the analytical and numerical simulation results at the FFP.

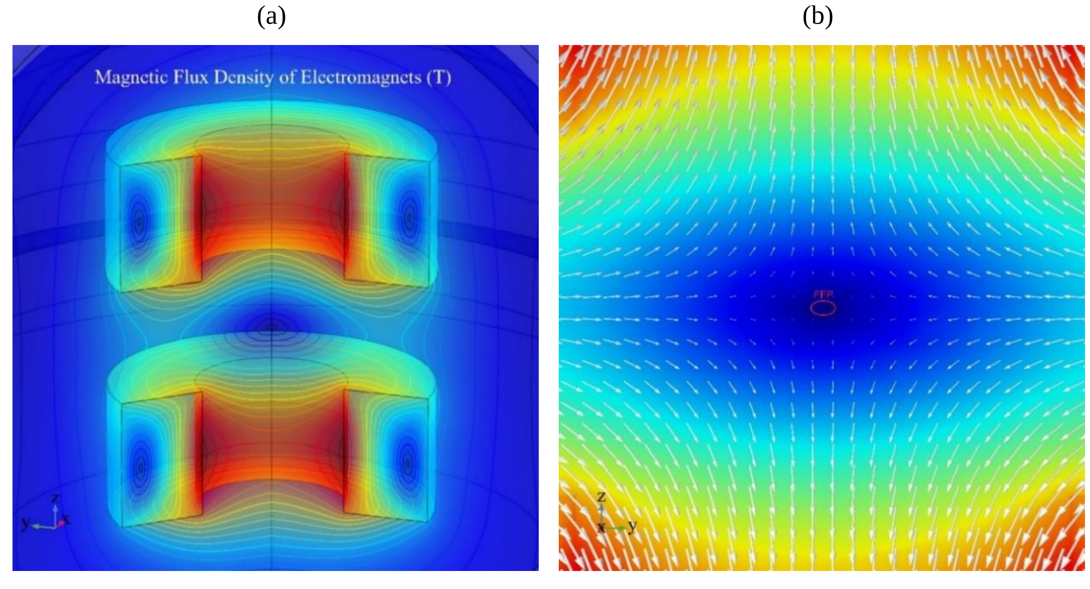
(a)
(b)

Figure 4.9: Magnetic flux density (T) of the electromagnets-based selection field setup. (a) 2D axisymmetric simulation of the setup and transparent view from -90° to 225°. (b) 3D simulation of the setup with arrow representation in the y-z plane. Field Free Point (FFP) is highlighted with the red oval shape in the y-z plane.

The magnetic flux density is linearly increasing on either side (going away from the central point) of the FFP along the z-axis as shown in Figure 4.10(a). Analytical simulation (MATLAB) and numerical simulation (COMSOL) results are well matched at each point along the scanning axis. The gradient field strength is highly homogeneous (97.5%) in [-20, 20] mm interval as presented in Figure 4.10(b).

The uniform gradient field is very important inside FOV in which helps to detect an accurate response of the tracer material and minimize the wrapping artifacts. The transverse gradient field is uniform with just 2.5% fluctuation within the 40 mm of centrally positioned at the FFP.

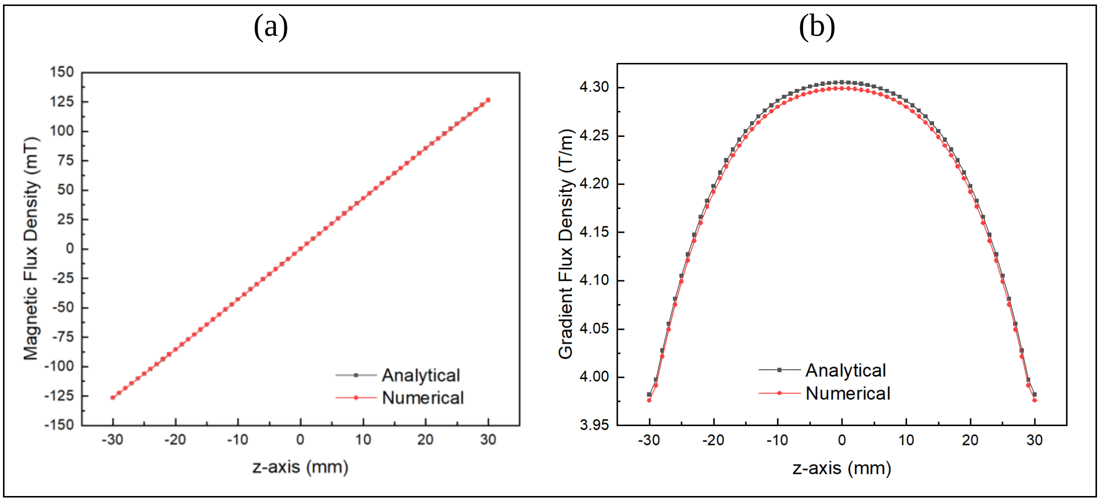

Figure 4.10: (a) Magnetic flux density of the electromagnets along the z-axis. The magnetic field at z = 0 demonstrates the Field Free Point (FFP), (b) the gradient field strength of the electromagnets along the z-axis.

4.2.3. Selection Field Design with Hybrid System

The proposed topology consists of NdFeB permanent magnets and electromagnetic coils pairs to establish a 4.3 T/m gradient field for the magnetic particle imaging device. The selection field setup based on solely electromagnetic coils can produce huge power dissipation and requires a large cooling system. A gradient field generation from electromagnets also requires large power amplifiers. To reduce power requirement, a combination of the previous topologies (PM and EM) was used together to achieve the same gradient field as shown in Figure 4.11. The permanent magnets (PM) and electromagnetic (EM) coils were mounted on the z-axis symmetrically at z = 0. A hybrid selection field setup was designed at the enhanced ratio of 11.25% to obtain a similar internal working space of 71 mm along the z-axis. The permanent magnet pair of 100 mm diameter and a thickness of 10 mm was used. Their outer diameter of 151.52 mm, the inner diameter of 104 mm, and a thickness of 51 mm the electromagnetic coils were designed. South poles of the permanent magnets were placed face-to-face, so the magnetic field of the permanent magnets cancels each other in the middle point. Similarly, direct current passes through the electromagnets in the opposite direction as represented with the arrow signs in Figure 4.11.

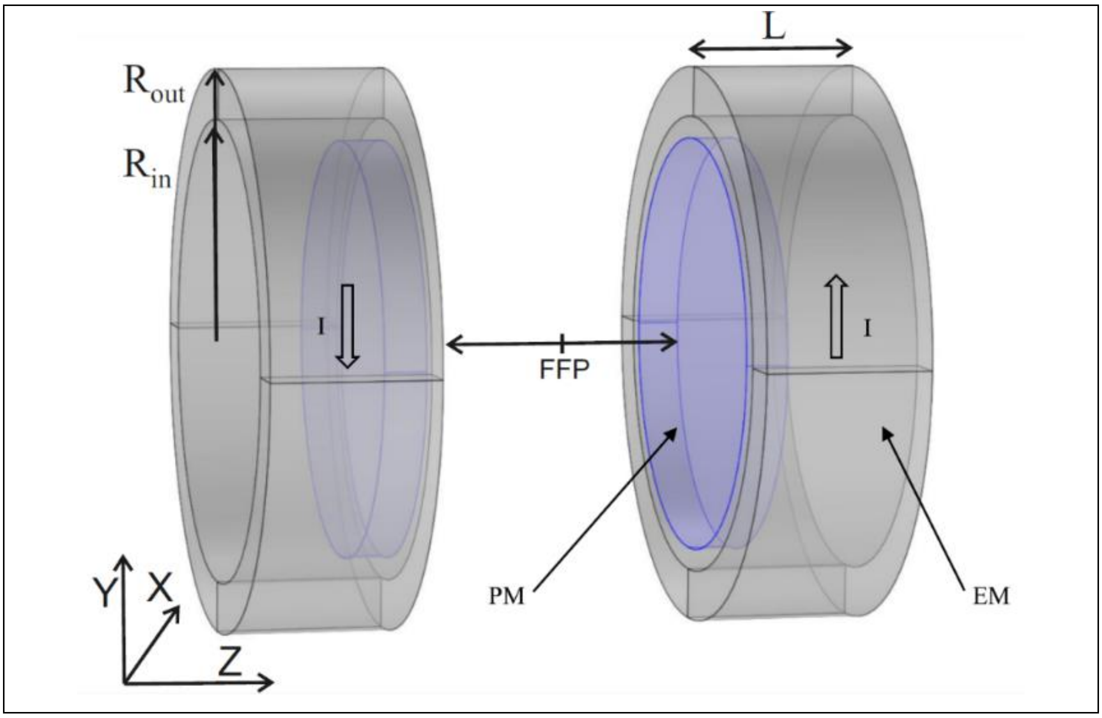

Figure 4.11: 3D transparent view of the combined topology of the disc type permanent magnet and ring-shaped electromagnetic coils. The current (I) direction of the electromagnets is represented with arrow directions. The permanent magnets (PM) are kept inside the electromagnets (EM) for effective usage.

Gradient field strength generated by the electromagnets directly depends on the electric current magnitude, so it can be changed and controlled within a certain range. Controllability of electric current brings useful applications of the gradient field for MPI scanners. The combined topology is a cost-effective technique in comparison to the electromagnet topology for the implementation of adjustable gradient field strength. Moreover, the all-time existence of the selection field from the permanent magnets does not have side effects on patients. The selection field achieved with the permanent magnets or a hybrid system does not produce heating or induce stimulation with static field [81, 82]. Maximum magnetic fields are produced at the center of permanent magnets and electromagnets. However, the magnetic fields inside the FOV are very limited. So, it does not affect the test object if it is slowly translated to avoid dB/dt effects [32].

The permanent magnets having a remanent flux density of 0.88 T were used similar to the prior design, and a gradient field of 2.2 T/m was obtained as presented in Figure 4.12(a). The electromagnetic coil consists of 14 layers with an overall 420 number of turns of the magnet wire of 1.7 mm (diameter). A direct current (DC) of

28.4 A was applied to the electromagnetic coils, and a gradient field of 2.2 T/m was achieved as shown in Figure 4.12(b). Opposite poles placement of the permanent magnets, and reverse current direction in the electromagnetic coils generate zero field point which is visible clearly at z = 0 in Figure 4.13(a).

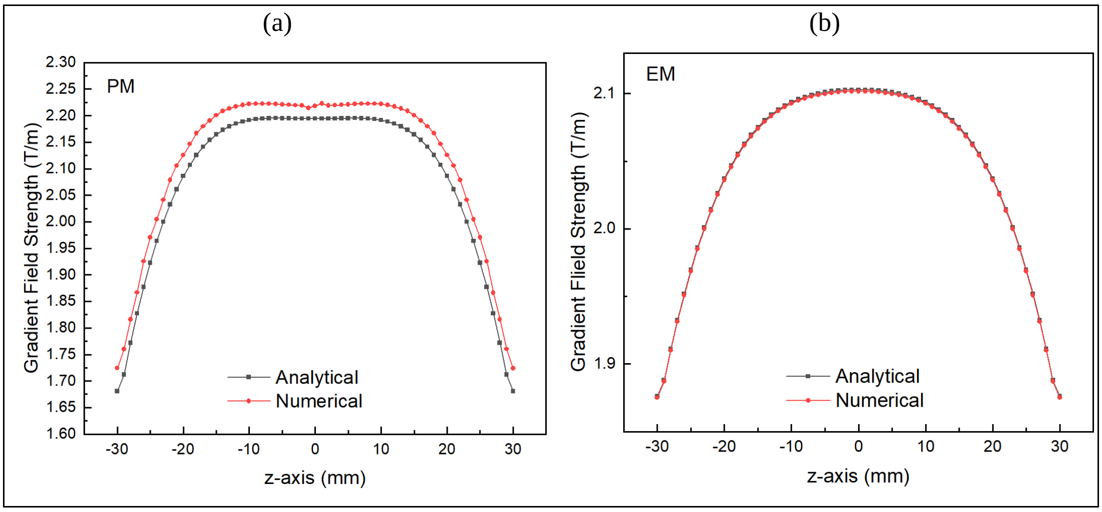

Figure 4.12: Gradient field strength along the z-axis. (a) The gradient of the selection field produced with the permanent magnets, (b) Gradient of the selection field produced with the electromagnets.

The magnetic flux density and gradient field of the permanent magnets and the electromagnetic coils-based selection field setup were also analyzed by using equations (4.7-4.14) for the combined topology in MATLAB. The magnetic field from the COMSOL simulation at the field-free point was 5.7 µT which can be ignored and considered as zero. A gradient field of 4.297 T/m was calculated in MATLAB whereas 4.310 T/m was achieved in COMSOL for using the same parameters. Hence, the relative gradient field error of 0.3% was observed in our analytical and numerical simulation results at the FFP. The overall gradient field strength of 4.3 T/m was obtained from the combination of both permanent magnets and electromagnetic coils as shown in Figure 4.13(b). The transverse gradient field is homogeneous (96.8%) with a maximum of 3.2% relative fluctuation within 40 mm of centrally positioned FFP for both simulation and calculation.

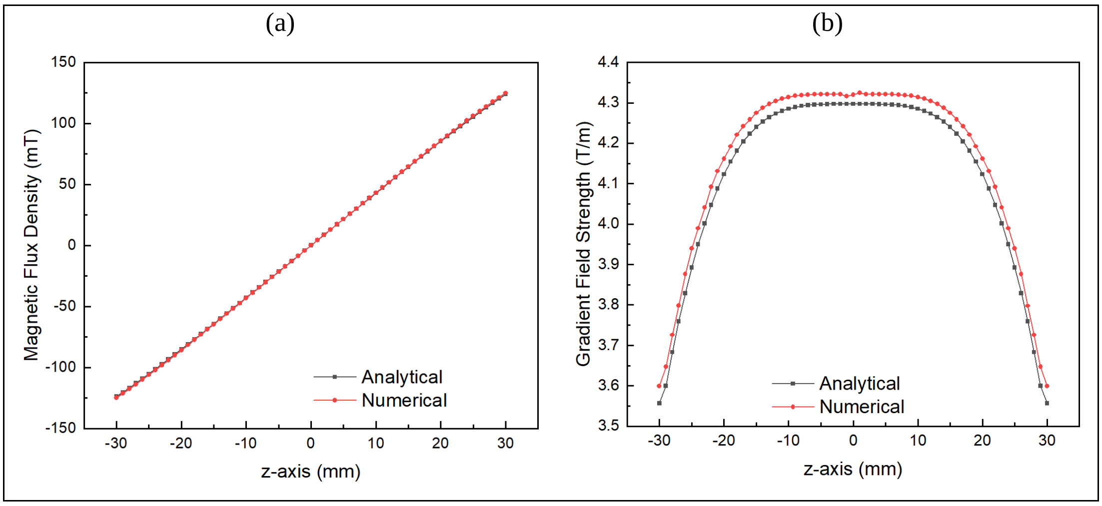

Figure 4.13: (a) Line graph of magnetic flux density along the z-axis. Zero magnetic fields at z = 0 demonstrate the Field Free Point (FFP), (b) the gradient field strength of the combined topology along the z-axis.

4.3. Results and Discussions

In this study, the three different topologies were modeled and simulated to generate a gradient field of 4.3 T/m for a new MPI scanner. The gradient field of the hybrid topology is achieved from constant 2.2 T/m (permanent magnets) and adjustable 2.1 T/m (electromagnets coils). The gradient field contribution of individual components was considered equally to observe the optimum effect on spatial homogeneity. These topologies were modeled to achieve a homogeneous gradient field around the FFP that covers at least scanning objects for artifacts free imaging. Magnetic flux density at the FFP was also simulated and analyzed for these specific topologies. Numerical results of gradient field strength and magnetic flux density for the proposed selection field geometries at the FFP location were highly compatible with the analytical results. The gradient fields of the three topologies were normalized with the targeted value of 4.3T/m and comparisons are shown in Figure 4.14. The gradient field near the FFP is homogeneous from the -20 to 20 mm range along the z-axis. The electromagnetic coil-based selection field has the highest uniform gradient field (97.5%) within 40 mm centrally positioned at the FFP. Hybrid (combined system) selection field topology has 96.8% homogeneity for the same spatial distance. However, the permanent magnet-based system has the least homogenous gradient field (95%) within 40 mm in the ROI. Three different ways of the selection field implementations are thoroughly studied in terms of relative gradient field strength and spatial homogeneity as presented in Table 4.2.

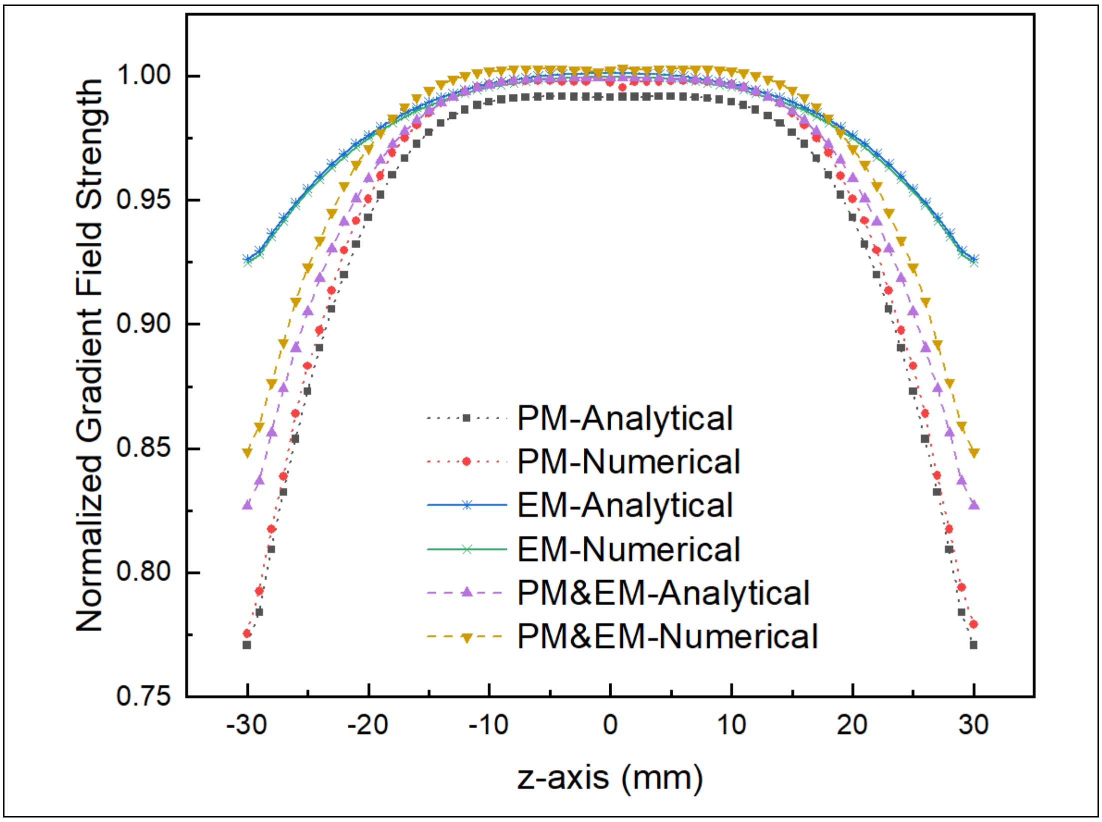

Figure 4.14: Comparison of gradients of the three topologies. PM-Analytical and PM-Numerical lines represent the NdFeB permanent magnets, EM-Analytical and EM-Numerical lines show the electromagnetic coils, and PM&EM Analytical and PM&EM Numerical lines indicate hybrid (combined system) topology.

Analytical, and numerical results of the given geometries were compared. Analytical solutions are the special cases along the z-axis (x = 0, y = 0) in the selection field topologies. However, numerical computations provide us information at any spatial point in 3D (x, y, z). Moreover, analytical results are also used to cross-check the accuracy of the numerical results before utilizing them for further usage in COMSOL. For example, the MPI system has a copper shielding effect that cannot be simulated analytically. Exact virtual implementation of MPI scanner is possible in COMSOL Multiphysics if the performance of the individual component is verified with analytical solutions. Analysis of the selection field topologies was accomplished on a single value of 4.3 T/m. However, the finding of this research could be used to design a selection field of the customized MPI scanner for specific applications.

All geometries were designed with an approximate enhanced ratio of 11.25% to the Maxwell configuration length (the highest spatial homogeneity). Most MPI scanners presented in the literature so far were used for small animal imaging with a bore size of approximately 50 mm. Limited research is found on human brain size MPI devices with a very small gradient field even less than 1 T/m. The bore size of MPI scanners and gradient field strength and their homogeneity are very correlated. Consequently, an enhanced ratio can be increased for a large bore size at the tradeoff of gradient field homogeneity.

Table 4.2: Comparison of all topologies over 40 mm distance symmetric around field-free point (FFP).

Topology	Gradient Field Strength (T/m)		Gradient relative error	Spatial homogeneity
	Analytical	Numerical	(%)	(%)
PM	4.263	4.288	0.58	95
EM	4.305	4.299	0.13	97.5
Hybrid	4.297	4.310	0.30	96.8

The resistance of the copper wire (1.7 mm diameter) used in two series-connected electromagnets of the hybrid topology is 2.4756 Ω. The maximum power dissipation of 1997 W was evaluated in COMSOL at 28.4 A. However, the resistance of the electromagnetic topology is 9.669 Ω which is quite high in comparison to the hybrid topology. So, the maximum power dissipation of 6919 W needs a large water-cooling system to keep the selection field setup at room temperature. Power requirements of the electromagnetic coils (EM) and hybrid topologies were calculated for different values of the gradient field strength as presented in Table 4.3. Electromagnetic and hybrid systems are operated at the maximum current capacity of the copper wires.

The permanent existence of high magnetic flux density at the FFP in PM topology undermines the easiness of this setup. The rapid motion of the patient inside the MPI scanner in the presence of a high magnetic field may generate high dB/dt. However, there is no theoretical or experimental work is done. Similarly, a high current requirement in the electromagnetic coils generates very high-power dissipation which needs a proper cooling setup that is beyond the scope of this thesis. However, the combined topology does not have a permanent existence of very high magnetic flux density at the FFP and does not require high power in comparison to their separate setup.

Table 4.3: Electrical power requirements of the electromagnetic (EM) and hybrid (PM&EM) topologies.

Gradient field (T/m) of Hybrid		Gradient field (T/m) of EM	Power dissipation (W) of EM	Power dissipation (W) of Hybrid
PM	EM			
2.2	0	2.2	1809	0
2.2	0.7	2.9	3146	221
2.2	1.4	3.6	4851	886
2.2	2.1	4.3	6919	1997

The equivalent gradient field is achieved from the combined topology using moderate specifications. The selection field of the hybrid system provides an adjustable FOV size with less power requirement compared to EM topology. So, the combined topology (i.e., PM &EM) is the most suitable to design an MPI scanner.

5. MAGNETIC PARTICLE IMAGING (MPI) SCANNER

MPI is a new tomographic imaging technique that uses SPIONs as a tracer agent. It does not produce any signal from human tissues and bones, which distinguishes it from other imaging modalities such as MRI and CT [1]. It uses the non-linear magnetization response of the tracer agents (defined by the Langevin function). MPI has a linear dependence on the concentration of the biocompatible SPIONs which are used for diagnosis and therapeutic applications. Gleich et al. extended the MPI scanner in 2008 to scan a 2D area of 1 x 1 cm^2 with a Lissajous scanning sequence at 25 frames per second [70]. The hardware of the MPI scanner was modified to a 3D level in 2009 for real-time acquisition (in-vivo). The movement of the bolus through the cardiovascular system of the healthy mouse was recorded with a high temporal resolution of 21 ms for 4D imaging [14].

MPI technique is at the pre-clinical stage currently and many research groups are working on the different aspects of it to explore its limits. Fundamentally MPI technique is based on the field-free point (FFP) selection field in closed bore geometry. However, Goodwill et. al. introduced the field-free line (FFL) selection field in 2012 for MPI [76]. FFL is a significant achievement that promises high sensitivity and less acquisition time as compared to FFP. Furthermore, MPI scanners of versatile methodologies such as single-sided, open bore (combination of two single-sided setups), and traveling wave MPI have been constructed in the last ten years [83,84].

In this thesis, a custom MPI scanner was designed for phantom imaging at 9.3 kHz. FFP based selection field of 4.3 T/m was implemented. Single drive and receive pair of solenoid coils were built to generate excitation field and pick-up the response of MNPs at FFP, respectively. A resonant filter was integrated into the drive chain at 9.3 kHz to achieve lower power dissipation. Standard nanoparticles of Vivotrax and Perimag® were used for phantom scanning. X-space reconstruction algorithm was applied for the reconstruction of the image.

5.1. Magnetic Gradient Fields

Spatially inhomogeneous (static) magnetic fields are implemented with NdFeB permanent magnets and/or electromagnets. Selection field based on FFP generates “no field region" at a single point (usually midpoint of the geometry) and linearly increases on other sides of ROI. The thorough detail of FFP spatial encoding is presented in the previous chapter. In the scope of this thesis, a gradient field of 4.3 T/m is implemented with two pairs of disc-shaped permanent magnets as shown in Figure 5.1. Permanent magnets of 100 mm diameter and thickness of 10 mm were mounted at a distance of 71 mm (internal working space of the setup) with epoxy glass sheets.

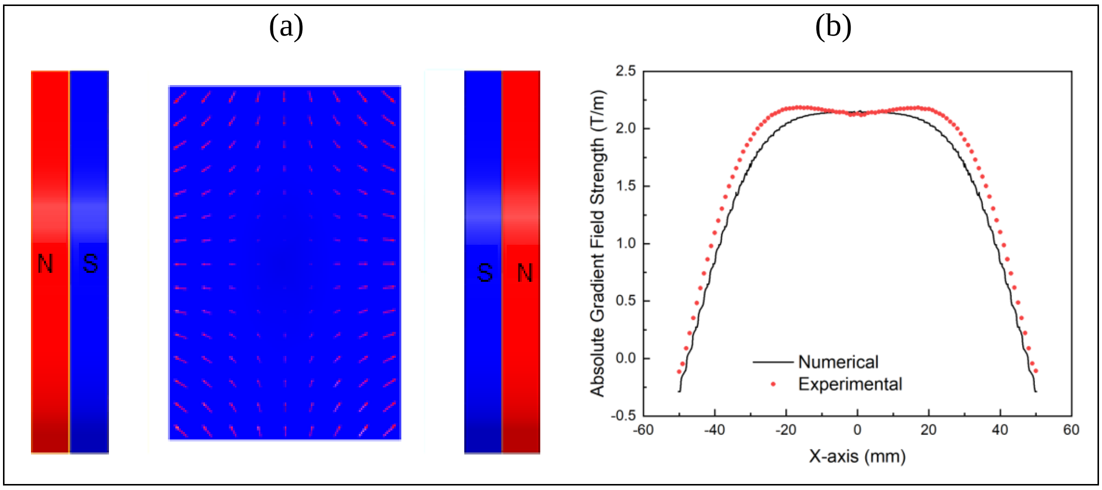

Figure 5.1. Selection field of the MPI scanner, (a) Pictorial representation of the permanent magnets for a selection field. N represents the north pole while S represents the south pole of NdFeB permanent magnets, (b) Gradient field along the bore axis (scanning axis) which is half of the fast axis gradient field strength (4.3 T/m).

The magnetic field inside the internal working space of the scanner was measured with axial (Figure 4.6(a)) and transverse (Figure 4.6(a)) probes, respectively. Overall, the magnetic field profile in the xz plan was calculated from axial and transverse probe data as shown in Figure 4.7. The gradient field along the bore axis is 90% homogenous from -29 mm to +29 mm along the x-axis. Gradient fields are three-dimensional by default, so the in-house MPI scanner has (-2.15, -2.15, 4.3) T/m along (x, y, z), respectively.

5.2. Solenoid Drive and Receive Coils

Dynamic magnetic fields are used to excite superparamagnetic iron oxides (SPIONs) at specific frequencies (e.g., 1-100 kHz) for magnetic particle imaging (MPI) applications [94]. These magnetic fields are implemented with different shaped electromagnetic coils. Similarly, the non-linear response of the magnetic nanoparticles is detected with electromagnetic coils. However, alternating current at frequencies to single copper wire causes high resistance as compared to direct current. This phenomenon is known as the skin effect and becomes the source of high-power losses in drive coils and low SNR ratio. To mitigate these issues litz wires are used for both drive and receive coils. The number of drive and receive coil pairs define the scanning dimensions of the MPI scanners. Usually, solenoid or Helmholtz coils are preferred to generate axial magnetic fields (for the x-axis). Rectangular, saddle, and fingerprint-shaped coils are utilized to generate transverse magnetic fields (for y, z axes).

Drive and receive coils of the MPI scanner along the bore axis were designed in solenoid shape. While homogeneity of the magnetic fields has significant importance in MRI, it is less crucial in MPI. Optimum homogeneity of the solenoid coil is achieved when its length is equal to 1.73 times its radius. The magnetic field of the coil is calculated with the following equation;

$$B(z) = \frac{\mu_0 NI}{2L(R_{out} - R_{in})}\left[A\,ln\frac{R_{out} + \sqrt{R_{out}^2 + A^2}}{R_{in} + \sqrt{R_{in}^2 + A^2}} + B\,ln\frac{R_{out} + \sqrt{R_{out}^2 + B^2}}{R_{in} + \sqrt{R_{in}^2 + B^2}}\right] \tag{5.1}$$

where $A = \frac{L}{2} - z,\ B = \frac{L}{2} + z$, and $-\frac{L}{2} < z < \frac{L}{2}$

L is the length of the solenoid coil. R_{in} and R_{out} are the inner and outer radii of the coil, respectively. *N* is the number of turns on a multi-layer solenoid coil. The deviation of the magnetic fields from the peak value (midpoint value) is known as the homogeneity of the magnetic fields represented with H.

$$H = \frac{B_0 - B_z}{B_0} \tag{5.2}$$

where B_0 is the midpoint magnetic field of the solenoid coil.

Numerical simulations were carried out in COMSOL to achieve optimum homogeneity. The drive and receive coils are designed in a cylindrical shape as shown in Figure 5.2.

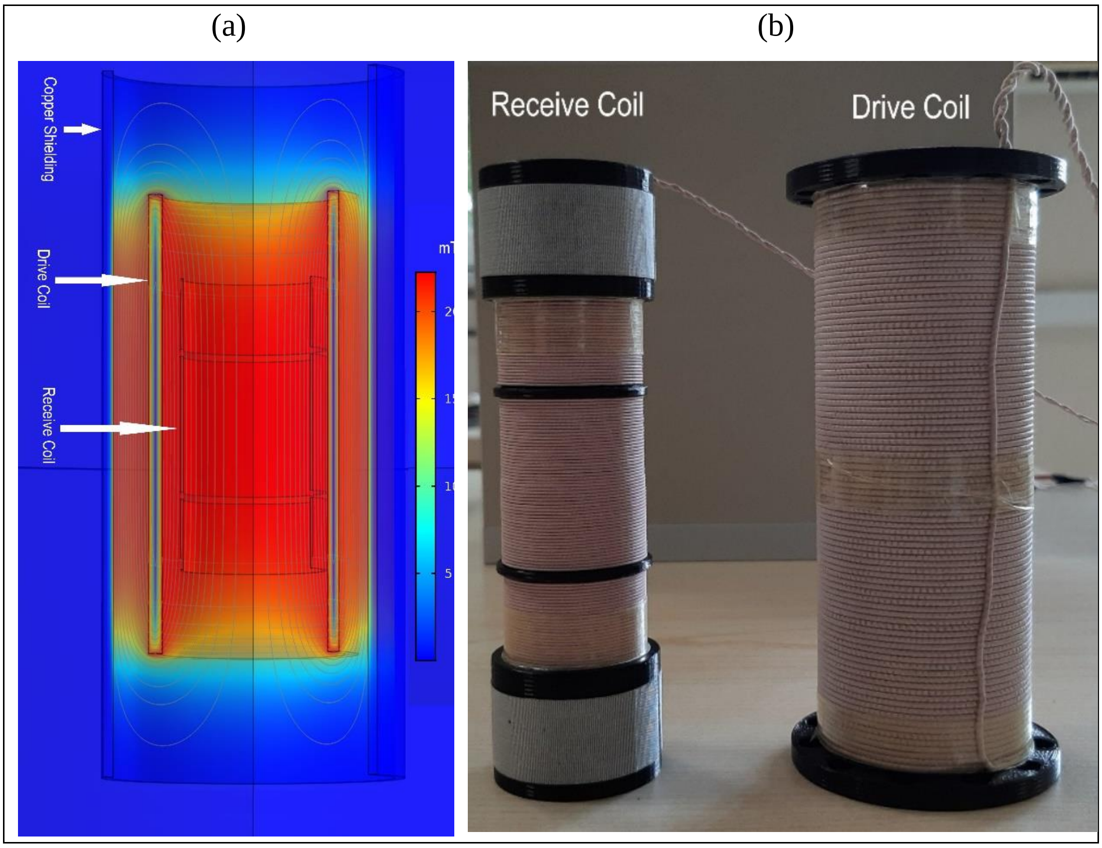

Figure 5.2: (a) Magnetic flux density of the drive coil in COMSOL, (b) Construction of drive and receive coils based on numerical simulation results.

The nonlinear response of the SPIONs is measured through the inductive method using a solenoid receive coil. However, the tracer response is a million times smaller than the fundamental harmonics of the excitation frequency. The induction of the first harmonic on the receive coil is known as the direct feedthrough phenomenon. There are two methods to eliminate the direct feedthrough effect. One is based on the geometric design of the receive coil which consists of three sections; the outer sections winding is opposite the middle section. Another method is to integrate a band stop filter (BSF) to suppress the fundamental harmonics of the receive coil. To show the advantages of the gradiometric winding of the receive coil, COMSOL results are shown in Figure 5.3.

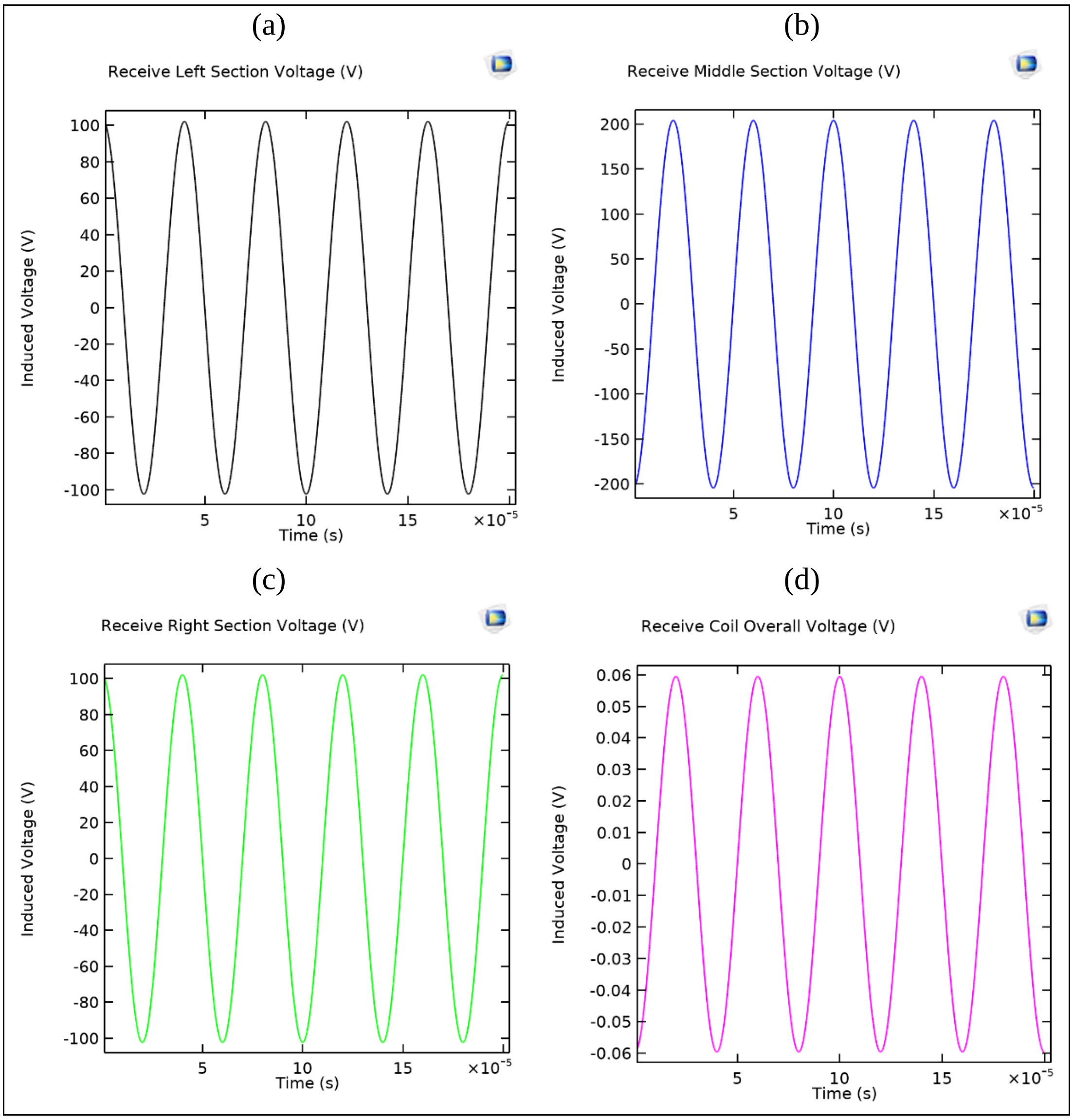

Figure 5.3: Voltage induced on the different sections of receive coil: (a) left section (upper), (b) middle section, (c) right section (lower), (d) overall voltage induction on the receive coil without SPIONs.

The voltage induced by the left and right sections of the receive coil is almost the same as the middle section voltage with opposite polarity. So, the overall voltage represented in Figure 5.3(d) is in the range of mV. When experiments will be taken on the nanoparticles at the FFP, induced voltage on receive coil will reflect particle signal efficiently. Practically, only overall receive coil voltage is recorded for post-processing.

Litz wire of 1.37 mm diameter was utilized for multilayers construction of the drive coil. Three layers drive coil was designed to achieve 20 mT (peak amplitude) magnetic flux density at a minimum current. The internal diameter of the drive coil is

44 mm. Drive coil inductance of 533.35 µH was measured with LCR 8105 G meter. Similarly, a single layer receive coil has an inductance of 66.95 µH. Physical and electrical key parameters of the drive and receive coils at 9.3 kHz are given in Table 5.1.

Table 5.1: Key parameters of the Magnetic Particle Imaging Scanner.

	Drive Coil	Receive Coil
Number of layers	3	1
Number of Turns	276	26:51:26
Length (mm)	130	82.5
Width (mm)	4.11	0.77
Internal diameter (mm)	44	32
Resistance (Ω)	1.956	0.929
Inductance (µH)	533.35	66.95

5.2.1. Sensitivity of the Drive Coil

The supporting holder of the drive coil was made from PLA (polyacrylic acid) material with a 3D printer. Magnetic flux density generated by the drive coil is directly controlled with electric current passing through it. To prevent the drive and receive coils from the nonlinearities of the permanent magnets and environment electromagnetic interferences, a cylindrical copper shielding of 3 mm thickness was used. Moreover, the shielding also restrains high-frequency magnetic fields in a closed area. The drive coil was placed in the cylindric copper shield which also reduced the efficiency of the coil depending on the air gap between the drive coil and copper shielding. To measure the sensitivity of the electromagnetic coil, 1A (DC) current was applied and magnetic flux density was measured across the length of the coil. Minimum current is applied to avoid thermal heating at the coil. Numerical simulation was performed in COMSOL Multiphysics using its AC&DC model, and experimental data were recorded with a gauss meter and moving robot. The comparison of the numerical and experimental data for the drive coil sensitivity is shown in Figure 5.4. The magnetic flux density of 2.55 mT was measured at the center of the drive coil at 1A direct current. The numerical and experimental data are in good agreement in terms of field homogeneity and efficiency (mT/A). Magnetic field homogeneity of 95% was achieved from -32 mm to +32 mm across the midpoint of the drive coil.

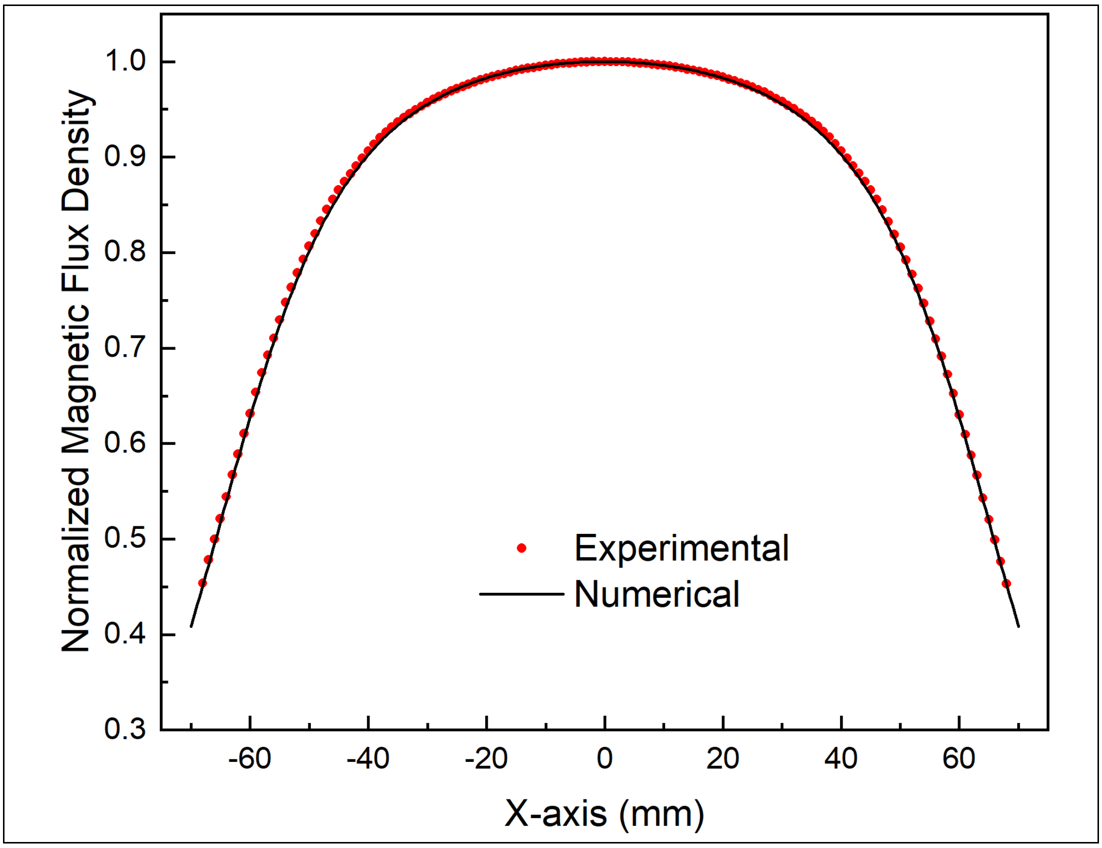

Figure 5.4: Normalized transfer function of the drive coil. The magnetic flux density of the drive coil was measured at a direct current of 1A.

5.2.2. Receive Coil Sensitivity

The supporting holder of the receive coil was built from PLA material with a 3D printer. The length of receive coil is 82.5 mm which is made from 3 sections based gradiometric type. The middle section is almost equal to the outer sections (left and right) of the receive coil. Litz wire diameter of 0.77 mm was used for the receive coil. To measure the sensitivity of the coil, 1A (DC) was applied and measurements were taken with 1 mm resolution along the x-axis. Numerical simulation and experimental data were compared, and their results are presented in Figure 5.5. The magnetic flux density of 1.10 mT was measured at the center of the drive coil at 1A direct current. The numerical and experimental data are in good agreement in terms of field homogeneity and efficiency (mT/A). Magnetic field homogeneity of 90% was achieved from -7 mm to +7 mm across the midpoint of the receive coil (middle section).

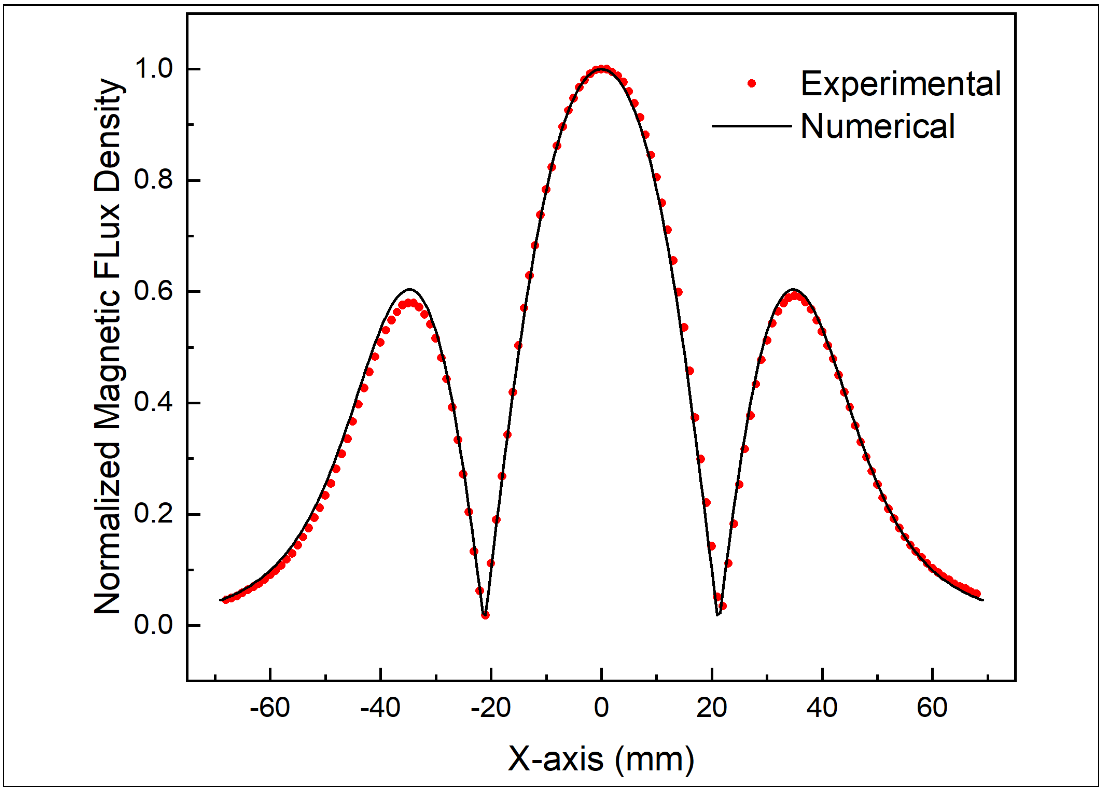

Figure 5.5: Normalized transfer function of the receive coil. The magnetic flux density of the receive coil is measured at a direct current of 1A.

Gradient field homogeneity (selection field), and homogeneous magnetic field (drive coil) are very crucial to correlate the theoretical and experimental boundaries of the FOV. As, both magnetic fields are highly homogenous inside the FOV region, so minimum artifacts would appear in the reconstructed image. In addition to this, receive coil homogeneity is also significant for scanning objects inside the FOV. 90% homogeneity of the middle section (receive coil) is the same as the 15 mm FOV.

5.2.3. Comparison of AC and DC Sensitivity

To prevent the drive and receive coils from the nonlinearities of the permanent magnets and environment electromagnetic interferences, a cylindrical copper shielding of 3 mm thickness was used around the co-axial coils. DC sensitivity does not affect an air gap. However, AC sensitivity is obtained by applying 1A (RMS-root mean square) alternating current, which changes with an air gap. As the air gap increase, AC sensitivity approaches DC sensitivity. Unfortunately, it is not possible to reserve empty space between the drive coil and copper shielding. To figure out optimized shielding distance, a parametric sweep study was performed in COMSOL Multiphysics. Moreover, shielding also restrains high-frequency magnetic fields in a closed area. The comparison of AC and DC sensitivity [85] is presented in Figure 5.6.

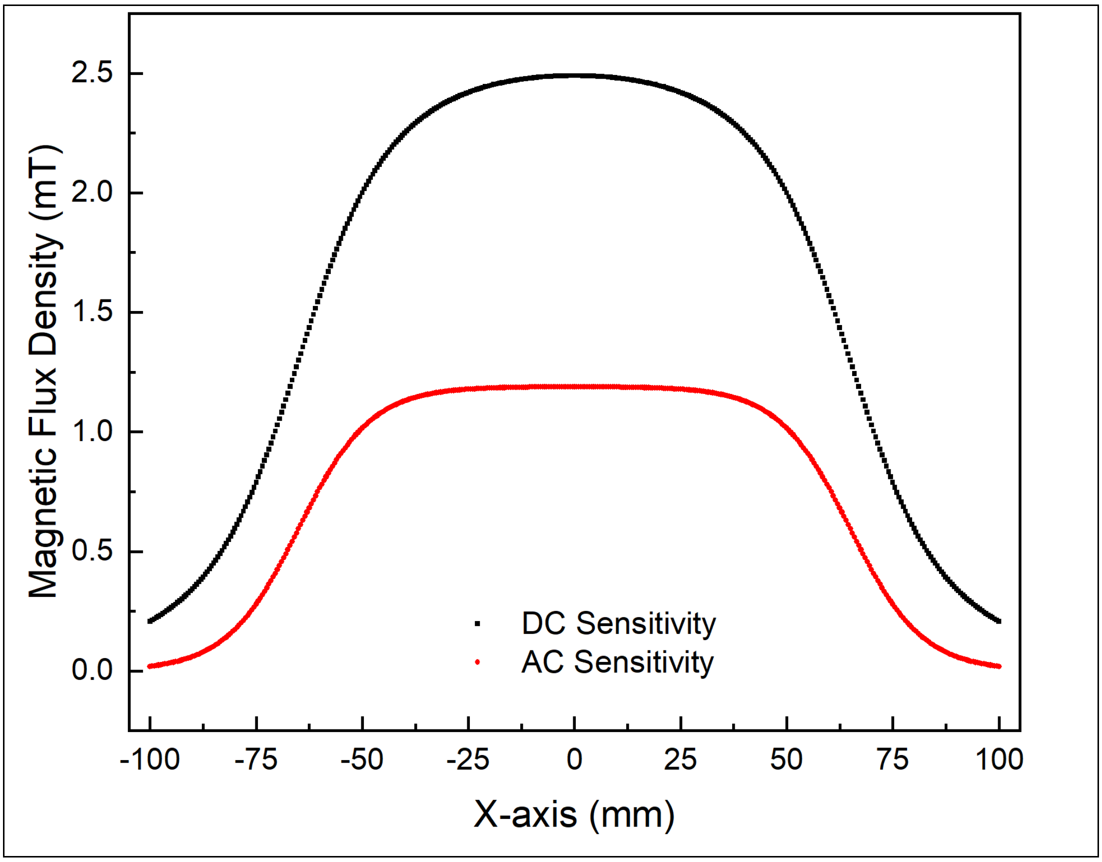

Figure 5.6: Sensitivity of the drive coil with direct current (1 A) and alternating current (1A RMS) at 9.3 kHz is evaluated.

In the light of the parametric sweep study of the COMSOL software, copper shielding was placed between selection field permanent magnets and the drive coil with an air gap of 8.5 mm. Again, DC is constant and does not affect magnetic flux density. Thus, the magnetic flux density of 2.55 mT was measured with 1A direct current. 1A (RMS) sinusoidal current at 9.3 kHz was applied to determine AC sensitivity which is 1.18 mT/A. The drawback of reduced sensitivity of the drive coil is eliminated with the implementation of the selection field with electromagnets instead of permanent magnets. So, there will be no need for copper shielding that causes a reduction in sensitivity values.

5.3. Impedance Matching Circuit

There are two purposes of impedance matching circuits: the first one is maximum power transfer, and the second purpose is maximum signal transfer. Power amplifier and impedance circuit are used to accomplish signal transfer with maximum efficiency. The operating frequency of the system drives the electronic circuit calculations. The inductive reactance of the electromagnetic coil, and the capacitance reactance of the required capacitor are defined with equations (5.3) and (5.4), respectively.

$$X_L = wL = 2\pi f L \tag{5.3}$$

$$X_C = \frac{1}{wC} = 1/2\pi f C \tag{5.4}$$

Here X_L is the inductive reactance, X_C is the capacitance reactance, f is the operating frequency, C is the capacitance, and L is the inductor. As shown in Figure 5.7, impedance Z is defined as the total resistance of the circuit to the alternating current passing through at a specific frequency.

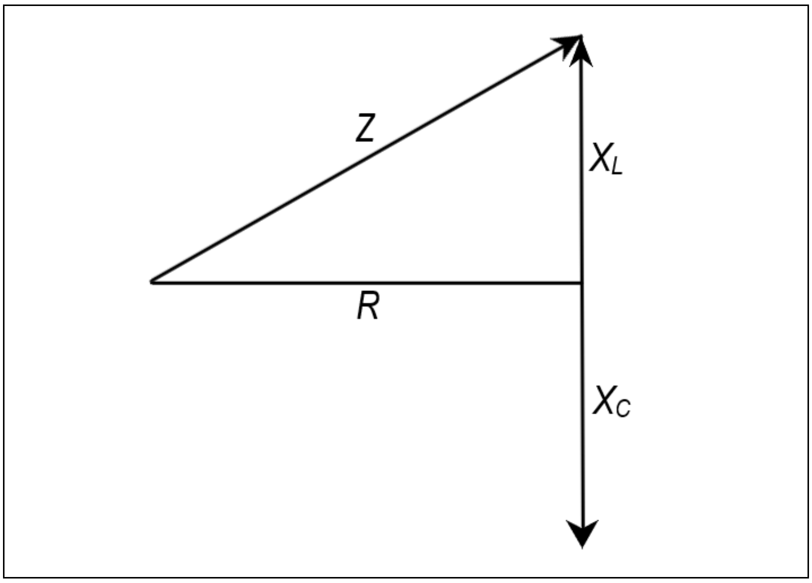

Figure 5.7: Impedance component of an electronic circuit.

The impedance vector as presented in equation (5.6) has a real part (R, resistance) and an imaginary part (X, reactance).

$$X = X_L - X_C \tag{5.5}$$

$$Z = \sqrt{R^2 + X^2} \tag{5.6}$$

At $X_L = X_C$, circuit shows minimum impedance at the resonance frequency. The imaginary part of the impedance vector becomes zero at this condition. So, the resonance frequency can be defined as:

$$f_0 = \frac{1}{2\pi\sqrt{LC}} \tag{5.7}$$

The power amplifier has 5.3 mΩ resistance and the solenoid coil with the resonant capacitor has 2.42 Ω. The high impedance of the load (receive coil) ensures maximum power transfer of the drive chain. Therefore, there is no need for impedance matching between a source (drive coil) and load (receive coil). The only maximum signal (current) transfer was implemented with a series capacitor. Impedance matching circuit (act as a low pass filter) was designed in LTSpice for the drive coil, as shown in Figure 5.8.

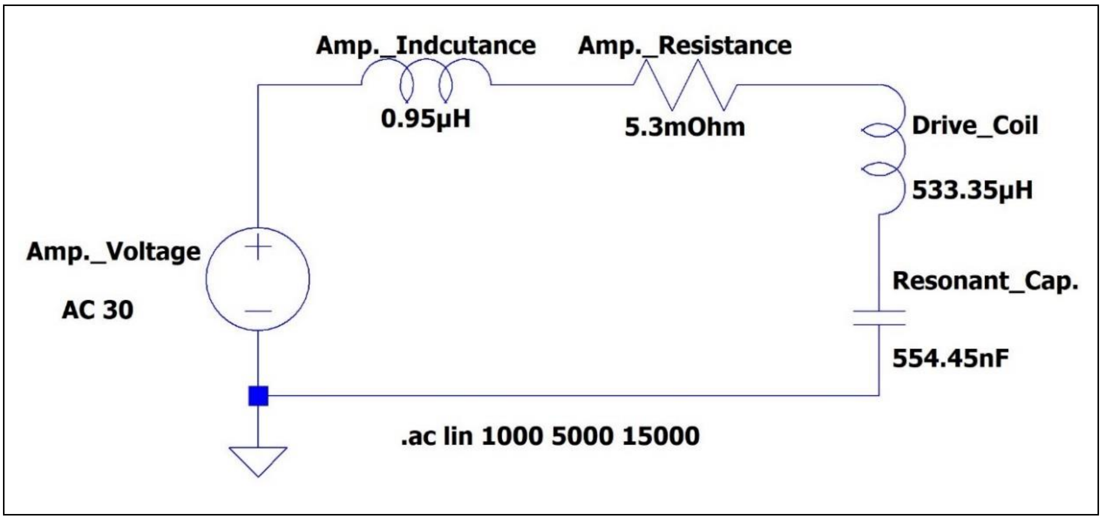

Figure 5.8: Impedance matching and low pass filter circuit for the drive chain of the MPI scanner.

Internal reactance and internal resistance of the power amplifier were also included to simulate realistic behavior. Required capacitance reactance to the drive chain was added with the high current capacitor of 554.45 nF. The resonance and excitation frequency of the drive chain was designed to be 9.3 kHz. The impedance of the load (electromagnetic coil and resonant capacitor) was evaluated at 9.3 kHz, as shown in Figure 5.9(a). The drive signal chain has an impedance of 2.42 Ω at the required excitation frequency. The response of the solenoid drive coil and the resonant capacitor was simulated in LTSpice. The frequency response of the current as shown in Figure 5.9(b) demonstrates the maximum current passing the drive coil that is occurred at 9.3 kHz.

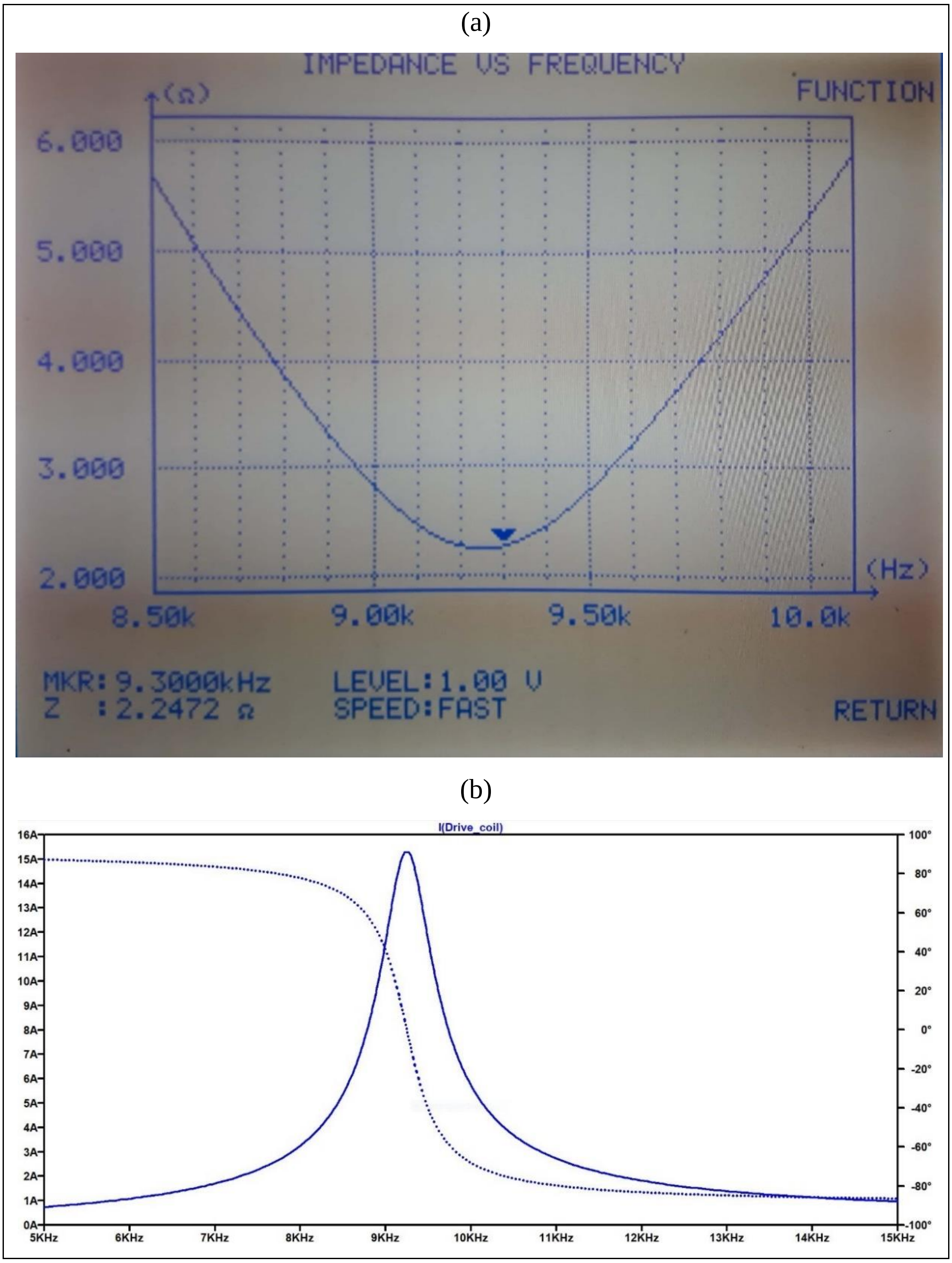

Figure 5.9: Frequency response of the drive chain: (a) Impedance of the drive chain (drive coil and resonance filter) was measured with LCR 8105G meter, (b) Frequency response of drive coil circuit, and the drive coil has the highest current capability at the resonance frequency (simulated with LTSpice).

To suppress higher harmonics of the operating frequency, a low pass or bandpass filter is necessary for magnetic particle imaging (MPI) application. Attenuation rate of

-20dB/decade helps to eliminate unwanted multiple harmonics of the excitation frequency produced from the power amplifier.

5.3.1. Self-Resonance of Drive and Receive Coils

Optimum excitation frequencies of the drive coils for MPI applications are close to 25kHz. As MPI is at the pre-clinical stage, a wide range of excitation frequencies are utilized below 45 kHz. In the design of electromagnetic coils for MPI, the issue of self-resonance should be addressed carefully. Practically, each inductor has a stray capacitance parallel to the inductor. Therefore, the self-resonance of the drive coils for MPI applications is at least 10 times higher than the operating frequency (9.3 kHz) [86]. The frequency response of the drive coil is presented in Figure 5.10. The self-resonance of 278 kHz of the drive coil is measured with an 8105G LCR meter. So, this drive coil can easily operate up to 27 kHz for MPI.

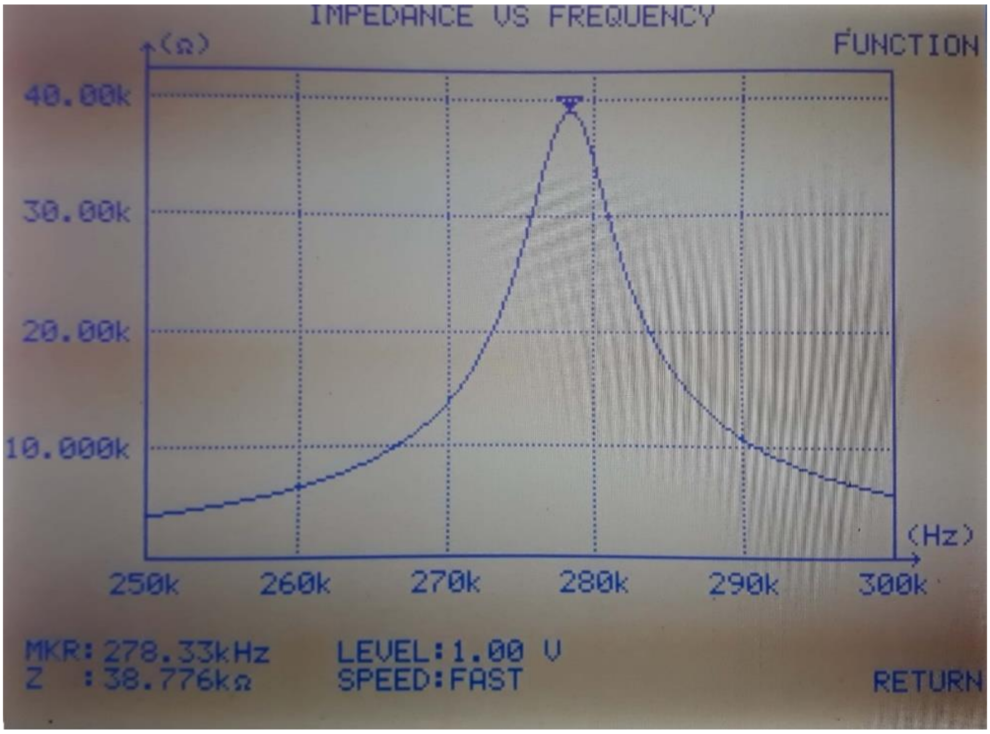

Figure 5.10: Self-resonance of the drive coil.

Self-resonance of the receive coil is highly critical because the receive coil is used to record multiple harmonics of the excitation frequency. Therefore, a wide bandwidth spectrum is essential for the receive coil. The frequency response of the receive coil is shown in Figure 5.11. It is clearly shown that the first resonance peak occurred at 1.22 MHz which ensures multiple harmonics that can be recorded up to 1 MHz.

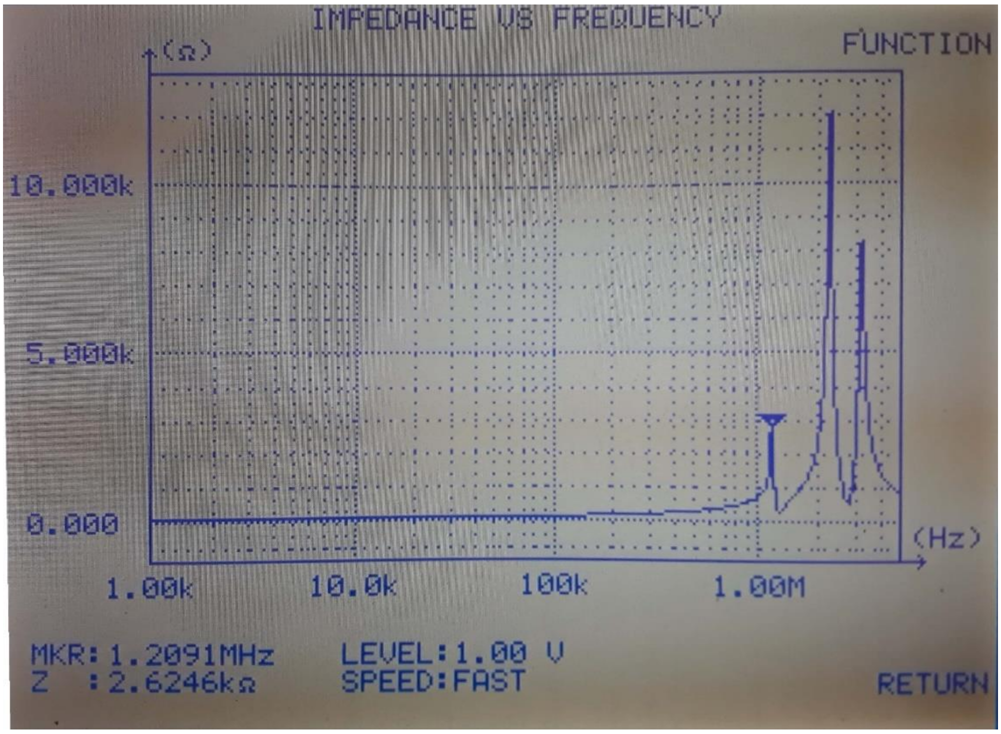

Figure 5.11: Self-resonance of the receive coil.

5.4. Field Free Point Movement

The selection field produces only a single point where magnetic fields are not present. The superposition of spatially homogeneous drive field and inhomogeneous selection field move the FFP non-mechanically. The FFP moves to the position where the magnitude of the drive and selection fields cancel each other.

The drive field also acts as an excitation field for the tracer agents. The sinusoidal shape of the drive field excites magnetic nanoparticles at the excitation frequency. Higher harmonics induced from tracer material provide spatial information inside the field of view (FOV). Sinusoidal excitation field along the bore axis (x-axis) can be represented as;

$$B^D(t) = -A_x^D \cos(2\pi f^E t) e_x \quad (5.8)$$

The superposition of the drive field and selection field can be represented at any spatiotemporal location;

$$B_x(x,t) = -A_x^D \cos(2\pi f^E t) + G_x x \quad (5.9)$$

FFP translates along the x-axis within $[\frac{-A_x^D}{G_x}, \frac{A_x^D}{G_x}]$ interval. The speed of the FFP is maximum at the center of the defined interval and becomes zero at the edges of the interval. This also affects the image quality which is higher at the center of the FOV. The movement of the FFP inside FOV is shown in Figure 5.12. It is observed that FFP moves fast in the middle and slowdown at the outer edges. As the drive field is sinusoidal the response on either side of the FFP is symmetric.

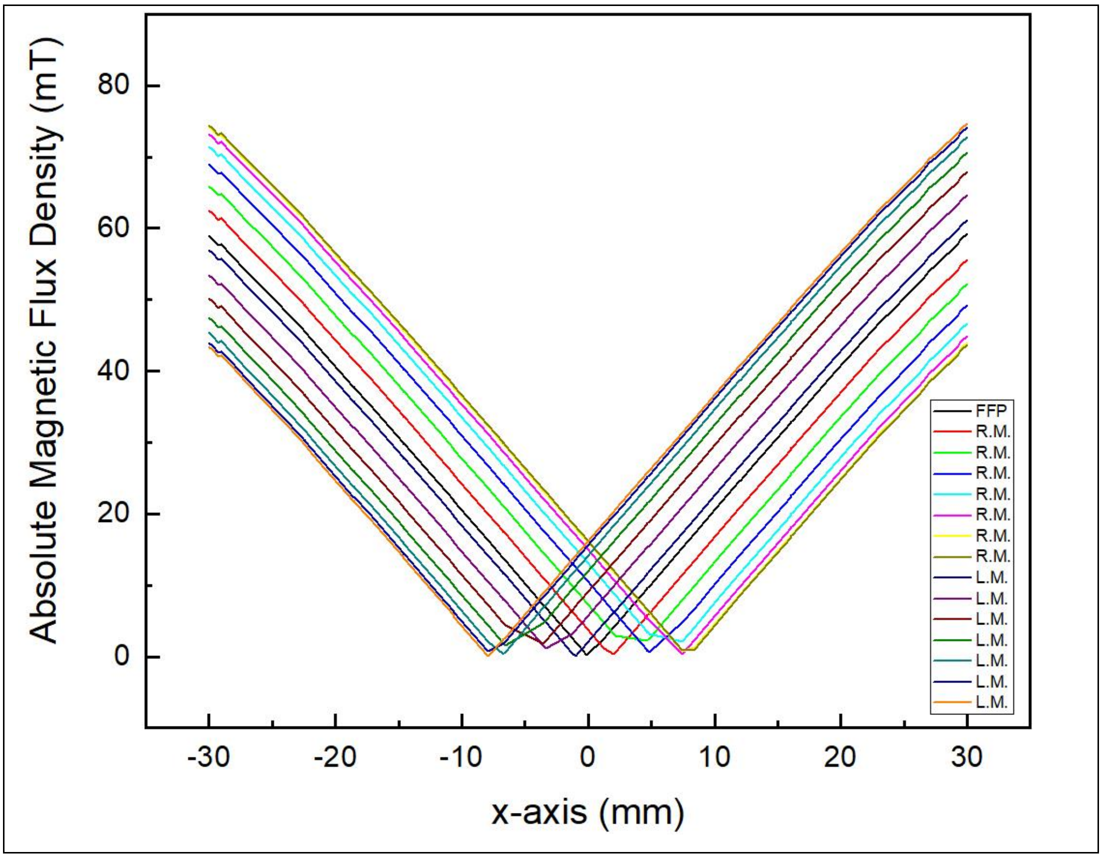

Figure 5.12: Superposition of the drive field half cycle (negative peak to positive peak) and selection field. R.M. represents right moving while L.M. stands for left moving.

An excitation field of 15 mT (peak amplitude) was applied along the bore axis (x-axis), so the FOV region along the x-axis varies from -7 mm to 7 mm. Theoretically, tracer presence near the outer edges does not produce any signal. Maximum signals are induced over receive coil when magnetic materials are placed at the middle of FOV (x = 0). In this study, the selection field of [2.15, 2.15, -4.3] T/m along (x, y, z) axis, respectively with permanent magnets. Similarly, if an excitation field of 15 mT (peak amplitude) is applied along the y and z-axes, then the FOV region would be -7 mm to +7 mm for the y-axis and +3.5 mm to -3.5 mm for the z-axis. The implementation of the drive and receive coils for each axis ensures non-mechanical movement and scanning of the test object within certain limits defines by excitation field and gradient field strengths.

5.5. Signal Chain of MPI Scanner

In this thesis, a single drive coil and receive coil MPI scanner was designed and implemented at 9.3 kHz for phantom imaging. The main components are selection field, copper shielding, drive coil, receive coil, impedance matching circuit for the drive coil, and phantom setup. All components were constructed and integrated mechanically as shown in Figure 5.13(a).

An impedance matching circuit was designed for the drive chain at 9.3 kHz for maximum current at low power dissipation. A customized user-friendly interface based on MATLAB was developed to operate MPI scanners. A calibration process was performed to achieve the required magnetic fields at the source voltage signal of the DAQ card. The excitation frequency, magnetic field strength, number of cycles, number of the repetition rate of the scanning, scanning trajectories, and an applied voltage of the source device (DAQ card).

An applied voltage signal at 9.3 kHz was generated using a DAQ card and power amplifier 7224-AETechron with 100% gain was utilized to amplify the voltage. The voltage was applied to the solenoid drive coil and resonant capacitor to generate an excitation field of 15 mT. Perimag and Vivoplus standard SPIONs were utilized for phantom imaging and their magnetization responses were recorded with gradiometric receive coil. The voltage signal from the receive coil was first amplified with LNA and then process through a 100Hz-300kHz bandpass filter to reject the noise of the unwanted regions.

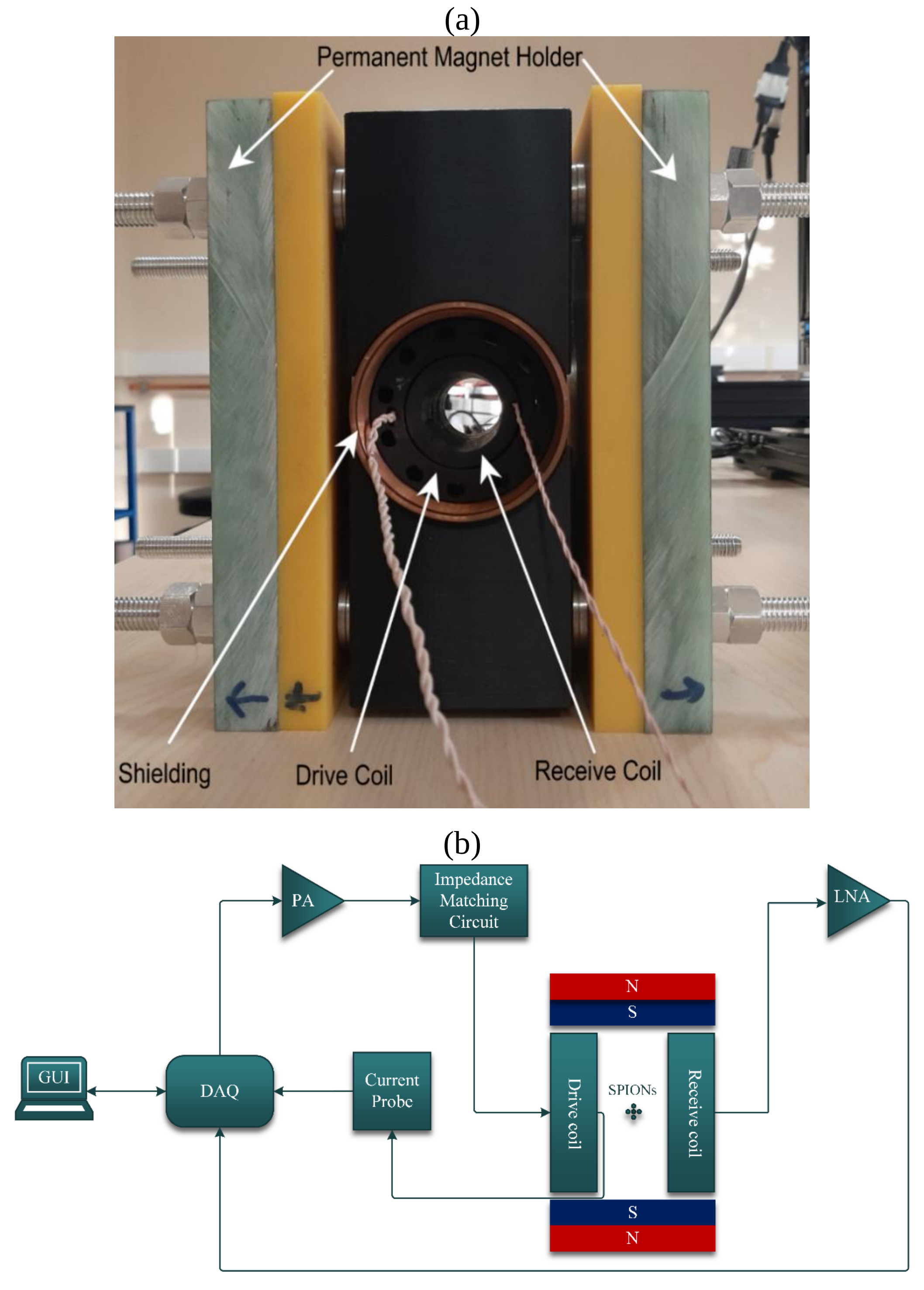

Figure 5.13: Signal chain of the MPI; (a) In-house MPI scanner, (b) MPI device is controlled from MATLAB based control console (graphical user interface, GUI) for imaging. The sinusoidal signal is generated from the data acquisition card (DAQ) and amplified with a power amplifier (PA). Superparamagnetic iron oxide nanoparticles (SPIONs) are placed inside the field of view region of the MPI scanner. Tracer-induced signal is passed through low noise amplification (LNA) of the receive signal before data recording by DAQ device for post-processing.

5.6. Phantom Imaging

Initially, an MPI scanner was targeted to scan standard nanoparticles such as Perimag and Vivoplus. This system has 15 mm FOV along the bore axis (x-axis), so SPIONs placed inside FOV can be spatially localized. 40 µL samples were placed in glass tubes of 3 mm diameter and those glass tubes were fixed in a PLA holder. Our home-designed MATLAB user interface was used to operate MPI scanner at 9.3 kHz, 15 mT (peak amplitude) excitation field, and 100 cycles with 30 repetitions. Background signals (without sample) were recorded at each position with a step distance of 1 mm. Overall, 105 background signals were recorded (21 on each line). A closed view of the sample points on 5 different lines inside FOV is shown in Figure 5.14.

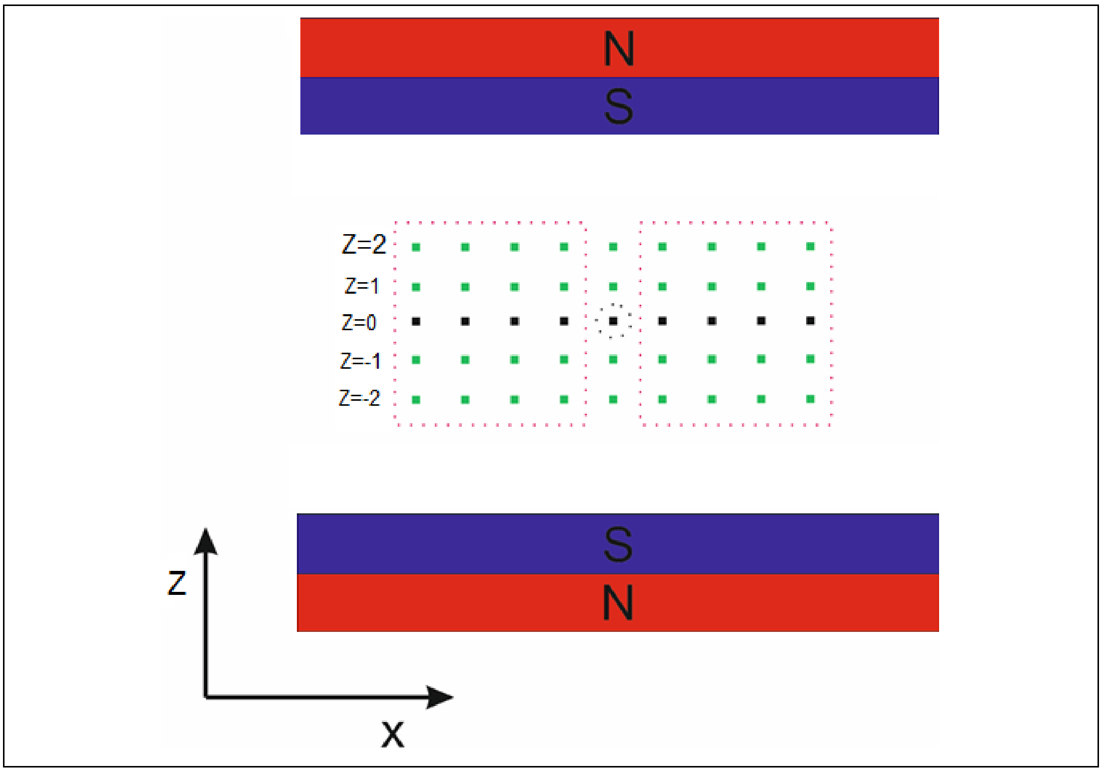

Figure 5.14: Cartesian trajectory scanning with 3D actuator movement of 1mm along the bore axis (x-axis). 5 different lines were scanned along the z-axis with a distance of 1mm.

The same trajectory was followed again to record sample scanning (phantom scanning) after inserting the samples inside the allocated spaces as shown in Figure 5.15. The phantom holder has a length of 60 mm, a width of 10 mm, and a height of

10 mm. However, the holes are 8 mm in depth. These circular holes have a diameter of 4 mm for glass tubes that contains the samples. A single position phantom was translated (scanned) from -10 mm to 10 mm across the FFP position. The overlap of two consecutive data points was 92.85%.

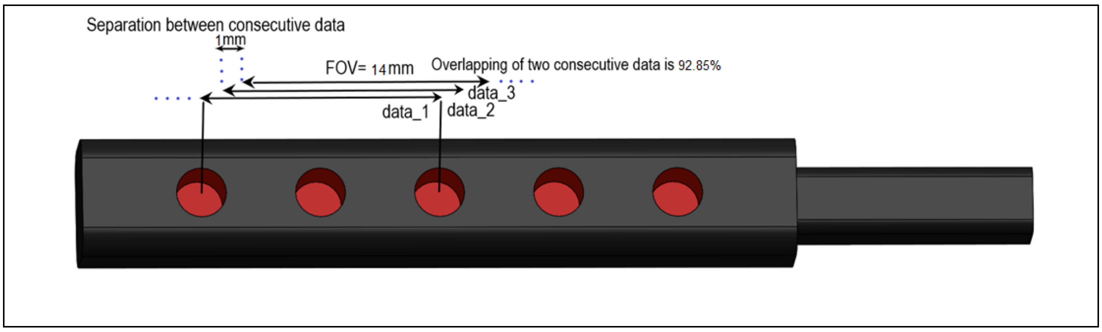

Figure 5.15: Sample holder for phantom imaging.

5.7. Post Processing of Recorded Data

Direct induction of the fundament harmonics to the receive coil dominates over SPIONs' signal. Therefore, digital filtering was inevitable in the time and frequency domain. The finest form of the recorded signal does not provide any information about the spatial distribution of the samples. Imaging reconstruction for MPI is mainly performed with system function (frequency domain) [27] and X-space (time-domain) [28] reconstruction techniques. Under the scope of this thesis, the X-space reconstruction technique was followed to figure out the spatial distribution of the scanned objects. A thorough discussion will be carried out in the next chapter about post-processing and the X-space technique.

6. IMAGE RECONSTRUCTION

Direct visualization of MPI signal is not feasible without transforming the voltage signal to particles concentration. Image reconstruction time and image quality are trademarks of the post-processing techniques. A linear relationship between particle concentration and measured signal is the main assumption in the reconstruction techniques used for MPI systems. Theoretically, MPI scanners do not have background signals inherently. Human tissues, bones, and other structures do not cause any signal generation. Practically signals are recorded without placing scanning objects (phantom, in-vitro sample, in-vivo) are known as background signals due to inductive coupling between drive and receive coils.

Two different techniques are used for MPI image reconstruction purposes. The system function (frequency-based) approach relies on the frequency spectrum of the receiver channels. The system function aims to establish the link between induced signals from SPIONs as a function of space (location dependent) [77]. The system function is calculated basically in two different ways: measurement-based, and model-based.

Measured-based system function takes too much time even days to establish a system matrix. On the other hand, the model-based function relies on the ideal Langevin model. However, the real behavior of the nanoparticles does not fully follow the Langevin model due to the relaxation phenomena of the nanoparticles.

The second technique for image reconstruction of MPI is known as X-space (time-based). Instead of using frequency response, receive channels data is directly processed in the time domain. X-space technique relies on the linear and shift-invariant (LSI) property of the recorded data [87]. This approach works fine for rectangular trajectories, however, the Lissajous trajectory for three drive-receive channels is very challenging as fast scanning intervals violate the LSI property due to the relaxation behavior of the nanoparticles. A brief comparison of harmonic-space and X-space MPI imaging workflow is shown in Figure 6.1. MPI scanner with one drive-receive coil pair is considered enclosed in copper shielding. The selection field for FFP spatial encoding is represented with two pairs of NdFeB permanent magnets (N (north pole), S (south pole)). Although scanning procedures are different for both techniques, its scanner geometry is still identical.

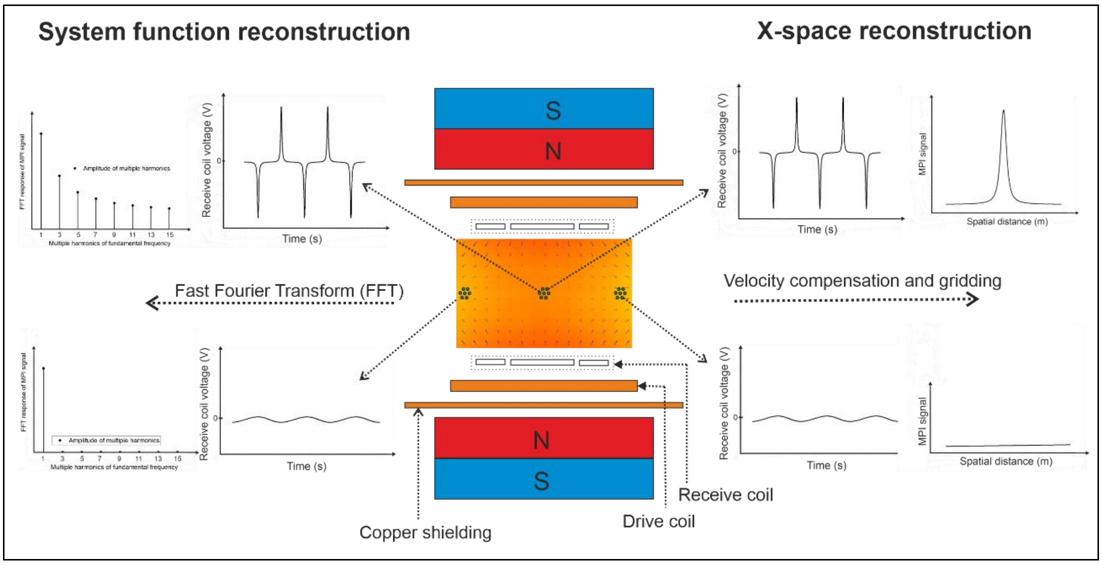

Figure 6.1: System function and X-space are two prominent image reconstruction techniques in MPI. A simplified MPI scanner with one drive coil and one receive coil are displayed in the middle. N, S represents the north and south poles of the permanent magnets, respectively. Maximum particles’ signal is obtained at zero field region (midpoint). System matrix utilizes the Fast Fourier Transform (FFT) of the particles’ signal at each point in the field of view (FOV). However, X-space used the same particle’s signal for further processing. The tracer response becomes saturated at the outer edges of the FOV region which results in no MPI images.

Under the scope of the thesis, an MPI scanner at 9.3 kHz for phantom imaging was constructed. Post-processing and X-space image reconstruction technique algorithms were designed as a last stage of the MPI system. In addition to analog filtering through LNA, digital filters were applied to the recorded data. X-space reconstruction has two key steps, initially, velocity compensation of the FFP was applied followed by gridding the particles’ signal to the specific location.

6.1. System Function Reconstruction

The system function can be measured from calibration-based, model-based, and hybrid approaches, separately. The delta sample of the tracer agent is used and translated with a 3D actuator in a calibration-based system matrix approach [1]. It does not require any mathematical representation of the MPI hardware components or response of the tracer agent. MPI signal (u) relation with system matric (S) is defined as;

$$Sc = u \tag{6.1}$$

where c is particle concentration in the FOV.

All system imperfections are considered in this approach, but it is very time-consuming. Overall MPI system is also simulated in a model-based approach with nearly accurate sensitivity and transfer function of the receive channels [88, 89]. The exact modeling of the nanoparticle response to excitation fields is a key factor in the model-based approach as well. Meanwhile, the hybrid approach integrates both simulation and calibration aspects of the MPI scanner. 3D actuator movement is removed and the focus field for emulation of the selection field is included for robust and accurate system matrix [90-92]. Overall, the acquisition of the system matrix is tedious as compared to X-space reconstruction.

6.2. Post-processing of the Recorded Data

Drive and receive coils of the MPI system are inductively coupled. The fundamental component of an excitation frequency is also induced on the receive coil without the presence of the SPIONs. The particles were excited with an oscillating magnetic field at 9.3 kHz. Tracer particles induce multiple harmonics of the excitation frequency f^{E} on receive coil. Geometric-based cancelation techniques are quite easy to implement, however, it is very challenging to remove the direct feedthrough completely. Particles' signal $u^{\mathrm{P}}(\mathrm{t})$ and coupling component $u^{\mathrm{E}}(\mathrm{t})$ are simultaneously induced on the receive coil as mentioned in equation (6.2);

$$u(\mathrm{t}) = u^{P}(\mathrm{t}) + u^{E}(\mathrm{t}) \tag{6.2}$$

Particle signal and excitation signal are graphically elaborated in the time and frequency domain [100] as shown in Figure 6.2. A background signal without a sample is represented as;

$$u^{empty}(t) = u^{E}(t) \tag{6.3}$$

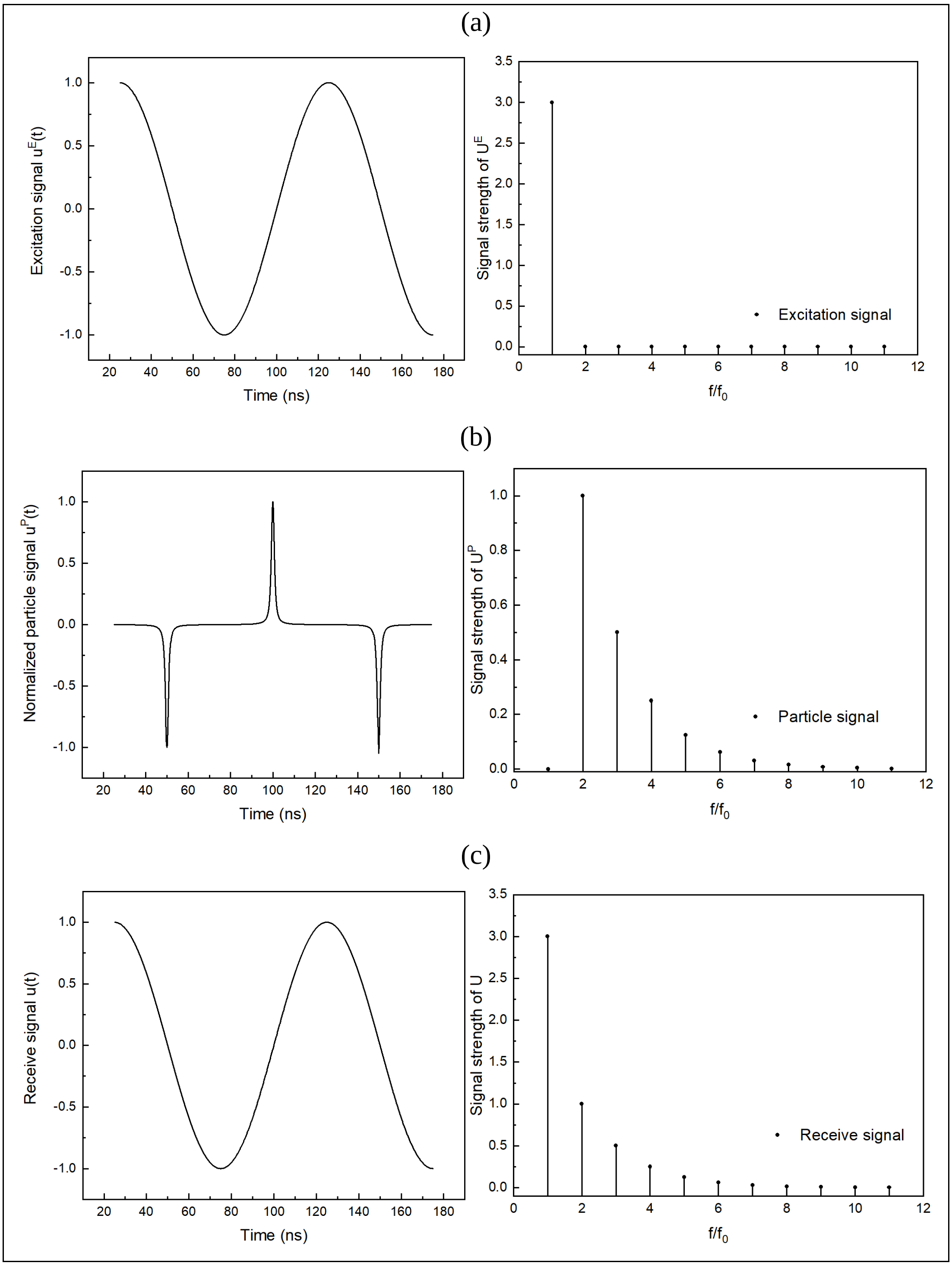

Figure 6.2: The coupling of the excitation frequency to the particle signal; (a) Direct feedthrough induction in the receive coil with sinusoidal excitation field (i.e., the background signal and its frequency spectrum), (b) The induced signal is due to tracer material, (c) the superposition of the excitation frequency component (1st harmonic) and particle signal.

In the time domain, coupled excitation has dominated the overall induced signal on the receive coil. In the frequency domain, the particle signal is distinguishable with multiple decaying harmonics. The background signal (without sample) and its frequency spectrum [100] are shown in the first row of Figure 6.2(a). Furthermore, in the presence of the magnetic nanoparticles receive coil signal still resembles the background signal due to the higher strength of the main frequency direct feedthrough interference [100] as displayed in the 3rd row of Figure 6.2(c).

The particle signal can be extracted from the overall signal by simply removing the empty signal (i.e., background signal) as presented in equation (6.4);

$$u^{P}(t) = u(t) - u^{empty}(t) \tag{6.4}$$

Experimentally, post-processing of the recorded data was initiated with the implementation of equation (6.4) which results in particle signal as shown in Figure 6.3.

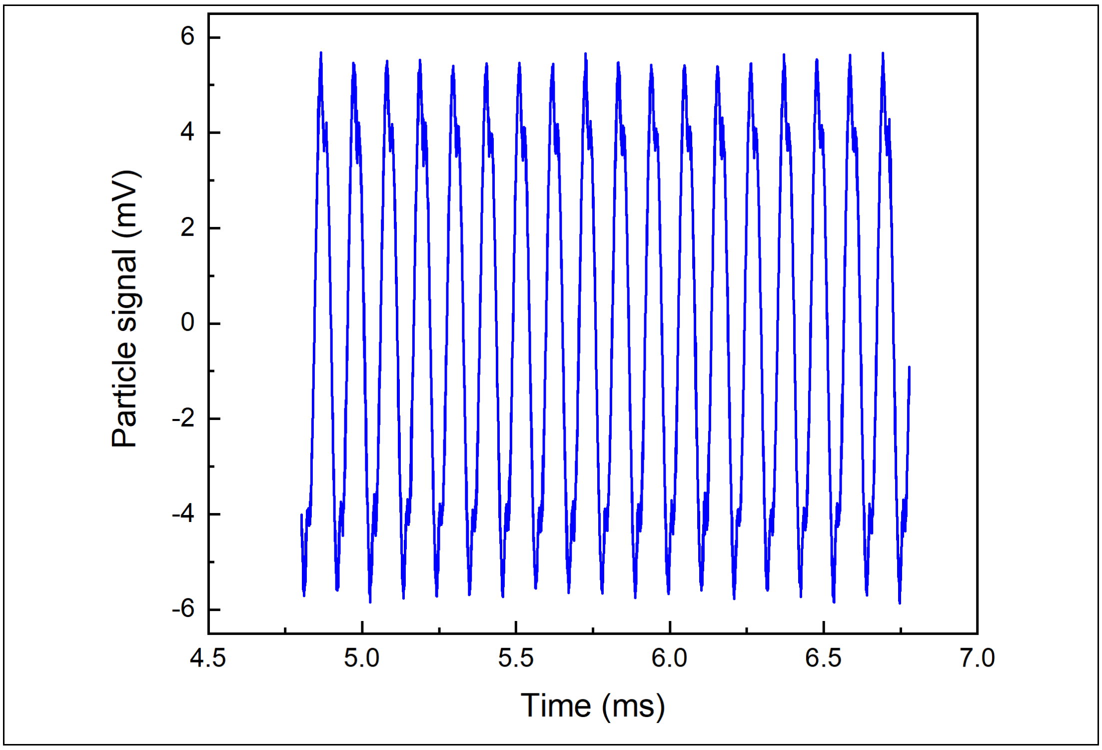

Figure 6.3: Particle signal of the 40 µl Perimag® at the midpoint of the 4.3 T/m MPI scanner. An excition field of 15 mT was applied to acquire the background signal before the sample scanning.

The shape of the particle signal is sinusoidal which shows the dominance of 1st harmonics of the excitation frequency. The subtraction of the background signal did not fully remove the coupled component. In addition, a digital low pass of 16th order was applied in the time domain with cutoff frequency up to 20th harmonics of the excitation frequency. Later on, the particle signal was transformed to the frequency domain and 1st harmonic was eliminated. In the final step of the post-processing, the particle signal was regenerated as shown in Figure 6.4.

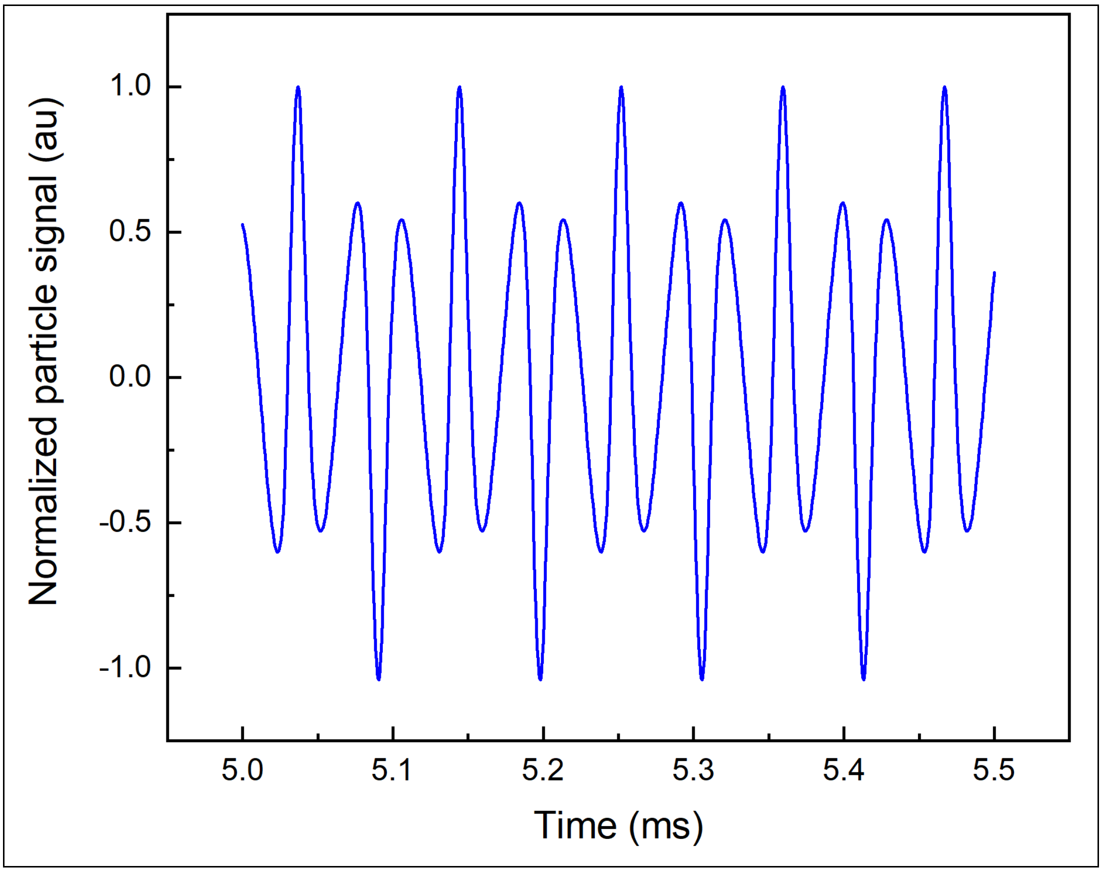

Figure 6.4: Particle signal of the Perimag sample of 40 µl at the midpoint (x=0, y=0, z=0) after digital filtering of the recorded data.

Digital filtering was applied to the particle signals after removing background at each point inside the ROI for further processing through the X-space image reconstruction technique discussed below. The particle signal shows maximum strength at the midpoint of the setup; however, it disappears at the outer edges of the FOV.

6.3. X-space Reconstruction

The time-domain X-space technique offers fast image reconstruction of the particle concentrations [20]. It is important to emphasize that applied field homogeneity and infinite fast relaxation of the tracers are driving assumptions of the X-space technique. Receive coil voltage is normalized with FFP movement followed by the gridding of the MPI signal on the FFP scanning pattern. The first one is velocity compensation of the FFP and the last one is gridding adapted from the reference [87] as shown in Figure 6.5.

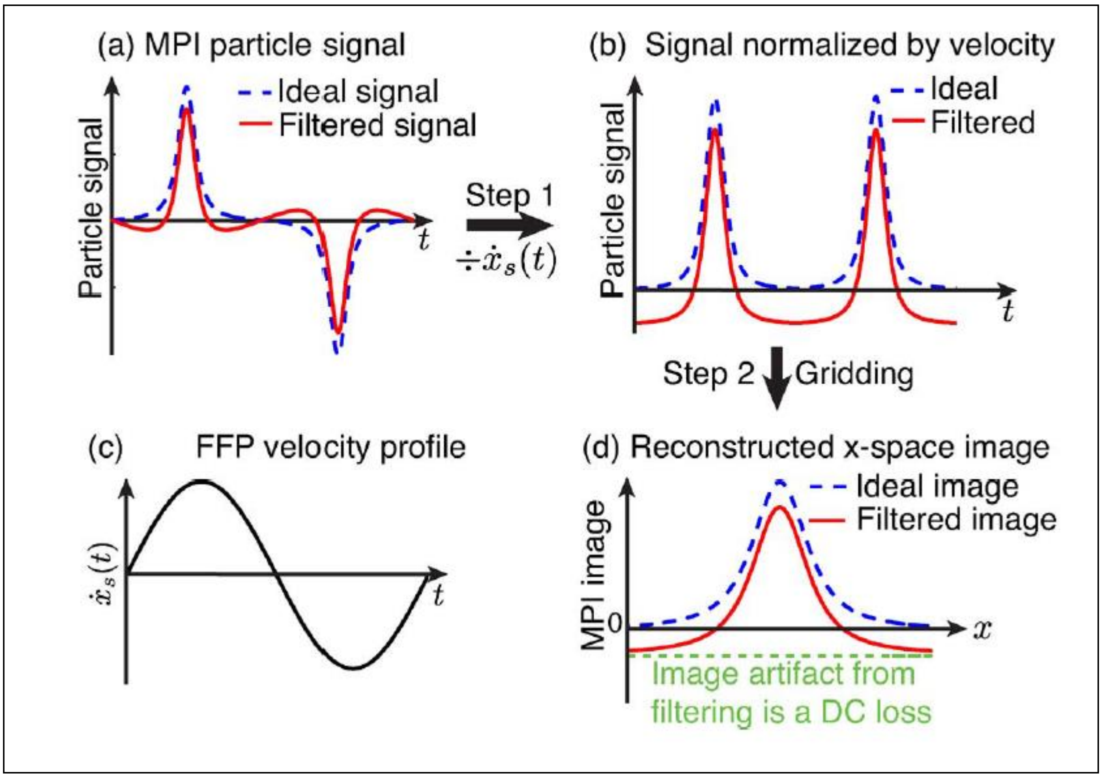

Figure 6.5: X-space reconstruction technique for the post-processing of the MPI signals.

Gradiometric design of receive coils and analog filters on the receive channels remove the feedthrough effect and tracer response at the excitation frequency. Fortunately, the missing information only brings DC offset in the reconstructed signal that can be recovered with continuity boundary conditions [87, 93]. Frequency-dependent relaxation behavior of the magnetic nanoparticle delayed the receive coil voltage in comparison to the excitation field. Relaxation-based delay leads to shifting of the MPI signal in spatial mapping at the gridding stage [56]. Furthermore, the relaxation behavior of the nanoparticles can be modeled as an exponentially decaying function convolved with the magnetic nanoparticles’ magnetization response [56]. A blurring in the reconstructed image can be cleaned with deconvolution techniques such as using Wiener filtering. The movement of the FFP can be mathematically expressed as based on equation (5.9);

$$x^{FFP}(t) = \frac{A_x^D}{G_x}\cos(2\pi f^E t) \tag{6.5}$$

FFP translates along the x-axis over the line within $[\frac{-A_x^D}{G_x}, \frac{A_x^D}{G_x}]$ interval. G_x is gradient field strength along the x-axis, and A_x is the peak amplitude in the x-axis. The maximum limits of the FFP represent the FOV region along the x-axis. Particle signals across the FFP are shown in Figure 6.6.

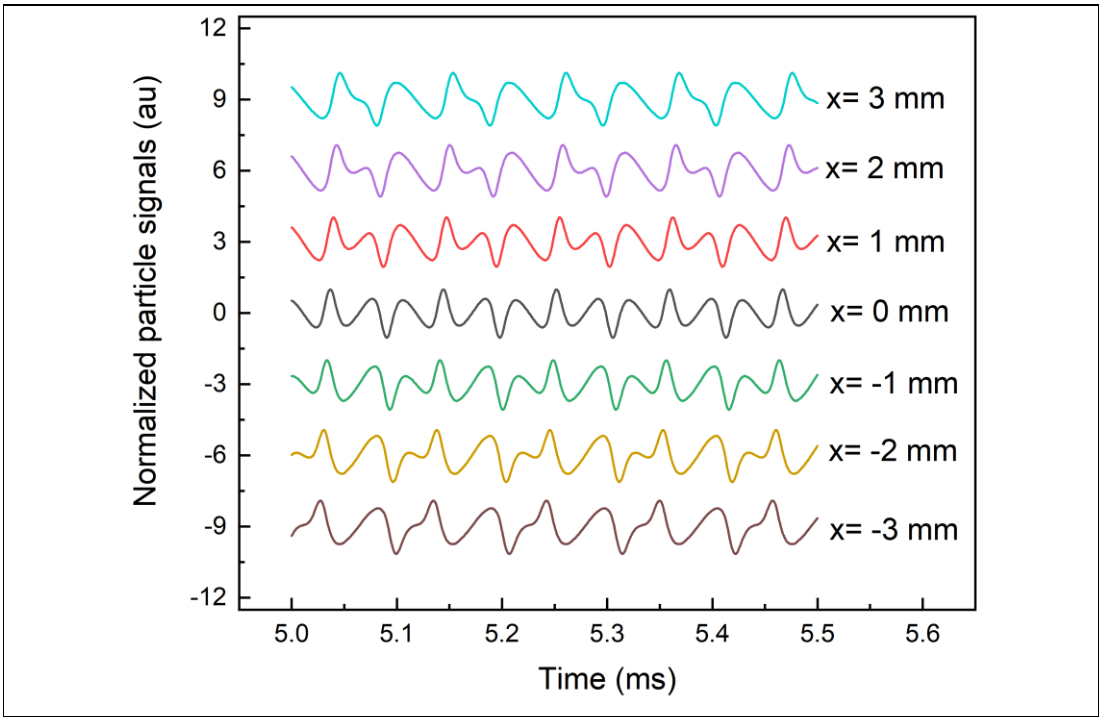

Figure 6.6: Particle signals of the Perimag sample at z=0 line. The midpoint of the setup lies at x=0 mm. The particle signals are symmetric across the midpoint.

The velocity compensation of the received signal can be modeled as in equation (6.6);

$$u^N(t) := \frac{u^P(t)}{(B^D)'(t)} = (c * \acute{m})(\frac{B^D(t)}{G_x}) \tag{6.6}$$

whereas $\acute{m} := P^R m' G_x$

FFP has the maximum speed at the center of the FOV internal (midpoint of the scanning line), whereas the FFP has zero speed at the boundaries. Hence, there is no particle signal at the boundaries. However, if there is an imperfection in the selection field then one can expect a signal even out of the FOV region. Experimentally, velocity compensation was applied to the particle signals at a defined location of the scanning trajectory as shown in Figure 6.7. The partial PSFs at various locations across the x-axis are presented across x=0 mm.

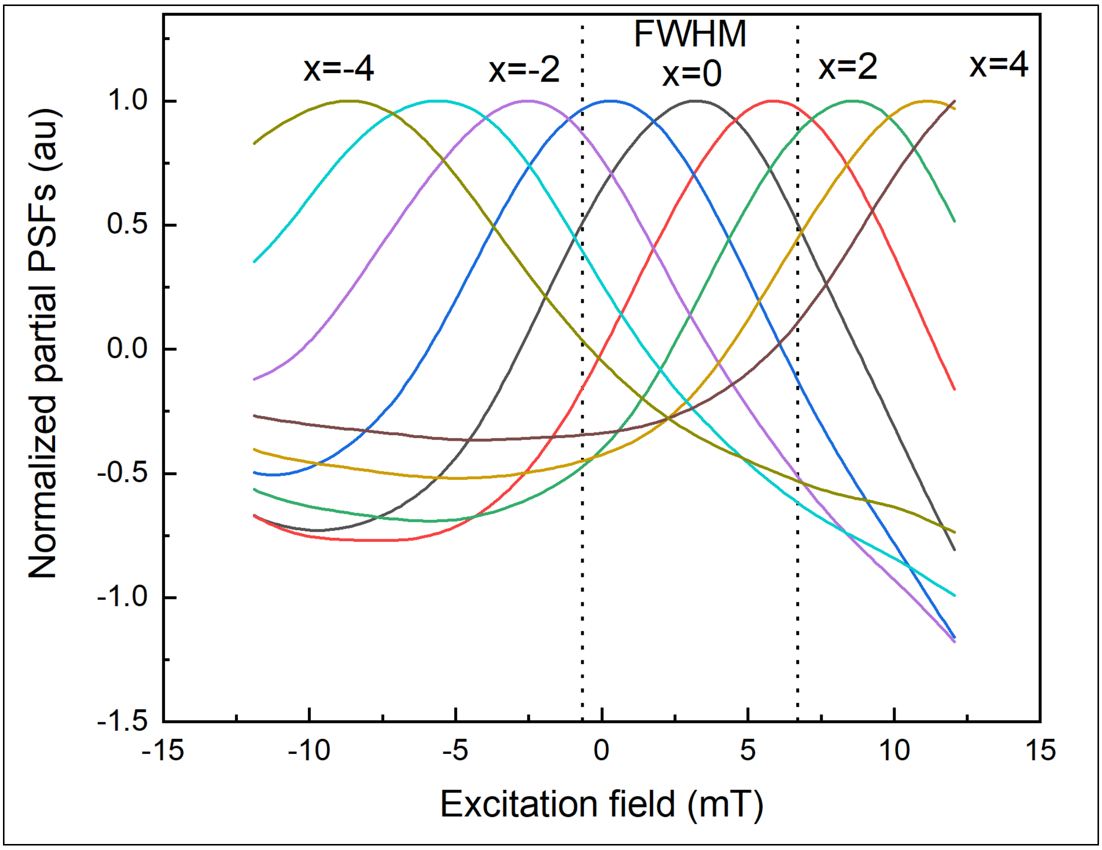

Figure 6.7: Velocity compensated partial PSFs at z = 0 scanning line.

The partial PSFs at positive locations (x= 1, 2, 3, 4) mm were shifted towards the right direction. Whereas the PSFs at negative locations (x = -1, -2, -3, -4) mm were shifted towards the left direction as the FFP moves to the left direction, respectively. The FWHM of the central particle signal was measured to be 7.35 mT which is in good agreement with the results of MPS at 9.9 kHz of the Perimag sample.

The spatial gridding of the particle signals can be performed with the coordinate transformation of the velocity compensated signals. The particle concentration across the FFP trajectory (instantaneous positions) can be expressed as;

$$u^x(x^{FFP}) = u^N(\frac{1}{2\pi f^E} cos^{-1}\left(\frac{G_x}{A_x^D} x^{FFP}\right) = (c * \acute{m})x^{FFP} \tag{6.7}$$

Initially, partial MPI signals were acquired from the velocity compensated signals at scanned positions. Only, the excitation field was transformed to spatial distance (mm) based on the 2.15 T/m gradient along the x-axis as shown in Figure 6.8.

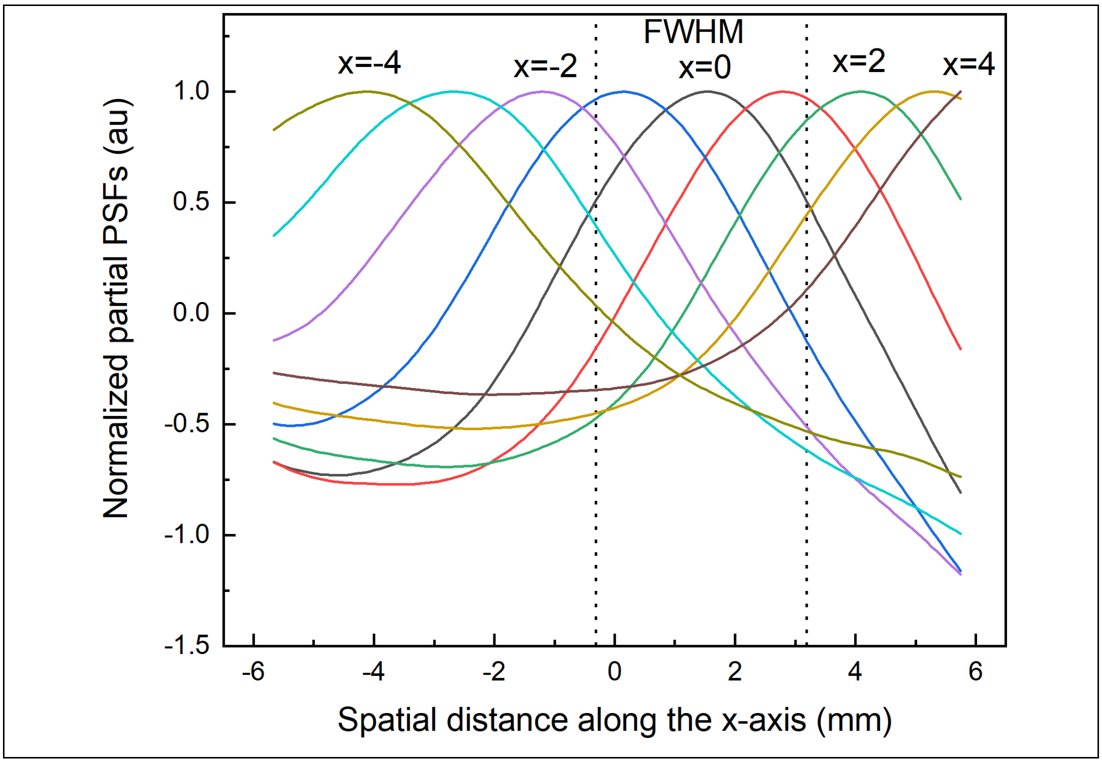

Figure 6.8: Normalized partial PSFs at spatial locations across the x-axis.

The partial PSFs at spatial locations have shown a similar response to the velocity compensated signals. The FWHM of the centered partial PSF was measured as 3.5 mm. This represents the minimum possible resolution for Perimag with an excitation field of 15 mT (peak amplitude) at a 4.3 T/m gradient of the selection field. The FOV region of this MPI scanner is between -7 mm to +7mm along the x-axis. So, the particle signals were acquired from -10 mm to +10 mm with a step distance of 1 mm. To achieve the overall PSF, partial PSFs should be combined in a single frame as shown in Figure 6.9. The FOV is 14 mm and particle signals were recorded with a 1mm gap among them. Therefore, consecutive particle signals have 92.85% overlapping which is visible in Figure 6.9.

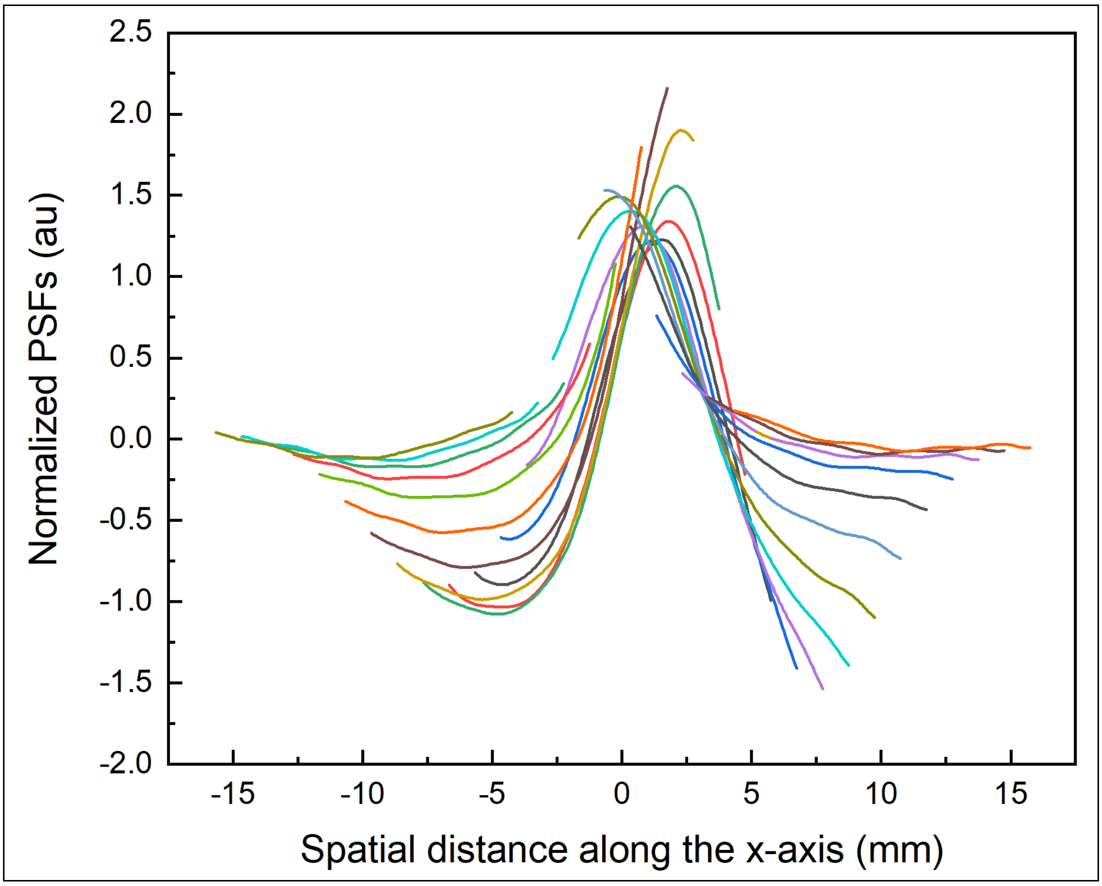

Figure 6.9: Overlapped view of the partial PSFs at z = 0 line.

In addition to overlapping issues, the partial PSFs have variable DC offset among them. The DC offset is based on the elimination of the 1st harmonic at the post-processing stage. This DC offset issue pushes the overall reconstruction of the non-linear and time-invariant (LSI) phase which takes as a challenge for MPI. All other medical imaging techniques such as MRI, CT, ultrasound, and PET/SPECT [87] are quantitative. LSI properties ensure the quantitive capabilities of any medical device. So, it is inevitable for MPI as well. The recovery of the lost component (1st harmonic) helps to restore LSI property for MPI. Under the scope of this thesis, the continuity algorithm was designed for the consecutive partial PSFs so to get rid of the DC offset issue. Overall, MPI signal for each line was possible after the implementation of the continuity algorithm as presented in Figure 6.10.

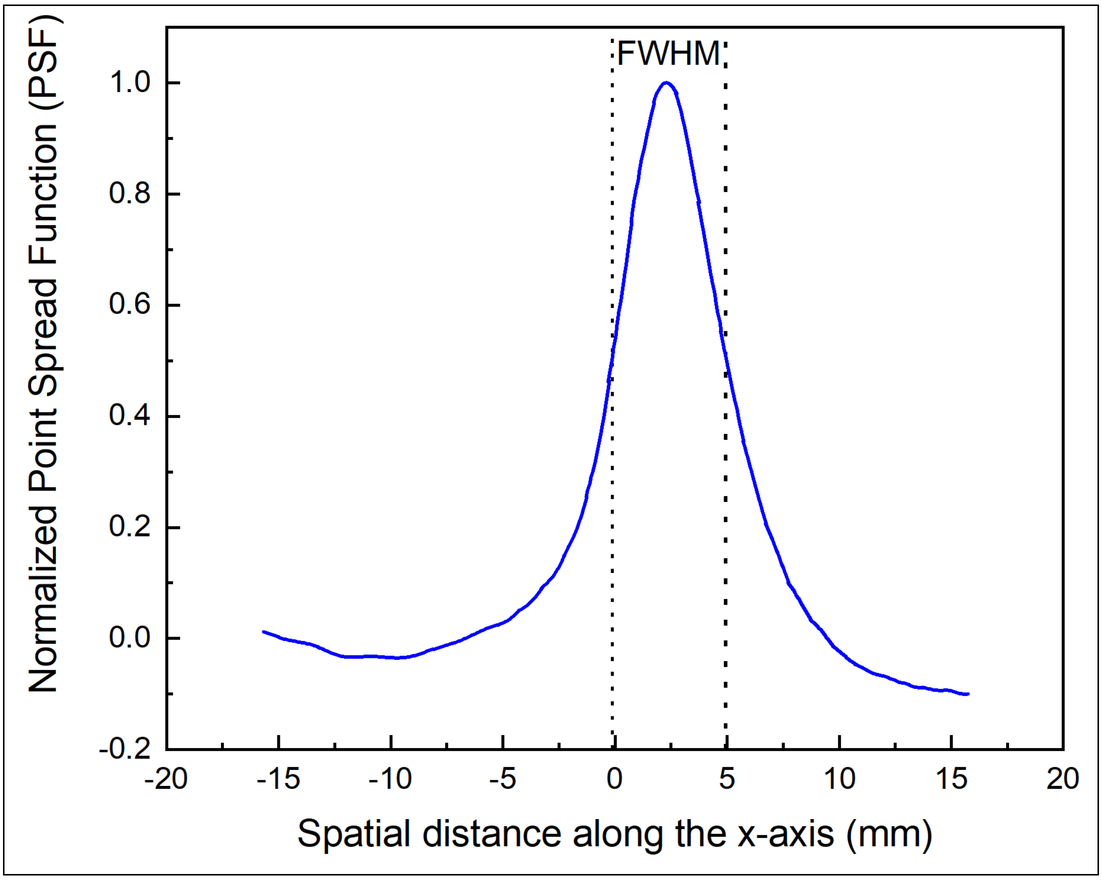

Figure 6.10: MPI signal of the Perimag sample at centered (z = 0) line.

The spatial resolution of the MPI signal for the z=0 line was measured as 5.06 mm (FWHM). Phantom imaging of 40 µl in a diameter of 3.5 mm glass tube. Five lines were scanned along the z-axis (perpendicular to the bore axis). MPI signals for the z-axis were acquired by following the same procedure. The spatial resolution of the overall MPI signal is larger than the centered PSF (3.5 mm). This may be affected by the thick phantom of 4 mm in diameter. Theoretically, a single point source can be considered for imaging. However, an experimentally certain amount of the sample keeps significant area/volume which may affect spatial resolution. Therefore, phantoms made of Perimag SPIONs can be distinguished with a gap of 5 mm. The considered sample was canned for 5 lines with a step distance of 1 mm along the z-axis. MPI signals established for the z-axis lines are presented in Figure 6.11. The spatial resolution of the individual MPI signals is similar to each other. Effective relaxation of the SPIONs plays a crucial role in MPI imaging. All signals were shifted to the right side as positive point spread functions were considered. Similarly, the relaxation effects can shift the negative PSFs to the left direction. The relaxation time of the MPI signals causes blurring in the final image which is another challenge that affects the spatial resolution and reduces the quality of the image.

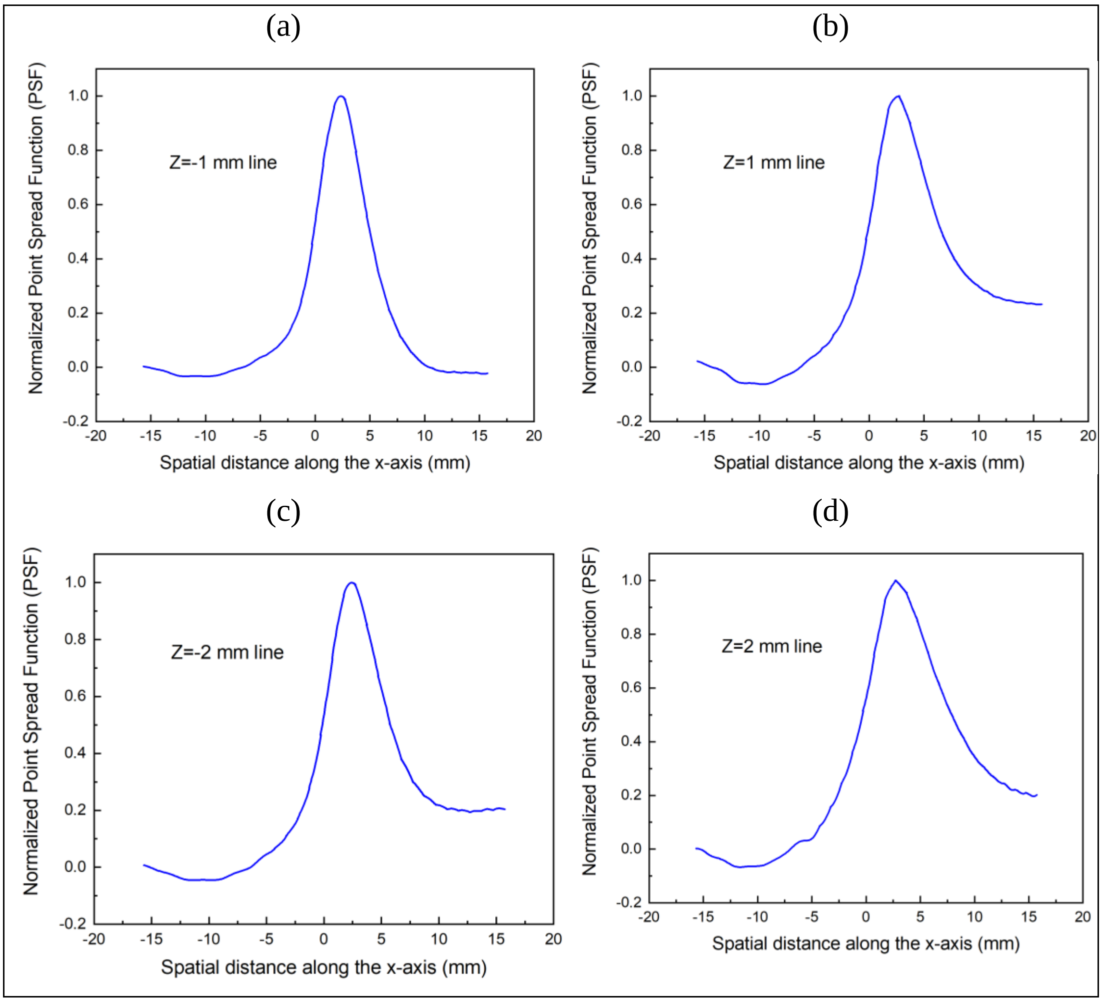

Figure 6.11: MPI signals along the z-axis (-2 mm to 2 mm).

6.4. Reconstructed Image

A single phantom of the Perimag sample was scanned as presented in the previous section inside FOV (-7 mm to 7 mm). A sinusoidal excitation field of 15 mT (peak amplitude) was applied to the drive coil. The phantom was attached to the 3D actuator and particle signals were recorded with a step of 1 mm distance. Five lines were recorded for the Perimag® sample and their MPI signals were presented in Figure 6.11. The recorded data of the 5 lines and 21 points on each line were mapped along the xz plane as shown in Figure 6.12.

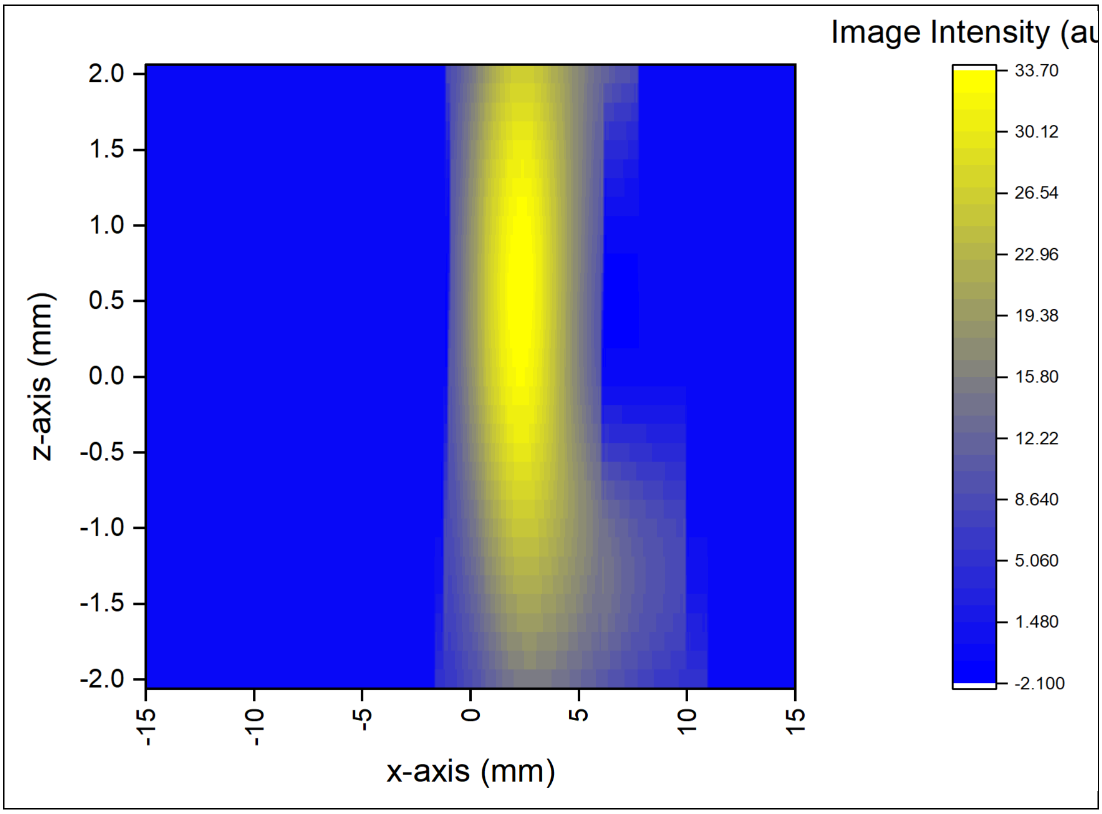

Figure 6.12: MPI image of the Perimag sample of 40 µl in a cylindrical phantom.

The maximum image intensity was evaluated as 33.70 (au) for the Perimag sample of 40 µl in 3 mm diameter of a glass tube. Other standard SPIONs of Vivotrax Plus in the cylindrical phantom were also scanned with the same specifications in the MPI scanner. The amount of the new sample was kept the same as of the previous one. The Perimag® has a concentration of 17 mg/ml, whereas the Vivotrax Plus has a concentration of 5.5 mg/ml. The new sample was scanned for 8 lines along the z-axis. The MPI signal for the centered line (z = 0 line) is presented in Figure 6.13. The FWHM of the Vivotrax Plus sample was measured as 7.16 mm. It is significantly larger than the Perimag sample which downplays the spatial resolution of the MPI device. As the hardware and other technical specifications were the same for both samples which support the dependency of the MPI resolution on the tracer agent (Perimag®, Vivotrax Plus, etc).

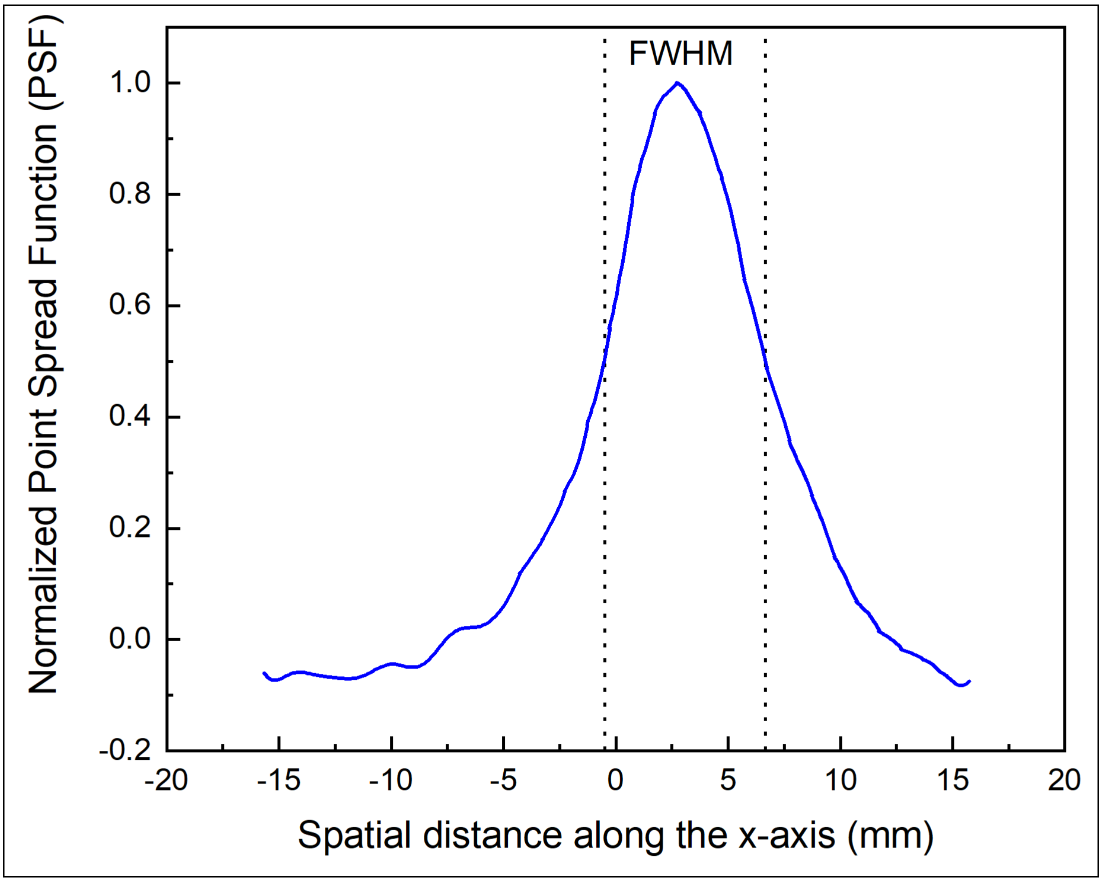

Figure 6.13: MPI signal of the Vivotrax Plus sample at centered (z = 0) line.

MPI signals with Vivotrax Plus samples were recorded for 8 lines along the z-axis. Overall, 21 data points were captured across the FFP with full coverage of the FOV. An MPI image was extracted from the acquired data for the spatial distribution of the new sample as shown in Figure 6.14. The maximum image intensity was measured as 7.30 (au) which is quite low as compared to the Perimag® sample. The iron concentration of the Vivotrax Plus is 3.9 times less than the Perimag sample that supports the low image intensity arguments.

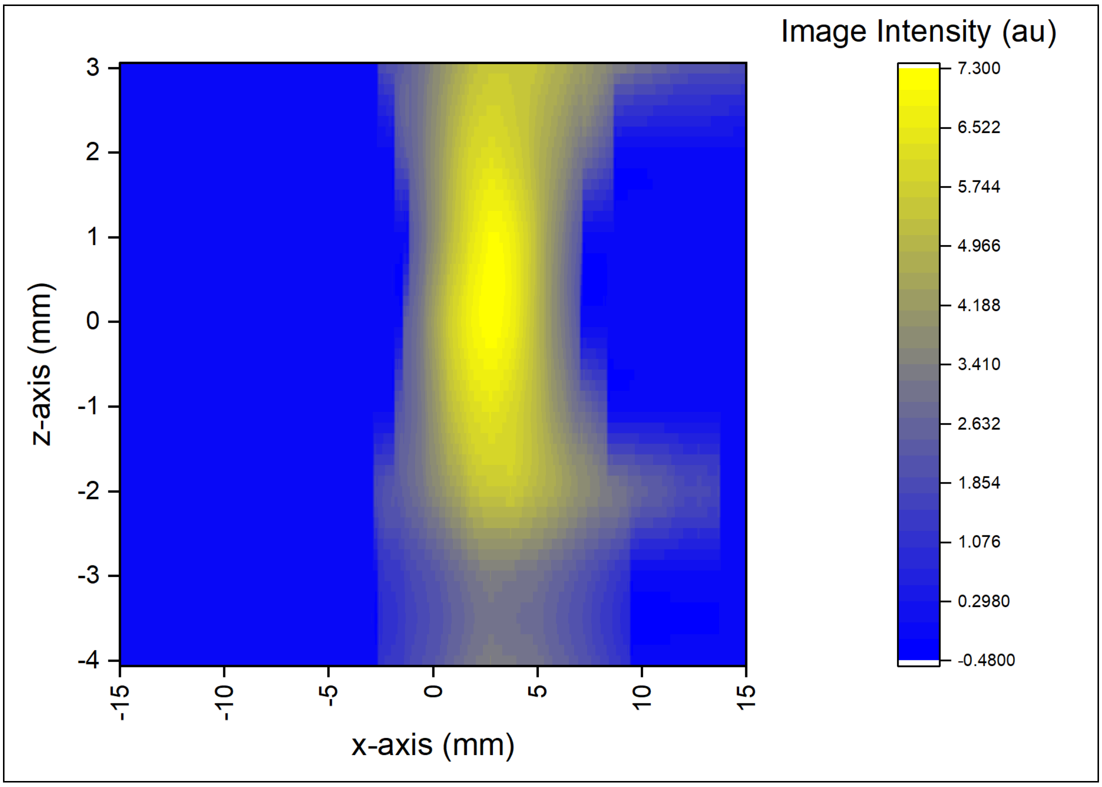

Figure 6.14: MPI image of the Vivotax Plus sample of 40 µl in a cylindrical phantom.

Finally, the spatial resolution of the MPI scanner can be improved with a higher selection field up to a certain limit. It can also be improved with better SPIONs (having fast relaxation and high magnetization) for MPI applications. In addition to this, the higher magnetization response of the tracer agents leads to a higher relative signal to achieve high SNR. Therefore, along with the hardware specifications of the MPI scanner, tracer agents also have significant importance in MPI imaging.

7. MPI SCANNER WITH 2D FIELD OF VIEW

MPI scanner presented in the 5th chapter has a small bore diameter (28mm) that is used for phantom imaging. In this chapter, a medium bore size of 50 mm was proposed with higher gradient field strength. Two pairs of drive and receive coils were used to speed up the scanning time of ROI. Solenoid drive and receive coils were used along the bore axis (x-axis) while saddle-shaped drive and receive coils were utilized along the fast gradient axis. Moreover, impedance matching circuits for drive coils, and bandstop filters (used for receive coils) were designed in LTSpice.

COMSOL Multiphysics was used as a simulation tool to visualize the MPI subsections and to calculate critical parameters before practical implementation. A custom design MPI scanner with 2D FOV with solenoid drive and receive coils was implemented as shown in Figure 7.1(a). Drive and receive coils can easily be replaced in this MPI scanner with 2D FOV. The Saddle-shaped drive and receive coils were placed instead of a solenoid system as shown in Figure 7.1(b). The signal flow of the MPI scanner is represented in Figure 7.1(c). The selection field setup is mentioned with N-S (North and South pole of the permanent magnet) sections above and below the drive and receive coils. The excitation signal generated by the data acquisition card (DAQ) is applied to the drive coil with the help of a power amplifier (PA) and other electronic circuits. The magnetic field generated by the drive coil is counter check with the current measurement using the current probe. The voltage signal induced by the superparamagnetic iron oxide nanoparticles (SPIONs) is connected to the low noise amplifier (LNA) for analog filtering and amplification and then recorded with DAQ.

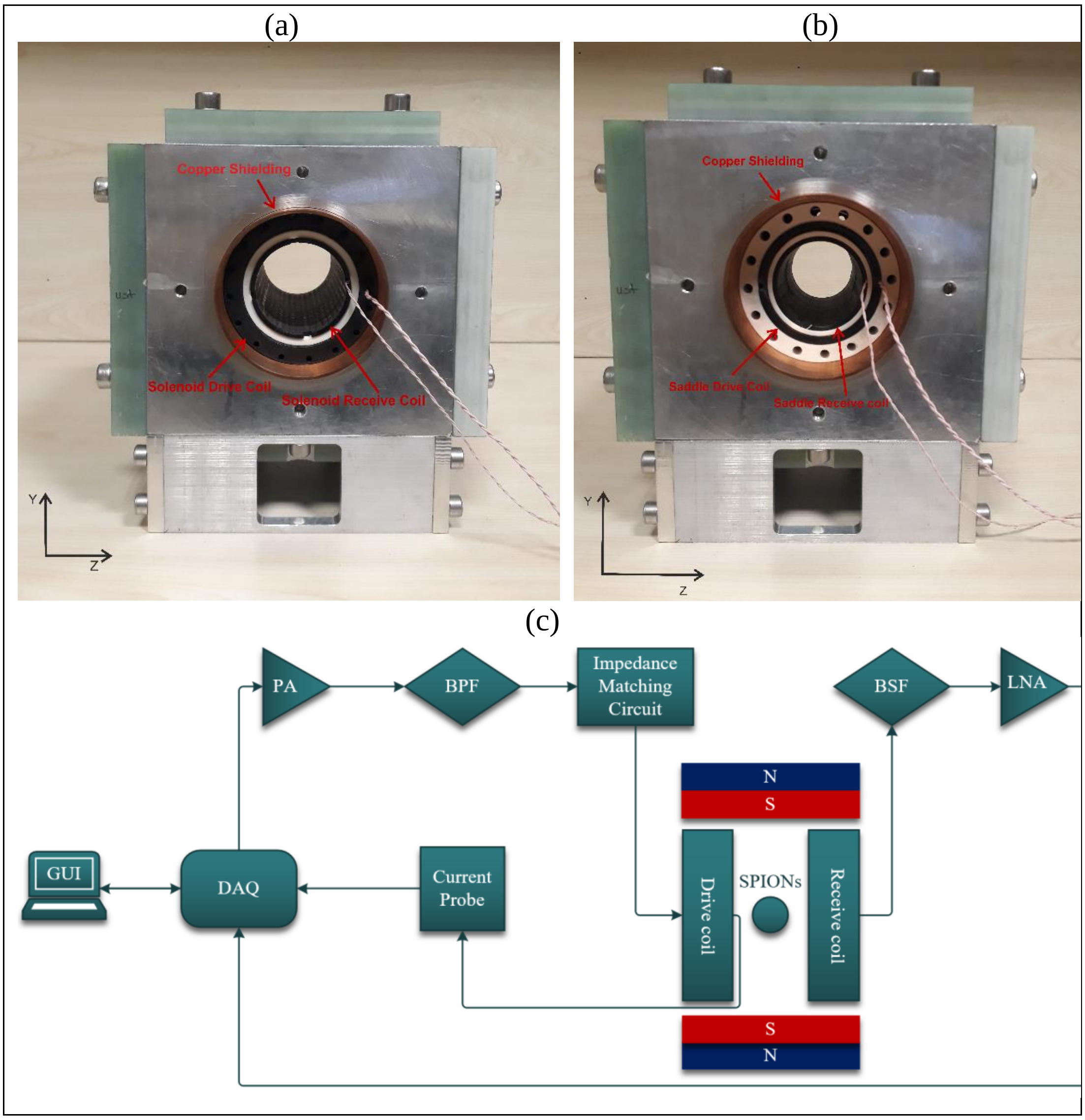

Figure 7.1: MPI scanner with 2D FOV; (a) MPI scanner with 2D FOV with solenoid drive and receive coils, (b) MPI scanner with 2D FOV with saddle-shaped drive and receive coils, (c) Generalized signal chain for two pairs of drive and receive coils (solenoid and saddle).

7.1. Selection Field Implementation

MPI scanner hardware part consists of permanent magnets, copper shielding, transmit coil, and receive coils. Resolution and imaging space (volume or area) are critical parameters of MPI device. All research groups (worldwide) work on moderate bore size for phantom and animal (i.e., rat, mouse) imaging. As far as phantom imaging is concerned, approximate bore diameter of 28 mm should be an appropriate selection. However, to perform imaging for small animals bore size should be enhanced. So, bore size 52 mm diameter was proposed for in-vitro and in-vivo experiments and hardware components were upgraded accordingly.

After imaging space selection, spatial resolution is a highly significant parameter. A selection field of 4.3 T/m perpendicular to the bore axis and 2.15 T/m along the bore axis was used in the 1D MPI scanner presented in the 5th chapter. As the drive coil was implemented along the bore axis so the spatial resolution of the image was restricted to 5 mm. To improve the spatial resolution of the MPI scanner with 2D FOV, a selection field of approximately 6 T/m was designed and implemented along the bore and perpendicular to the bore axis (in-between magnets). The selection field magnets are fixed with epoxy sheets in the MPI scanner with 2D FOV are shown in Figure 7.2.

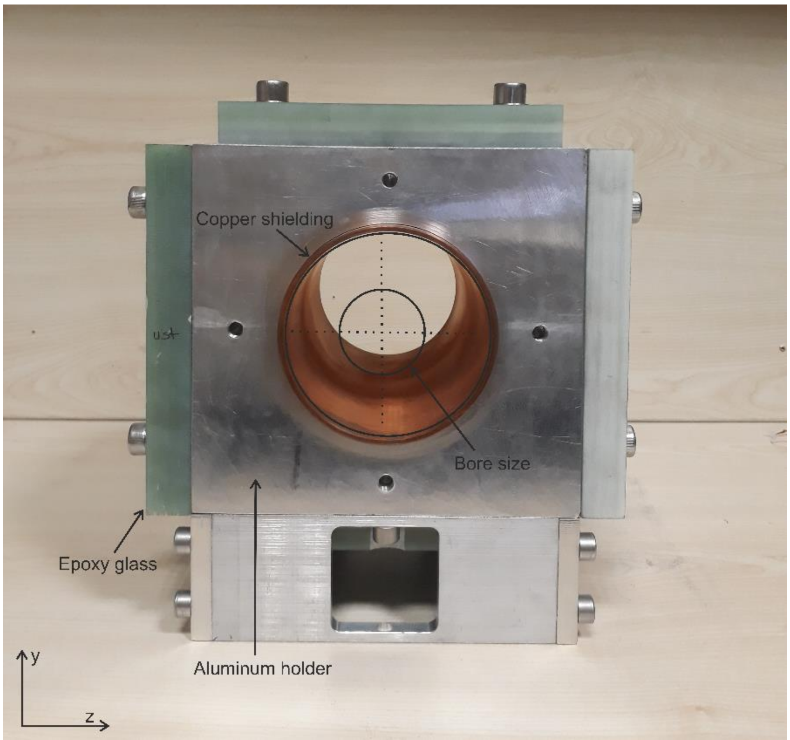

Figure 7.2: MPI scanner with 2D FOV; The selection field components are supported with fiberglass (G10). A large bore size is mentioned in the middle of the hardware system. Copper shielding is sandwiched between selection and drive field components to protect from each other effects. MPI holder was made of 99.99% of Aluminum.

Two different magnet arrangements were planned to be achieved high gradient fields along the bore and perpendicular to the bore axis. One is a single magnet pair used as discussed in chapters 4 and 5 for the 1D MPI scanner. The second plan is based on double magnet pairs (4 permanent magnets) to obtain high gradient field strength along the bore axis as shown in Figure 7.6.

7.1.1. Selection Field with Two Magnets System

FFP topology basically can be implemented with a single pair of permanent magnets, as discussed in chapter 5. However, it only produced a high gradient field between the magnets. It was planned to use saddle-shaped drive coils to exploit the high gradient field strength perpendicular to the bore axis. A selection field with single pair permanent magnets was implemented, and magnetic field measurements were measured with a transverse probe of the gaussmeter (Lakeshore Corporation). Experimental data and numerical simulation results were compared as shown in Figure 7.3.

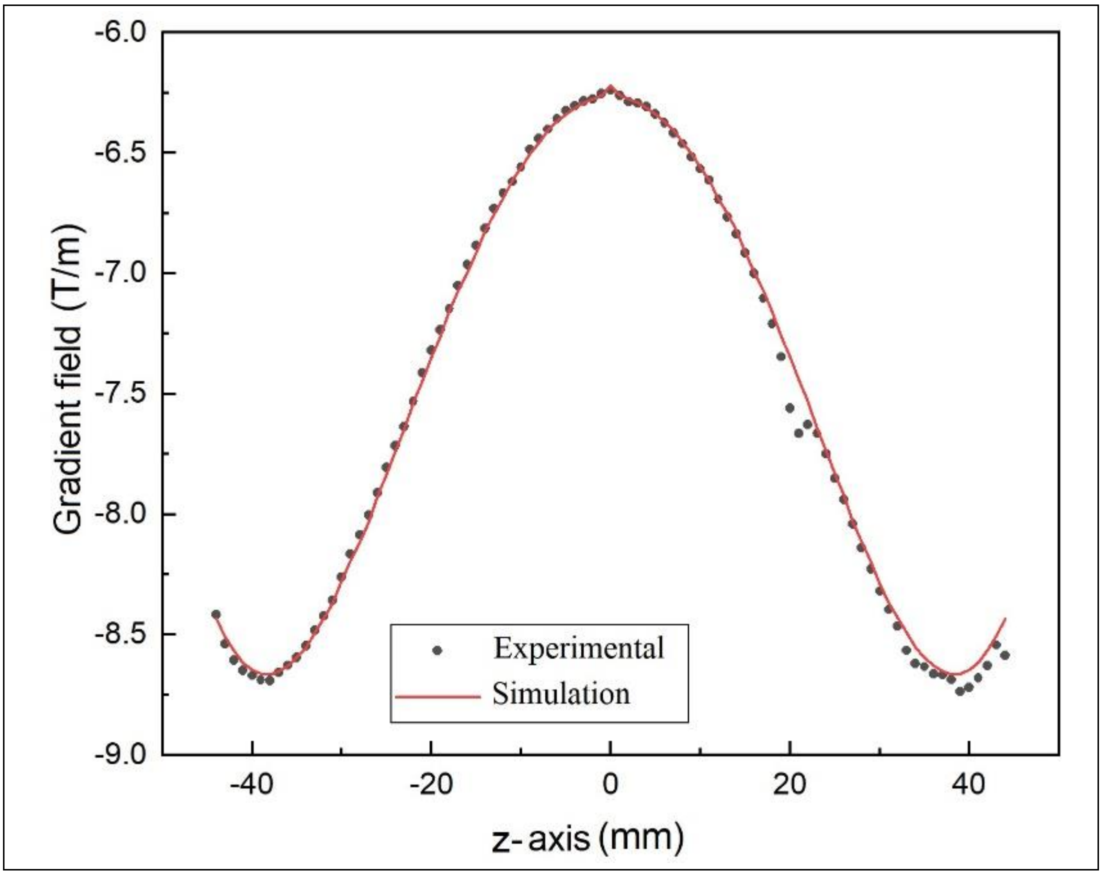

Figure 7.3: Gradient field strength (T/m) normal to the bore axis.

6.25 T/m was obtained as the absolute gradient field strength at z = 0 mm. It directly improves the resolution of the MPI scanner with 2D FOV. The axial probe of

DSP (Lakeshore Corporation) was used to measure the magnetic field values in the xy plane along the bore axis (called as x-axis here) at z = 0 as shown in Figure 7.4(a). Similarly, the transverse probe was also used to measure the magnetic field in the xy plane as presented in Figure 7.4(b).

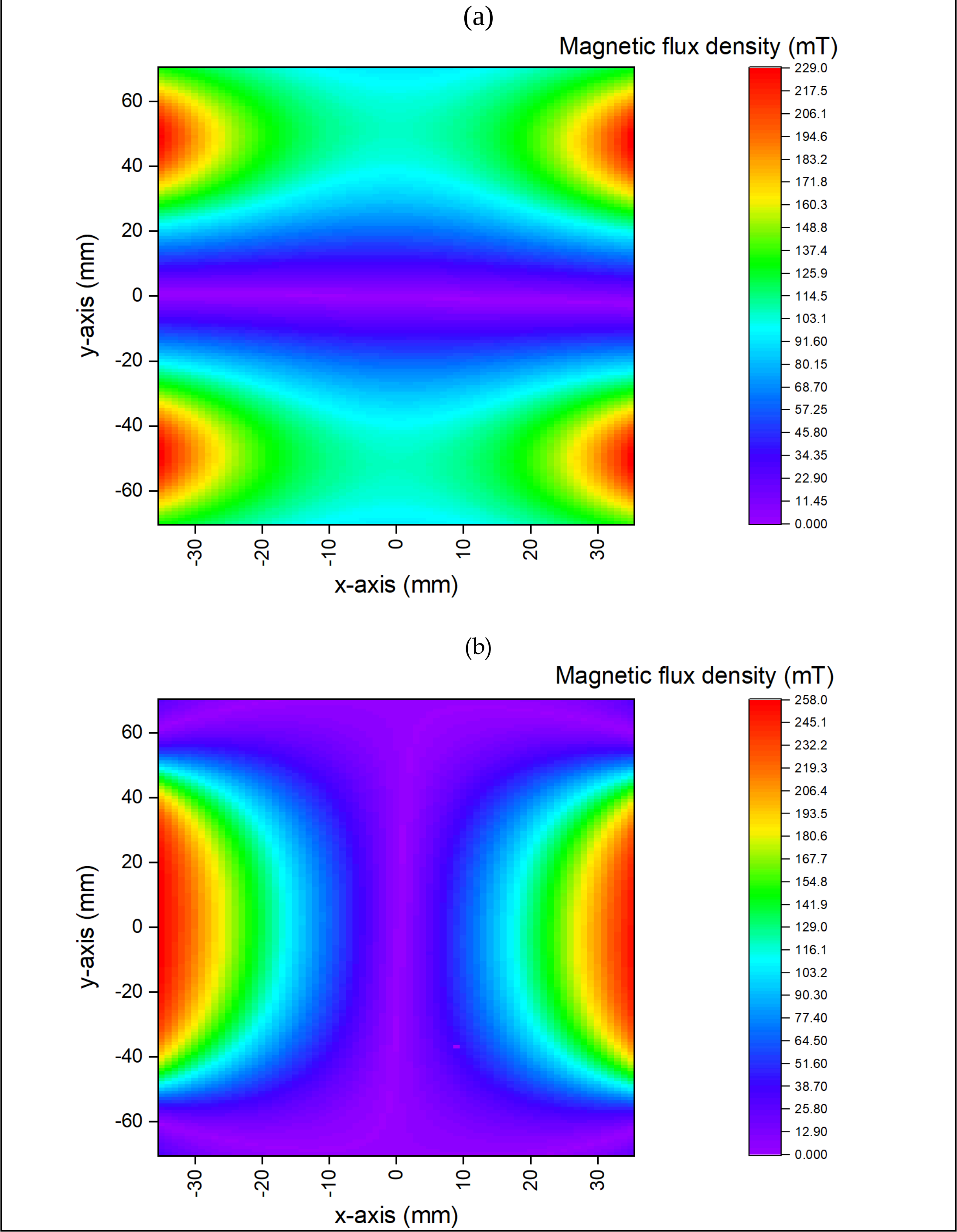

Figure 7.4: Magnetic profiles at z = 0 plane, a) measurement with the axial probe, b) measurement with the transverse probe.

Magnetic field patterns are not symmetric in each plane, e.g., circular in xy-plane and elliptical in yz and xz planes. The data measured for the z = 0 plane with the individual probes were combined to see the overall magnetic field patterns as shown in Figure 7.5.

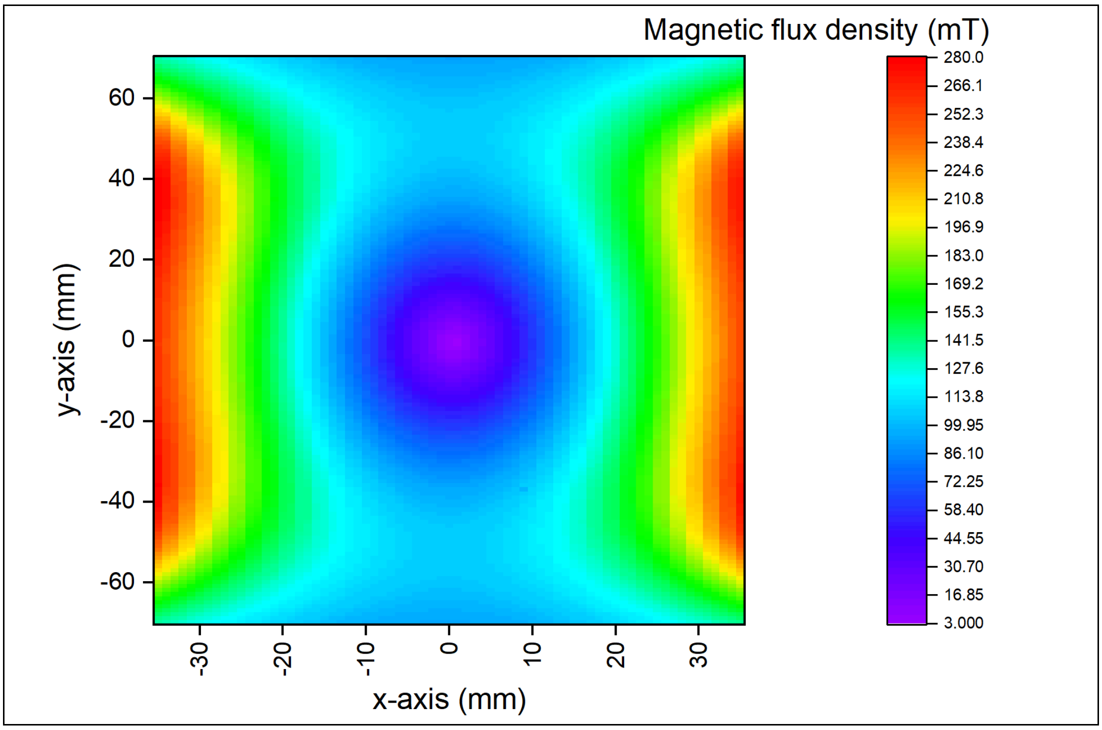

Figure 7.5: Field free point (FFP) is produced at the center of the xy-plane magnetic field.

7.1.2. Selection Field with Four Magnets System

3D space dimension was utilized in COMSOL Multiphysics to simulate the magnetic flux density of the two magnet pairs designed based on Maxwell configuration. The diameter of the magnets is 100 mm with different thicknesses. The magnetic flux density inside 80 mm around the midpoint (FFP) of the setup is shown in Figure 7.6.

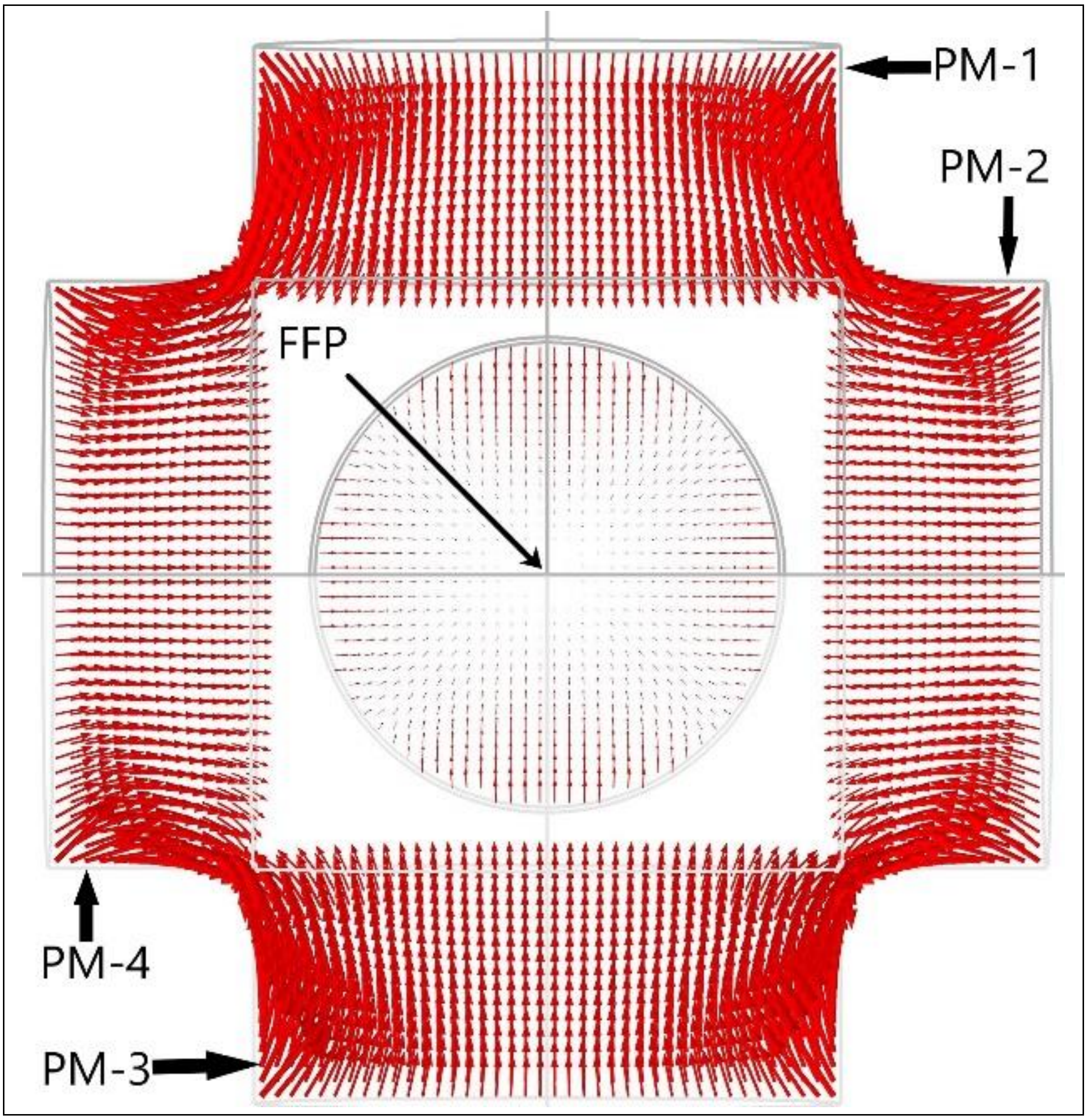

Figure 7.6: Magnetic flux density of the two pairs system in YZ plane; pole magnets of PM-1 and PM-3 are oppositely placed. Similarly, pole magnets of PM-2 and PM-4 are also oppositely placed. No magnetic field exists at the center of the system.

High magnetic fields at the corner of the magnets show high stress that can be prevented with a strong holder. The gradient field strength for each axis was obtained from the spatial gradient of the magnetic fields along the corresponding axis. The gradient field along the x-axis (along the bore axis) is shown in Figure 7.7. The highest gradian field appeared at the x = 0 mm location. The magnets were arranged to achieve the highest gradient field along the x-axis.

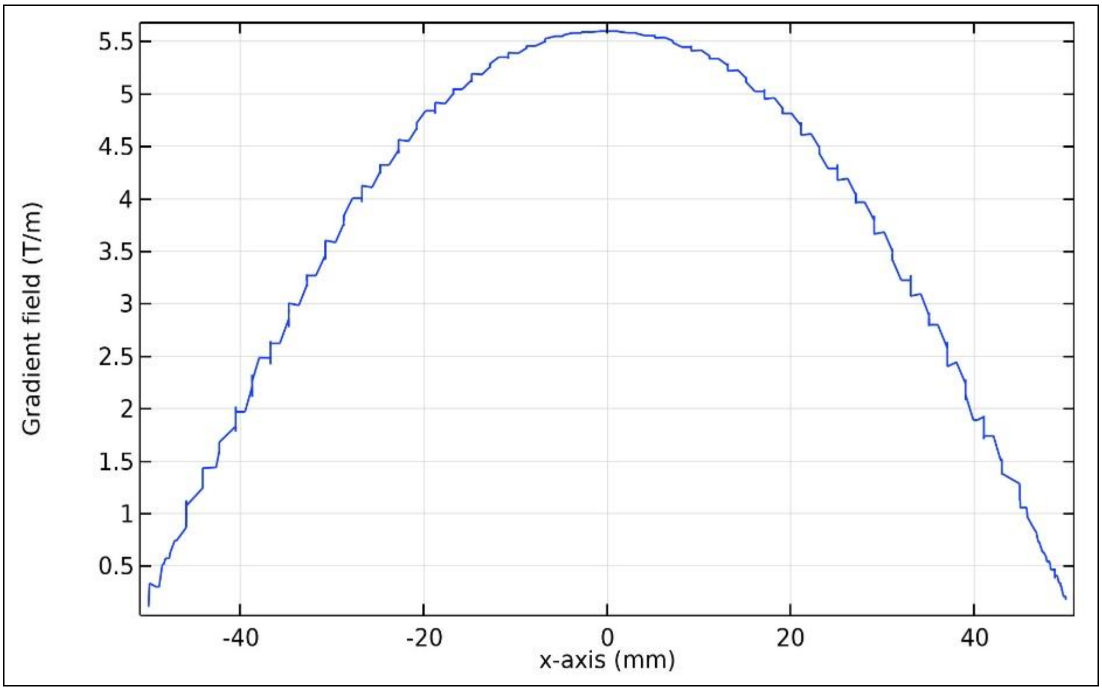

Figure 7.7: Gradient field along the x-axis with two pairs of permanent magnets.

7.2. Solenoid Drive-Receive System

Imaging along the bore axis can be performed with Maxwell-based cylindrical coils (two coils) or with a single solenoid coil. Solenoid coil can produce better homogeneity for the excitation field as compared to the two coils setup for the drive coil. Technical parameters of the solenoid (internal diameter, outer diameter, and length) were optimized with COMSOL Multiphysics simulations. The gradiometric receive coil was designed in three sections to minimize coupling between the drive and receive coils which cause feedthrough interference. Outer sections of the receive coils were wounded oppositely to the middle section with a specific air gap between consecutive sections. Axisymmetric 2D space dimension simulation technique was utilized for modeling solenoid drive and receive coils in COMSOL. The drive and receive coil parameters were optimized in the presence of copper shielding which is a very essential part of the MPI scanner once the selection field is implemented with permanent magnets. Moreover, the shielding effect improves the homogeneity of the excitation field. However, it reduces the sensitivity of the drive and receives coils depending on the air gap between the shielding and electromagnetic coils. The solenoid drive and receive coil were constructed based on numerical results from

COMSOL as shown in Figure 7.8(a). The magnetic flux density of the solenoid drive coil is presented in Figure 7.8(b).

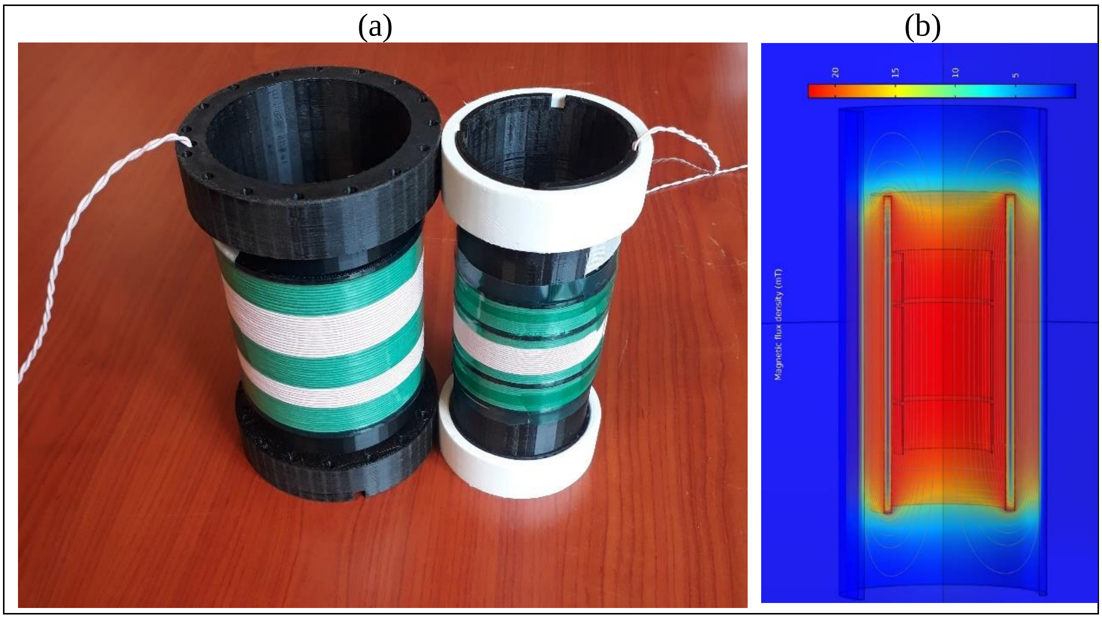
(a) (b)

Figure 7.8: Solenoid drive-receive coil system; a) Hardware implementation, b) Magnetic flux density of the solenoid drive coil and influence of copper shielding. The homogeneous magnetic flux density in the middle of the setup is visible.

The main purpose of the shielding is to prevent dynamic magnetic fields from reaching permanent magnets. Moreover, the thickness of the shielding is also critical to get rid of the skin depth issue of the eddy currents. The response of the tracers inside the field of view (FOV) is measured in electrical voltage form. So, coupling effect analysis in voltage signal is important for receive coil parameters. Outer sections of the receive coil generate similar but opposite polarity voltage for cancellation of the fundamental harmonics of the excitation field as shown in Figure 7.9.

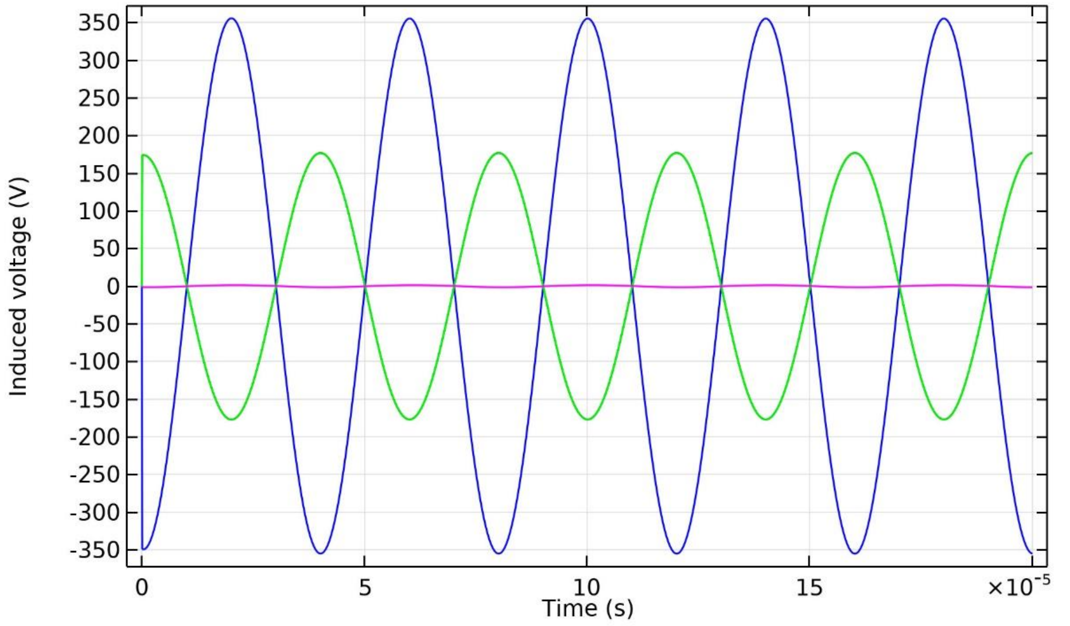

Figure 7.9: Induced voltages at individual sections of the receive coil; middle section voltage with blue color, outer sections voltage with green color, and the overall voltage across receive coil is mentioned with the purple color curve.

Theoretically or numerically, it is possible to get a 0 V overall signal without a sample. However, practically it is very difficult. So far, we have 250 mV which is quite a significant improvement in hardware optimization. All simulations were conducted at 20 mT excitation field strength for the solenoid drive coil as shown in Figure 7.8. Color homogeneity in the revolve view of the solenoid drive coil simulation represents the uniform nature of the excitation field inside FOV.

Litz wire of 1.20 mm diameter was utilized for double layer construction of the drive coil. Two layers drive coil was designed to achieve 20 mT (peak amplitude) magnetic flux density. The internal diameter of the drive coil is 76 mm. The drive coil inductance of 338.65 µH was measured with LCR 8105 G meter. Similarly, a single layer receive coil has an inductance of 58.30 µH. Physical and electrical key parameters of the drive and receive coils at 9.2 kHz are given in Table 7.1.

Table 7.1: Key parameters of the solenoid drive and receive coils at 9.2 kHz.

	Drive Coil	Receive Coil
Number of layers	2	1
Number of Turns	120	16:29:16
Length (mm)	72	48.8
Width (mm)	2.40	0.70
Internal diameter (mm)	76	59
Resistance (Ω)	1.47	0.967
Inductance (µH)	338.65	58.30

7.2.1. Sensitivity of Solenoid Drive Coil

The mechanical holder of the drive coil was made from a PLA material printed with a 3D printer. Magnetic flux density generated by the drive coil was directly controlled with current passing through it. The drive coil was placed in the cylindric copper shield which also reduced the efficiency of the coil depending on the air gap between the drive coil and copper shielding. The magnetic flux density profile of the drive coil was measured at 1A (DC). The profile of the drive coil sensitivity in the xz plane is presented in Figure 7.10(a). The comparison of numerical and experimental results for the drive coil sensitivity along the x-axis (y=0, z=0) is shown in Figure 7.10(b). The magnetic flux density of 1.49 mT was measured at the center of the drive coil at 1A direct current. Numerical and experimental results are in good agreement in terms of field homogeneity and efficiency (mT/A). Magnetic field homogeneity of 95% was achieved from -14 mm to +14 mm across the midpoint of the drive coil.

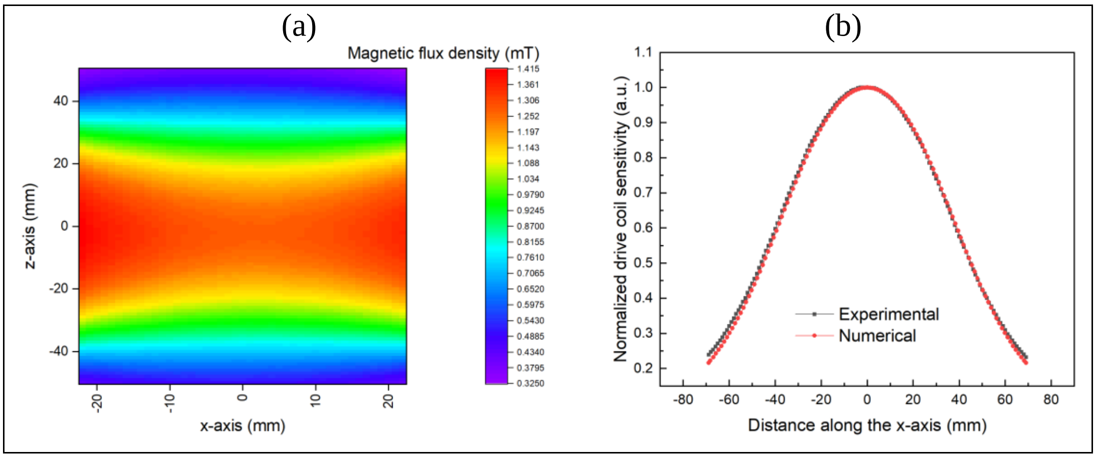

Figure 7.10. Sensitivity of the solenoid drive coil: (a) sensitivity profile of the drive coil in the xz plane at y = 0 line, (b) Normalized line sensitivity along the x-axis (y=0, z=0).

7.2.2. Sensitivity of Solenoid Receive Coil

The supporting holder of the receive coil was also built from a PLA material with a 3D printer. The length of receive coil is 48.8 mm which is made from 3 sections based gradiometric type. The middle section is almost equal to the outer sections (upper and lower) of the receive coil. Litz wire of 0.70 mm (as diameter) was used for the receive coil. The sensitivity profile of the receive coil was measured at 1A (DC) as shown in Figure 7.11(a). Receive coil has two winding gaps at the upper and lower sections. Zero magnetic field lines at z= +13 mm and z=-13 mm represented the sign changes of the magnetic fields. Magnetic field measurements were taken with a step distance of 1 mm. Numerical and experimental results were compared, and their results are presented in Figure 7.11(b). The magnetic flux density of 0.16 mT was measured at the center of the drive coil at 1A direct current. Numerical and experimental results are in good agreement in terms of field homogeneity and efficiency (mT/A). Magnetic field homogeneity of 90% was achieved from -5 mm to +5 mm across the midpoint of the drive coil (at the middle section). Gradient field homogeneity of the selection field and homogeneous magnetic field of the drive coil are very crucial to correlate the theoretical and experimental boundaries of the FOV. As both magnetic fields are highly homogenous inside the FOV region, so minimum artifacts would appear in the reconstructed image.

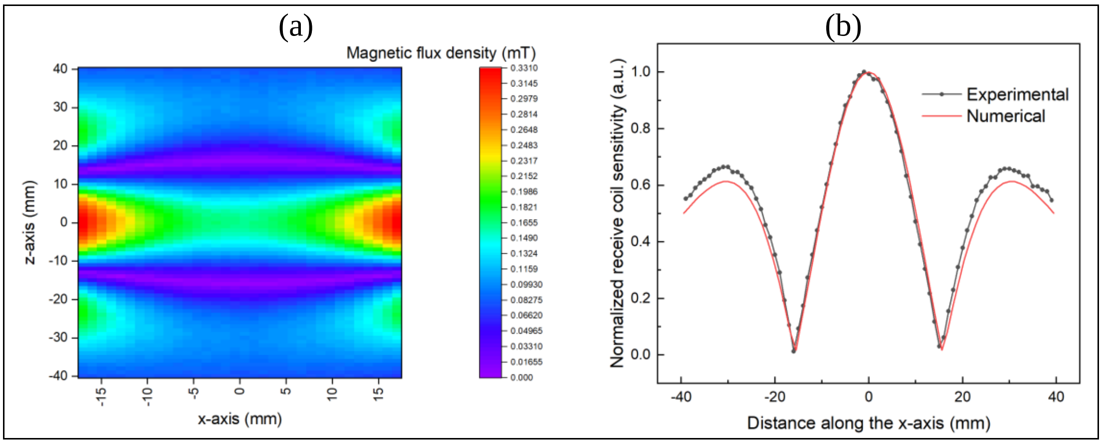

Figure 7.11. Sensitivity of the solenoid receive coil: (a) Sensitivity profile of the receive coil in the xz plane at y = 0 line, (b) Normalized line sensitivity along the x-axis (y=0, z=0).

7.3. Saddle Drive-Receive System

To compete with an existing medical devices acquisition time of MPI should be minimum. In addition to the solenoid drive and receive system, saddle drive and receive coil system was also designed to scan the plan area instead of the line as presented in Figure 7.12.

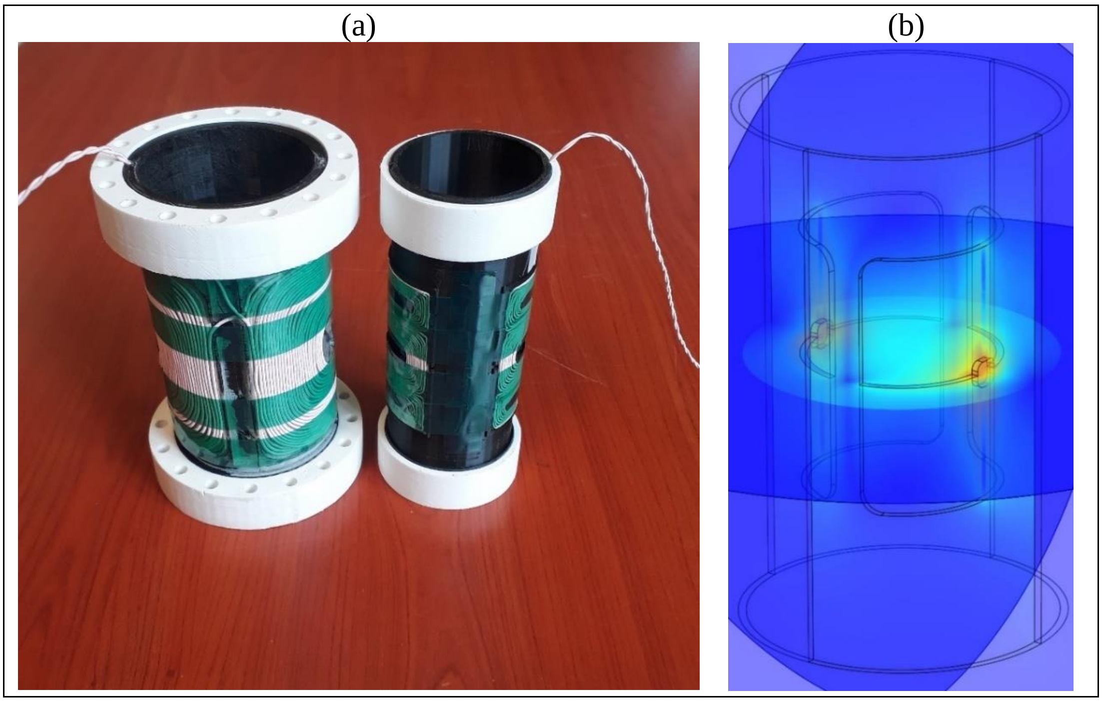

Figure 7.12: Saddle-shaped drive-receive system; a) Hardware implementation, b) Magnetic flux density of the drive coil.

The drive and receive coils consist of two spatially separated parts but are serially connected for electronic signals. Technical parameters (internal diameter, internal free space, and length) of the drive coil are optimized to achieve 15 mT using COMSOL Multiphysics. Voltage signals across the drive and receive coils are critical to reducing the coupling of the fundamental part of the operating frequency at 9 kHz. The excitation field generated by the drive coil is in phase with current passing through the coil. The voltage across the series-connected parts of the saddle drive coil is shown in Figure 7.13.

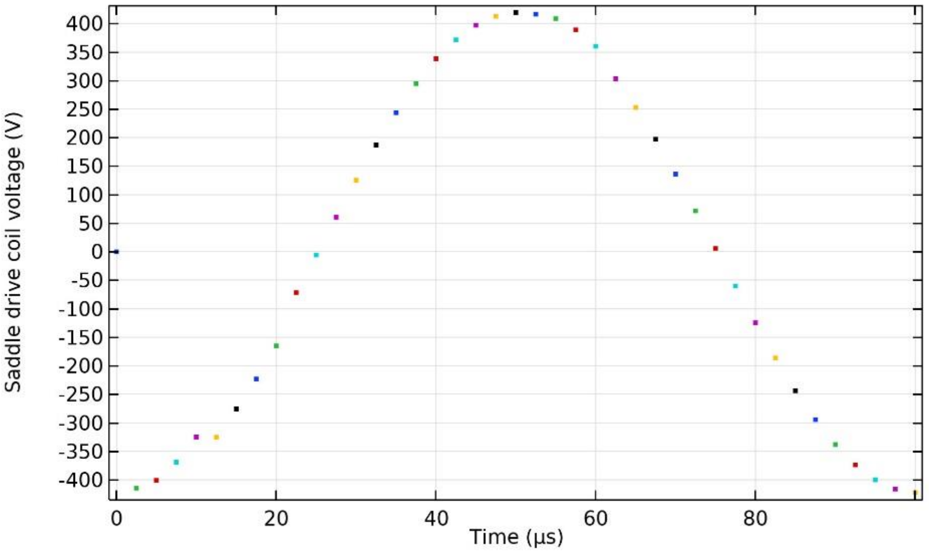

Figure 7.13: Voltage across the saddle drive coil of the MPI scanner with 2D FOV.

The drive and receive coils were simulated using the 3D space dimension in COMSOL Multiphysics. Saddle coils are not in linear or circular shapes. So, it is hard to compute simulations. The parametric sweep tool was used to perform simulation at limited points instead of continuous-time intervals. Similar to the gradiometric solenoid receive coil, the saddle receive coil was also planned to implement it in the same way. The middle section of the receive coil was simulated as shown in Figure 7.14.

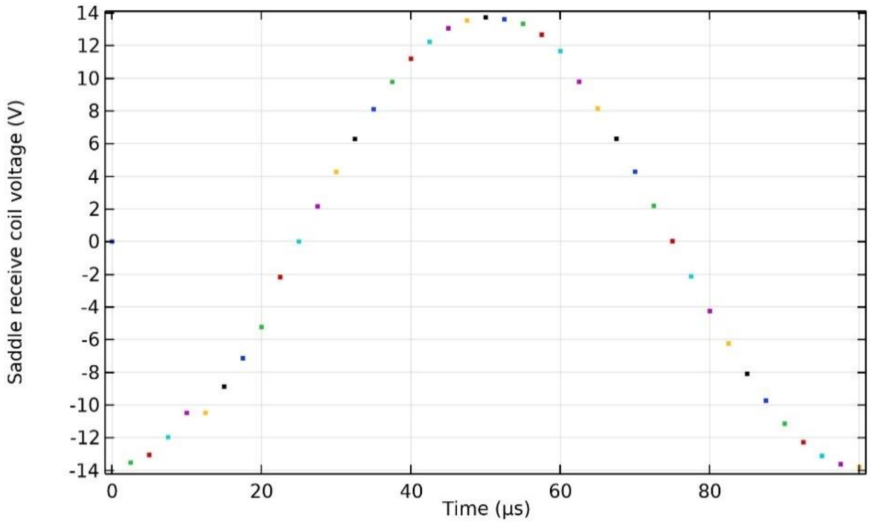

Figure 7.14: Induced voltage across the middle section of saddle-shaped receive coil.

Overall gradiometric saddle-shaped receive coil will have 6 spatially separated parts. It is difficult to keep them intact, however, a single holder can reduce human efforts. Litz wire of 1.20 mm diameter was utilized for the multilayer's construction of the drive coil. Two layers drive coil was designed to achieve 15 mT (peak amplitude) magnetic flux density at minimum current. The internal diameter of the drive coil is 66 mm. Drive coil inductance of 189.12 µH was measured with LCR 8105 G meter. Similarly, a single layer receive coil has an inductance of 28 µH. Physical and electrical key parameters of the drive and receive coils at 9 kHz are given in Table 7.2.

Table 7.2: Key parameters of the saddle-shaped drive and receive coils at 9 kHz.

	Drive Coil	Receive Coil
Number of layers	2	1
Number of Turns	51:51	8:12:8
Length (mm)	86	62
Width (mm)	2.40	0.70
Internal diameter (mm)	66	53
Resistance (Ω)	0.790	0.662
Inductance (µH)	189.12	28

7.3.1. Sensitivity of Saddle Drive Coil

The mechanical holder of the drive coil was made from a PLA material printed with a 3D printer. Magnetic flux density generated by the drive coil was directly controlled with current passing through it. The drive coil was placed in the cylindric copper shield which also reduced the efficiency of the coil depending on the air gap between the drive coil and copper shielding. The magnetic flux density profile of the drive coil was measured at 1A (DC). The profile of the drive coil sensitivity in the xz plane is presented in Figure 7.15(a). The comparison of numerical and experimental results for this drive coil sensitivity along the x-axis (y=0, z=0) is shown in Figure 7.15(b). The magnetic flux density of 0.83 mT was measured at the center of the drive coil at 1A direct current. Numerical and experimental results are in good agreement in terms of field homogeneity and efficiency (mT/A). Magnetic field homogeneity of 105% was achieved from -8 mm to +8 mm across the midpoint of the drive coil.

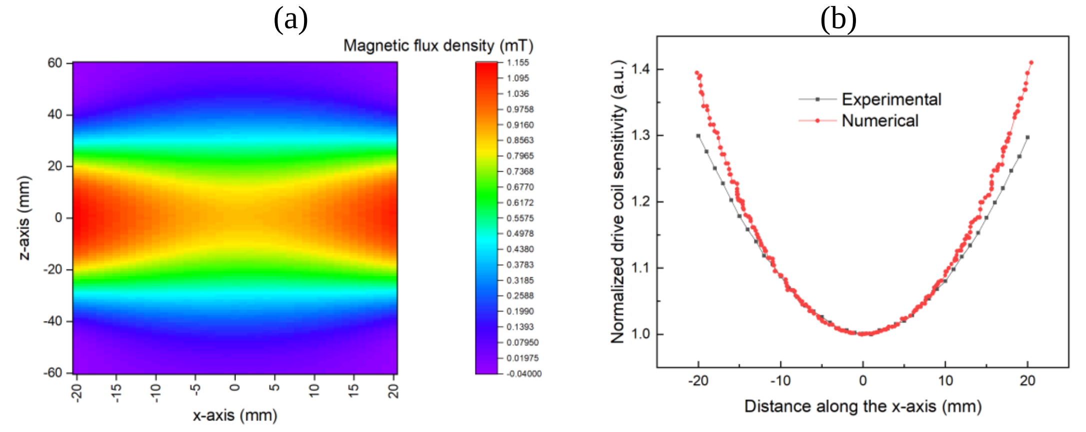

Figure 7.15. Sensitivity of the saddle drive coil: (a) Sensitivity profile of the drive coil in the xz plane at y = 0 line, (b) Normalized line sensitivity along the x-axis (y=0, z=0).

7.3.2. Sensitivity of Saddle Receive Coil

The supporting holder of the receive coil was built from a PLA material with a 3D printer. The length of receive coil is 62 mm which is made from 3 sections based gradiometric type. The middle section is almost equal to the outer sections (upper and lower) of the receive coil. Litz wire of 0.70 mm (as diameter) was used for the saddle receive coil. The sensitivity profile of the saddle receive coil was measured at 1A (DC) as shown in Figure 7.16(a). Receive coil has two winding gaps at the upper and lower sections. A zero magnetic field lines at z= +13 mm and z=-13 mm represents the sign changes of the magnetic fields. Magnetic field measurements were taken with a step distance of 1 mm. The line sensitivity along the x-axis is presented in Figure 7.16(b). The magnetic flux density of 0.14 mT was measured at the center of the drive coil at 1A direct current. Numerical and experimental outcomes are in good agreement in terms of field homogeneity and efficiency (mT/A). Magnetic field homogeneity of 90% was achieved from -4 mm to +4 mm across the midpoint of the drive coil (middle section).

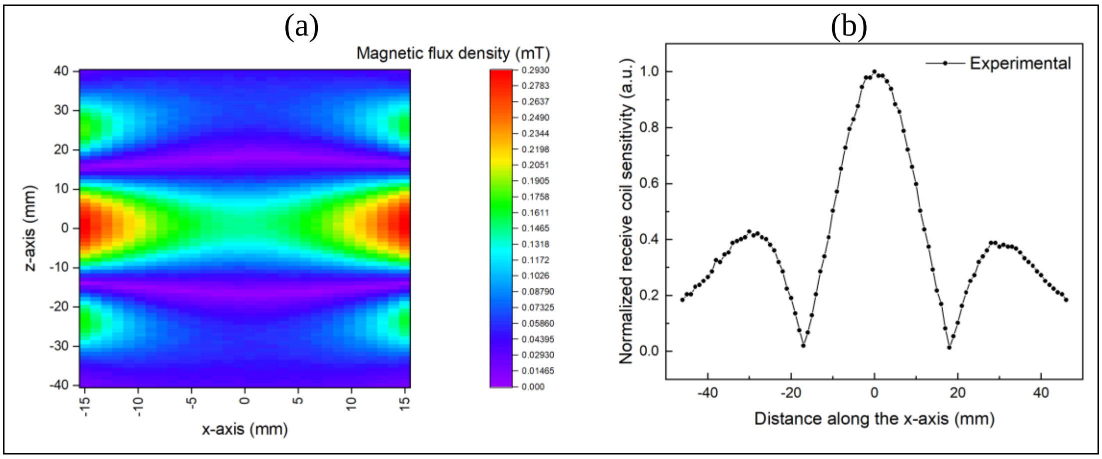

Figure 7.16. Sensitivity of the saddle receive coil: (a) Sensitivity profile of the receive coil in the xz plane at y = 0 line, (b) Normalized line sensitivity along the x-axis (y=0, z=0).

7.4. Analog Filters for Drive and Receive Coils

Resonance filters were designed for the drive coils to minimize power consumption and reduce heat loss. Resonance filters also act as low pass filters which helps the drive chain of MPI scanner to attenuate the higher frequency component of the operating frequency. Similarly, resonance filters made of LC network were integrated into the receive coils to eliminate the direct feedthrough component in addition to the geometric-based reduction of the fundamental harmonic of the operating frequency. The resonance filter in the solenoid drive coil and bandstop filter in the solenoid receive coil were designed at 9.2 kHz as shown in Figure 7.17(a). Similarly, the resonance filter in the saddle drive coil and bandstop filter in the saddle receive coil were also designed at 9 kHz as shown in Figure 7.17(b).

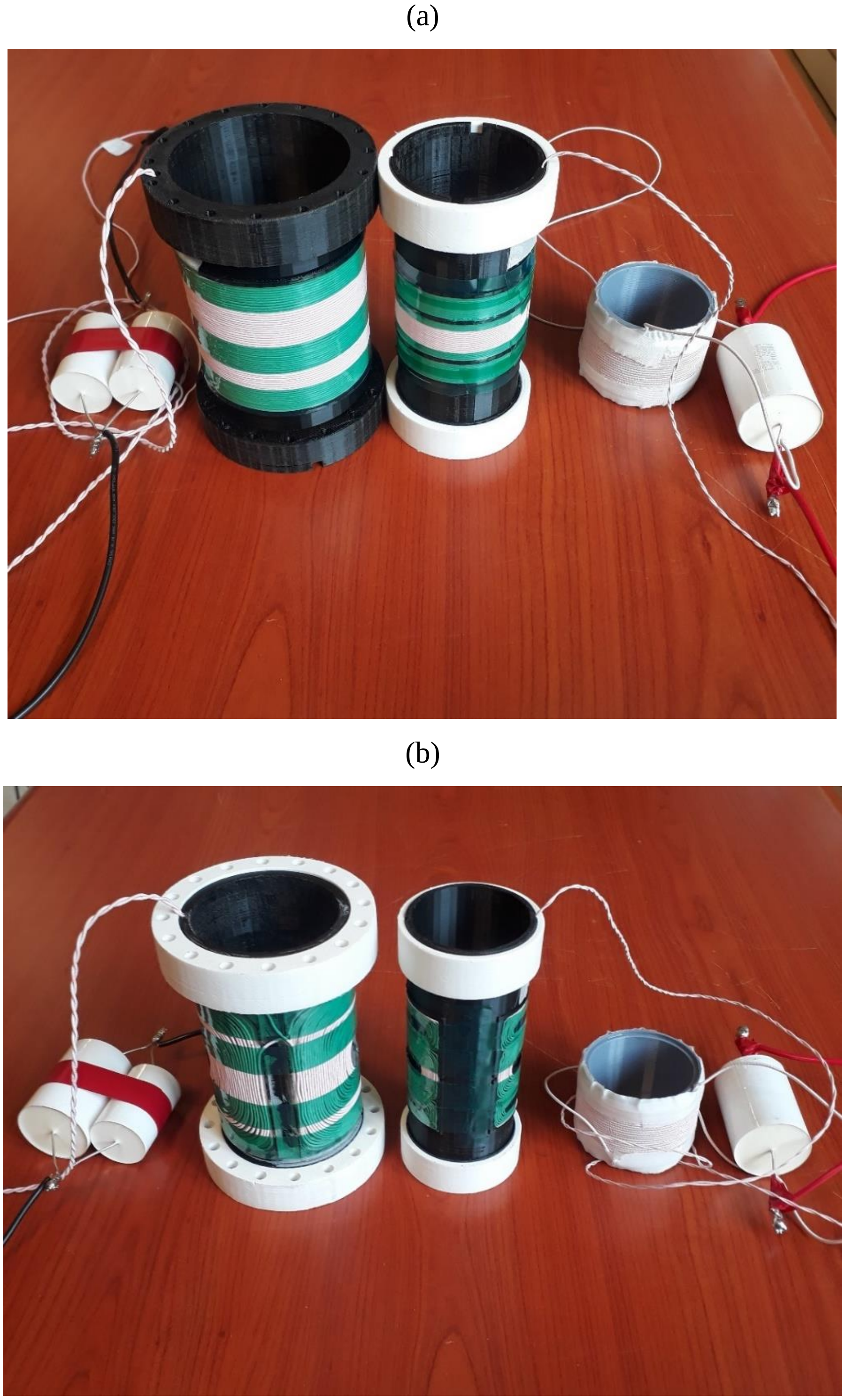

Figure 7.17. Resonance and bandstop filters for drive and receive chain of MPI scanner: (a) Solenoid drive and receive coil system, (b) Saddle drive and receive coil system.

7.4.1. Impedance Matching of Solenoid Drive Coil

There are two purposes of impedance matching circuits; the first one is maximum power transfer, and the second purpose is maximum signal transfer. Power amplifier and impedance circuit are used to accomplish signal transfer with maximum efficiency. The power amplifier has 5.3 mΩ resistance and the solenoid coil with a resonant capacitor has 1.47 Ω. High impedance of the load (electromagnetic coil and resonant capacitor) ensures maximum power transfer of the drive chain. Therefore, there is no need for impedance matching between source and load. Only maximum signal (current) transfer was implemented with a series capacitor. Impedance matching circuit (acting as a low pass filter) was designed in LTSpice for the solenoid drive coil as shown in Figure 7.18.

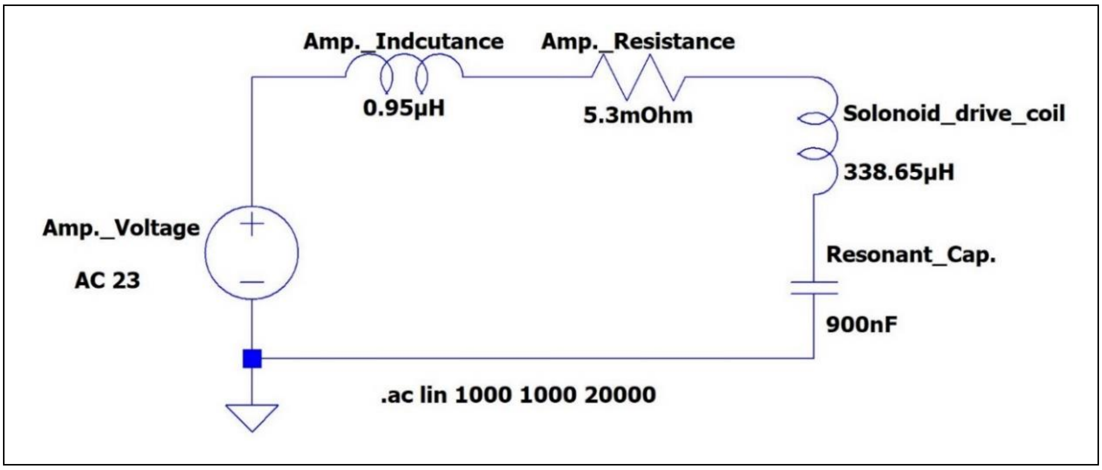

Figure 7.18: Impedance matching circuit for the solenoid drive coil of the MPI scanner with 2D FOV.

Internal reactance and internal resistance of the power amplifier were also included to simulate realistic behavior. Required capacitance reactance to the drive chain was added with the high current capacitor of 926 nF. The resonance and excitation frequency of the drive chain was designed to be 9.2 kHz. The impedance of the load (electromagnetic coil and resonant capacitor) was evaluated at 9.2 kHz as shown in Figure 7.19(a). The maximum current capability of the drive chain at the excitation frequency was evaluated in LTSpice, as shown in Figure 7.19(b).

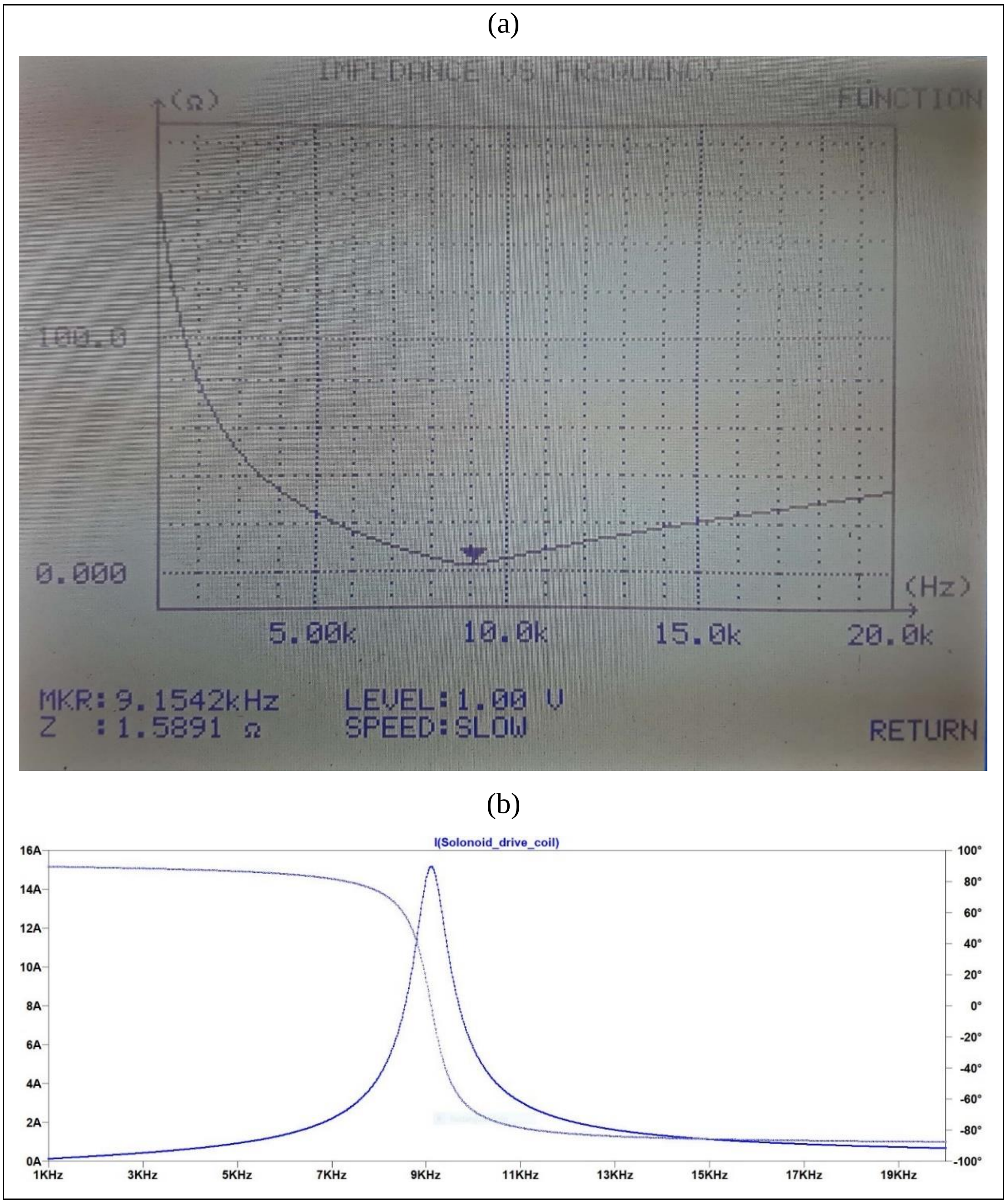

Figure 7.19: Frequency response of the solenoid drive chain: (a) Impedance of the drive chain (drive coil and resonance filter) was measured with LCR 8105G meter, (b) Frequency response of the drive coil circuit. The drive coil has the highest current capability at the resonance frequency (simulated with LTSpice).

To suppress higher harmonics of the operating frequency, a low pass or bandpass filter is necessary for MPI applications. Attenuation rate of -20dB/decade helps to reduce the intensity of unwanted multiple harmonics of the excitation frequency produced from the power amplifier.

7.4.2. Resonance Band Stop of Solenoid Receive Coil

In addition to gradiometric design of the receive coil, the drive side of the MPI system was kept simple as the focus was on receive side of the system. Both drive and receive coil were designed like a transformer in the LTspice environment. The coupling between the drive and receive coil was taken as 10% for simulation purposes. To observe the effectiveness of the band-stop filters only two sources of 9.2 kHz (main frequency) and its 3rd harmonic was as generated as a signal source in LTSpice. The most simplified resonant band-stop filter was considered under the scope of this thesis as shown in Figure 7.20.

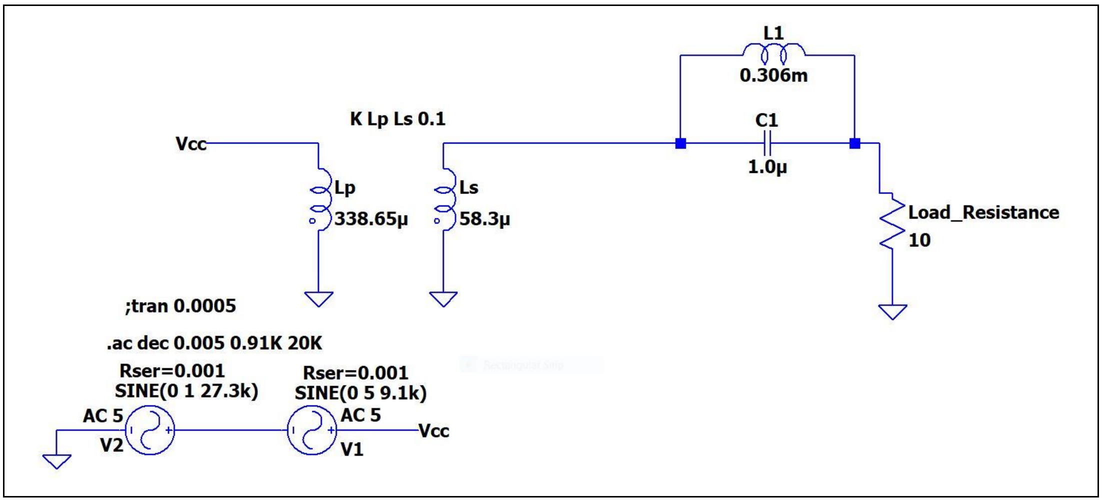

Figure 7.20: Impedance matching circuit for the solenoid receive coil of the MPI scanner with 2D FOV.

Impedance response of the solenoid receive coil was measured with LCR 8105G meter from 1-20 kHz. It shows the maximum impedance at 9.2 kHz as presented in Figure 7.21(a). An air core inductor of 306 µH and a low equivalent series resistance (ESR) capacitor of 1 µF were utilized to design a bandstop filter at 9.2 kHz. The current through simple resistive load was evaluated in LTSpice as shown in Figure 7.21(b). The coupling frequency component was reduced by -30 dB with a simple resonant filter in the receive chain.

(a)

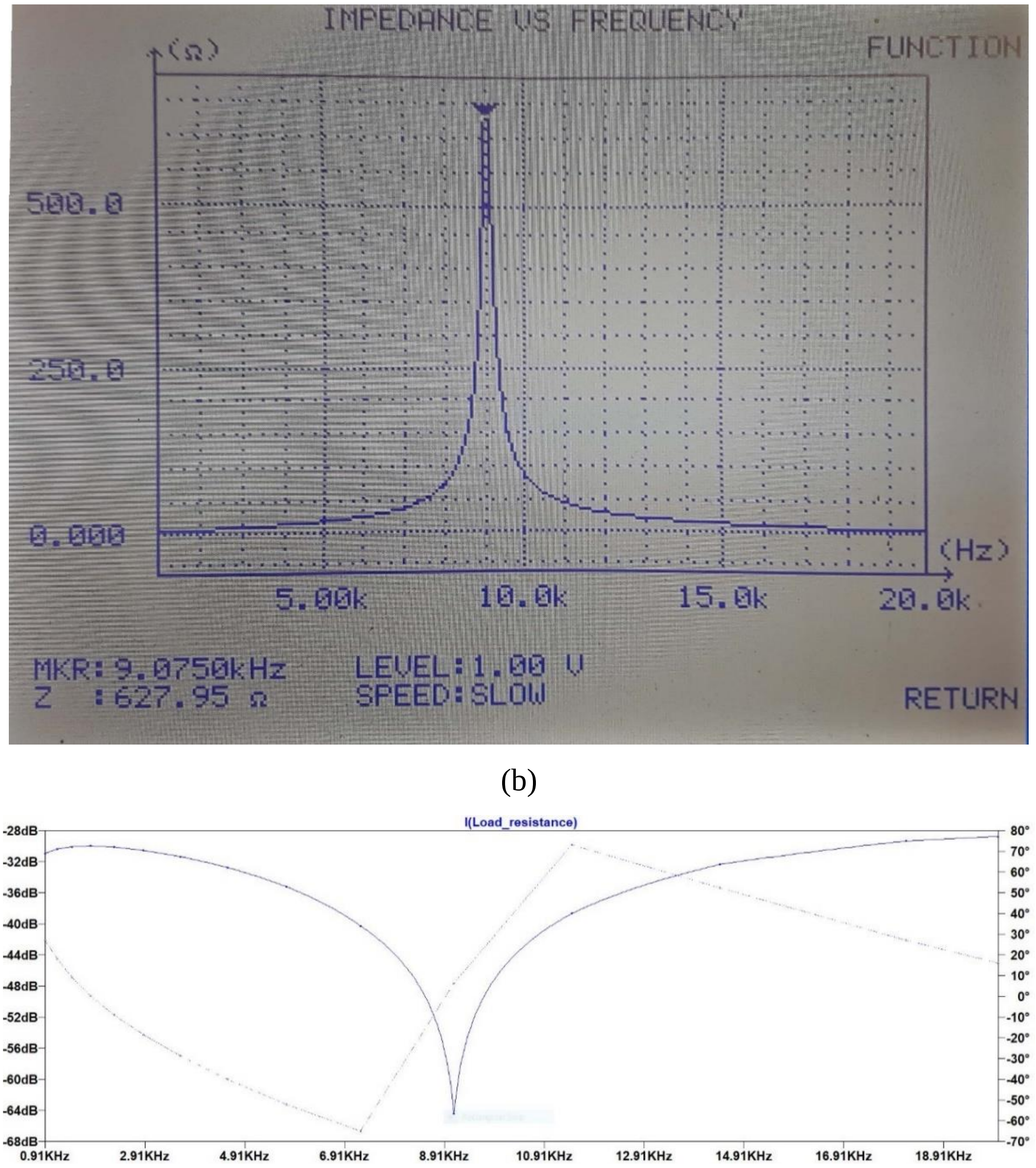

(b)

Figure 7.21: Frequency response of the receive chain: (a) Impedance of the receive chain (receive coil and resonance filter) was measured with LCR 8105G meter, (b) Frequency response of receive coil circuit, receive coil shows the maximum current reduction at the resonance frequency (simulated with LTSpice).

7.4.3. Self-Resonance of Solenoid Drive and Receive Coil

Optimum excitation frequencies of the drive coils for MPI applications are close to 25 kHz. Since MPI is at the pre-clinical stage, a wide range of excitation frequencies are utilized below 100 kHz. In the design of electromagnetic coils for MPI, the issue of self-resonance should be addressed carefully. Practically, each inductor has a stray capacitance parallel to the inductor. Therefore, the self-resonance of the drive coils for

MPI applications is at least 10 times higher than the operating frequency (9.2 kHz) [86]. The frequency response of the drive coil is presented in Figure 7.22(a). The self-resonance of 282 kHz of the drive coil was measured with an 8105G LCR meter. So, this drive coil can easily operate up to 282 kHz for MPI applications. Self-resonance of the receive coil is highly critical because a receive coil is used to record multiple harmonics of the excitation frequency. Therefore, a wide bandwidth spectrum is essential for the receive coil. The frequency response of the receive coil is shown in Figure 7.22(b). It is clearly shown that the resonance peak occurred at 2.54 MHz which ensures multiple harmonics that can be recorded up to 2.54 MHz.

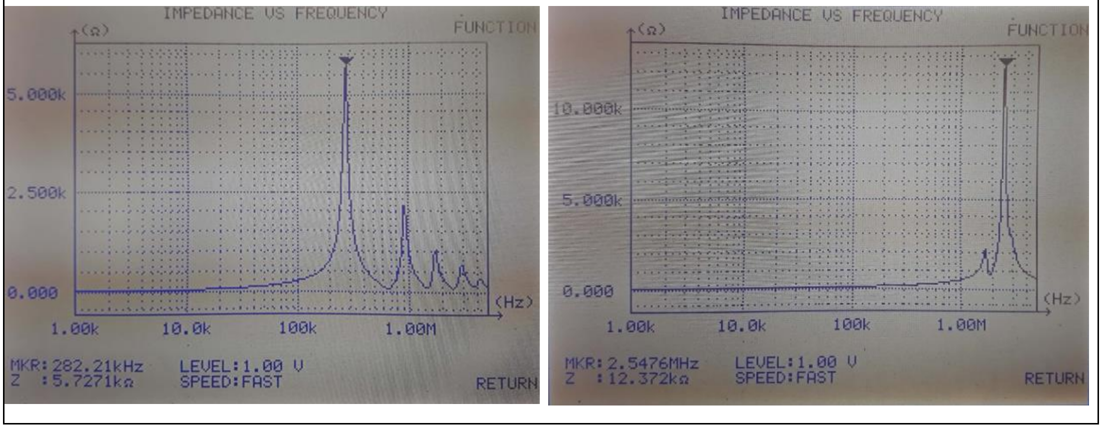
(a)

(b)

Figure 7.22: Self-resonance of the solenoid coils: (a) Drive coil, (b) Receive coil.

7.4.4. Impedance Matching of Saddle Drive Coil

There are two purposes of impedance matching circuits, the first one is maximum power transfer, and the second purpose is maximum signal transfer. Power amplifier and impedance circuit are used to accomplish signal transfer with maximum efficiency. The power amplifier has 5.3 mΩ resistance and the saddle coil with resonant capacitor has 0.790 Ω. High impedance of the load ensures maximum power transfer of the drive chain. Therefore, there is no need for impedance matching between source and load. Only maximum signal (current) transfer was implemented with a series capacitor. Impedance matching circuit (acting as low a pass filter) was designed in LTSpice for the saddle drive coil as shown in Figure 7.23.

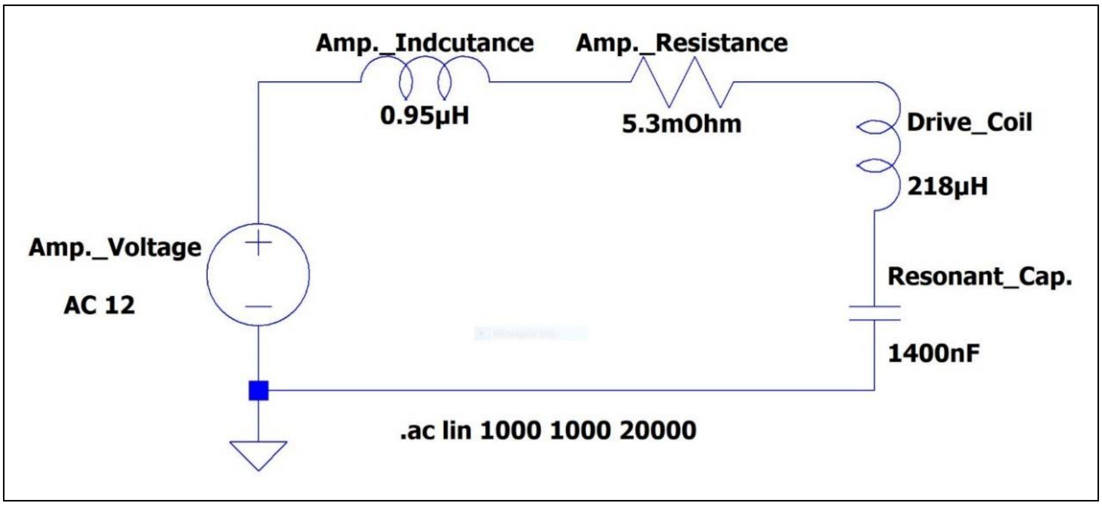

Figure 7.23: Impedance matching circuit for saddle drive chain of the MPI scanner.

Internal reactance and internal resistance of the power amplifier were also included to simulate realistic behavior. Required capacitance reactance to the drive chain was added with the high current capacitor of 1.43 µF. The resonance and excitation frequency of the drive chain were designed to be 9 kHz. The impedance of the load (electromagnetic coil and resonant capacitor) was evaluated at 9 kHz, as shown in Figure 7.24(a). The maximum current capability of the drive chain at the excitation frequency was evaluated in LTSpice, as shown in Figure 7.24(b). To suppress higher harmonics of the operating frequency, a low pass or bandpass filter was necessary for MPI applications. Attenuation rate of -20dB/decade helps to reduce the intensity of unwanted multiple harmonics of the excitation frequency produced from the power amplifier.

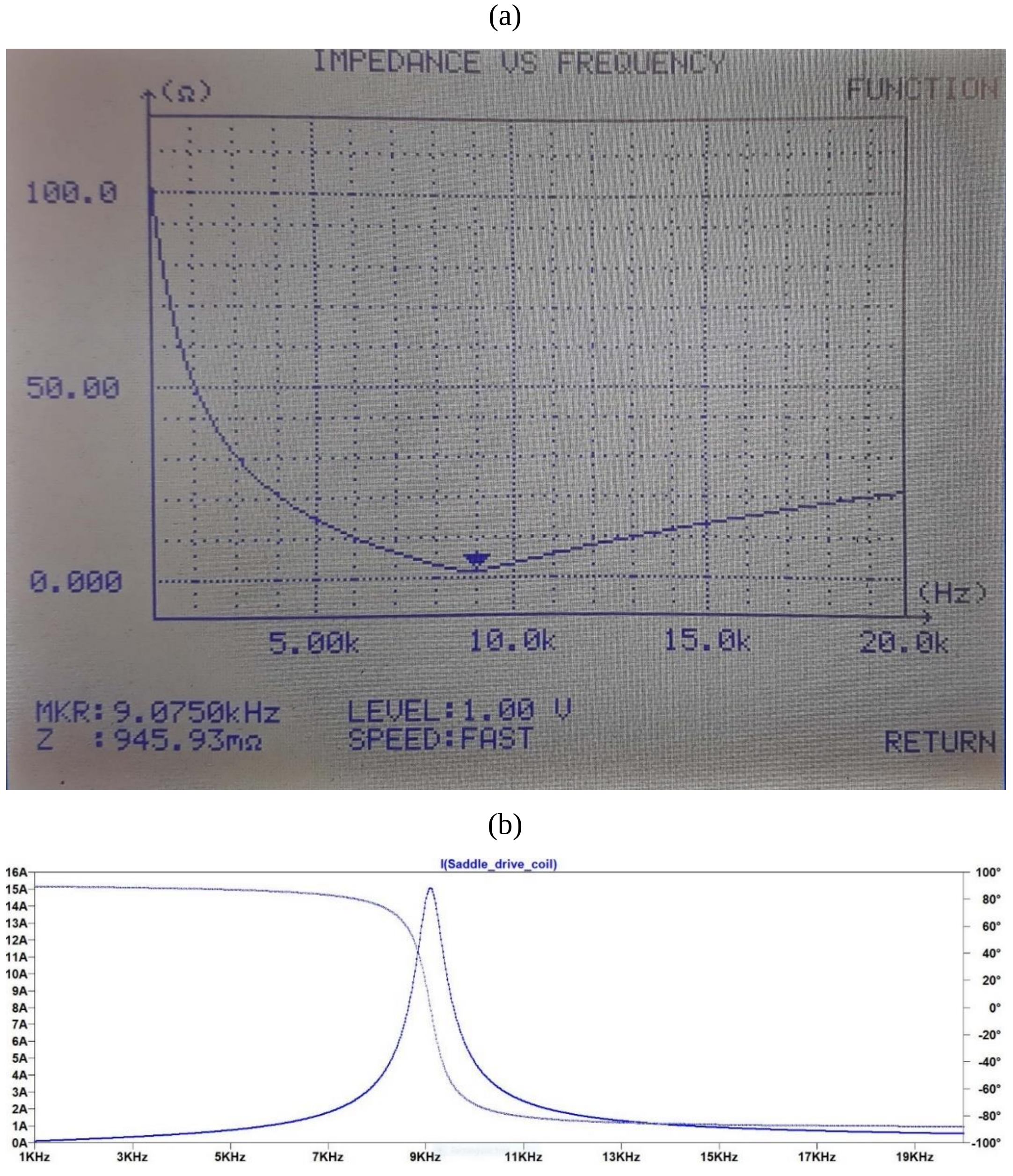

Figure 7.24: Frequency response of the drive chain: (a) Impedance of the drive chain (drive coil and resonance filter) was measured with LCR 8105G meter, (b) Frequency response of drive coil circuit, drive coil has the highest current capability at the resonance frequency (simulated with LTSpice).

7.4.5. Resonance Band Stop of Saddle Receive Coil

In addition to gradiometric design of the receive coil, the drive side of the MPI system was kept simple as the focus was on receive side of the system. Both drive and receive coils were designed like a transformer in the LTspice environment. The coupling between the drive and receive coil was taken as 10% for simulation purposes.

To observe the effectiveness of the band-stop filters only two sources of 9 kHz (main frequency) and its 3rd harmonic was as generated as a signal source in LTSpice. The most simplified resonant band-stop filter was considered under the scope of this thesis as shown in Figure 7.25.

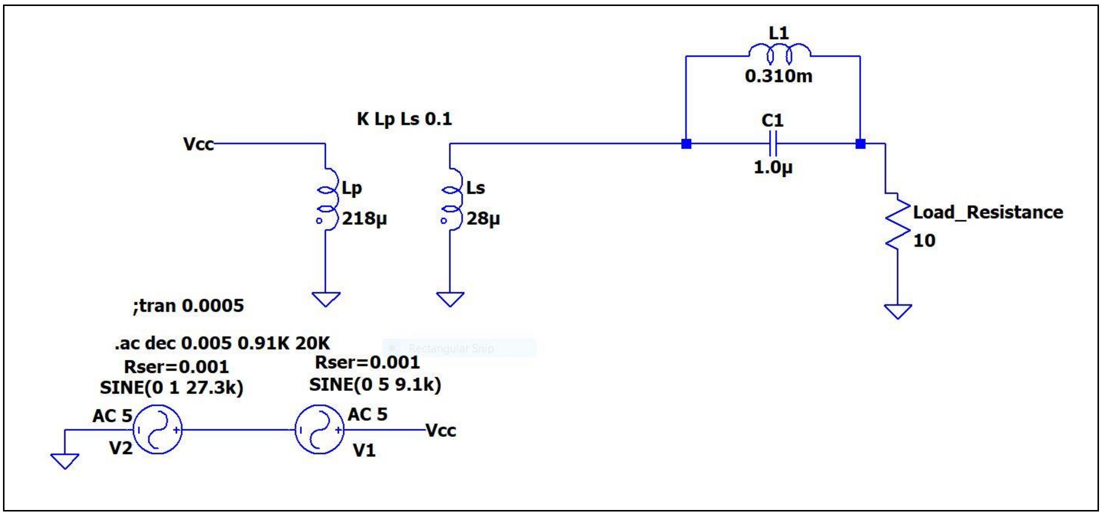

Figure 7.25: Impedance matching circuit for the saddle receive coil of the MPI scanner.

Impedance response of the solenoid receive coil was measured with LCR 8105G meter from 1-20 kHz. It shows the maximum impedance at 9 kHz as presented in Figure 7.26(a). Air core inductor of 310 μH and low equivalent series resistance (ESR) capacitor of 1 μF were utilized to design bandstop filter at 9 kHz. The current through simple resistive load was evaluated in LTSpice as shown in Figure 7.26(b). The coupling frequency component was reduced by -27 dB with a simple resonant filter in the receive chain.

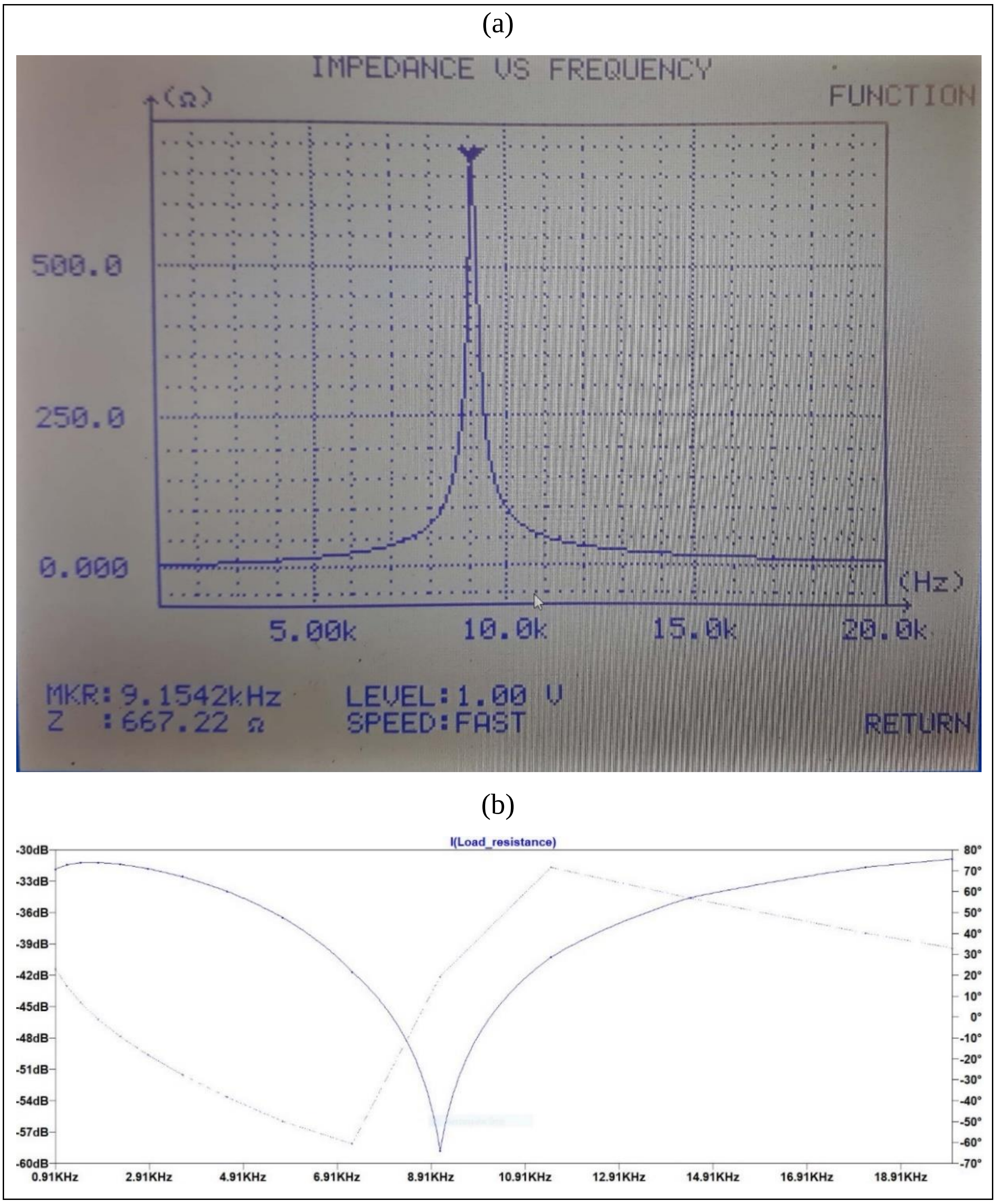

Figure 7.26: Frequency response of the saddle receive chain: (a) Impedance of the receive chain (receive coil and resonance filter) was measured with LCR 8105G meter, (b) Frequency response of receive coil circuit, receive coil shows the maximum current reduction at the resonance frequency (simulated with LTSpice).

7.4.6. Self-Resonance of Saddle Drive and Receive Coil

Optimum excitation frequencies of the drive coils for MPI applications are close to 25kHz. Since MPI is at the pre-clinical stage, a wide range of excitation frequencies are utilized below 100 kHz. In the design of electromagnetic coils for MPI, the issue of self-resonance should be addressed carefully. Practically, each inductor has a stray capacitance parallel to the inductor. Therefore, the self-resonance of the drive coils for MPI applications is at least 10 times higher than the operating frequency (9.0 kHz) [86]. The frequency response of the drive coil is presented in Figure 7.27(a). The self-resonance of 1.01 MHz of the drive coil was measured with an 8105G LCR meter. So, the saddle drive coil does not have any issue of self-resonance. Self-resonance of the receive coil is highly critical because receive coil is used to record multiple harmonics of the excitation frequency. Therefore, a wide bandwidth spectrum is essential for the receive coil. The frequency response of the receive coil is shown in Figure 7.27(b). It is clearly shown that the resonance peak occurred at 3.5 MHz which ensures multiple harmonics that can be recorded up to 3.5 MHz.

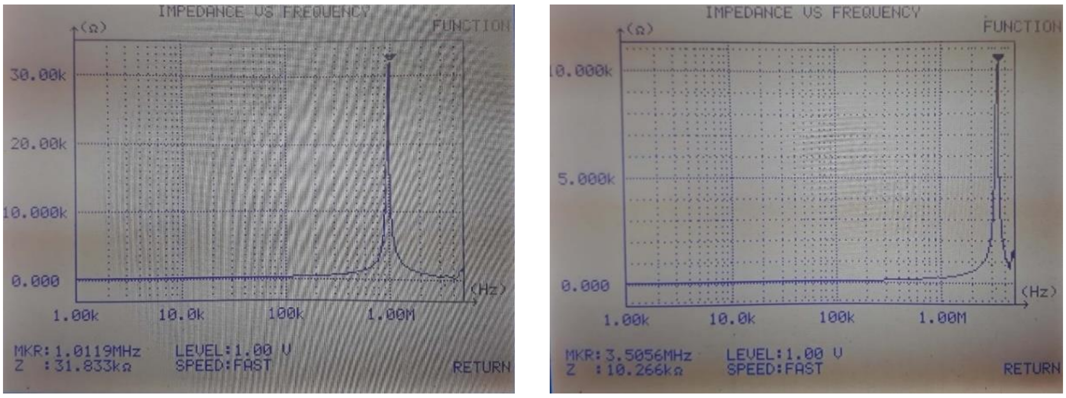
(a) (b)

Figure 7.27: Self-resonance of the saddle coils: (a) Drive coil, (b) Receive coil.

7.5. Scanning Trajectories and Field of View

Acquisition time depends upon the operating sequences and frequencies of the drive coils. The limits of the dynamic FFP movement along a specific axis are defined by the strength of the excitation field (mT) and gradient field (T/m). The selection field presented in section 7.1.1 implemented with a pair of permanent magnets was considered to generate [-3.1, -3.1, 6.2] T/m along x, y, and z-axis respectively. To demonstrate cartesian scanning, 10 mT excitation along the bore axis (x-axis) at 10 kHz was considered as shown in Figure 7.28(a). 2D scanning of the objects is possible if two excitation fields are operated simultaneously. Therefore, a 10 mT excitation field along the higher gradient axis (z-axis) at 1 kHz was considered as shown in Figure 7.28(b).

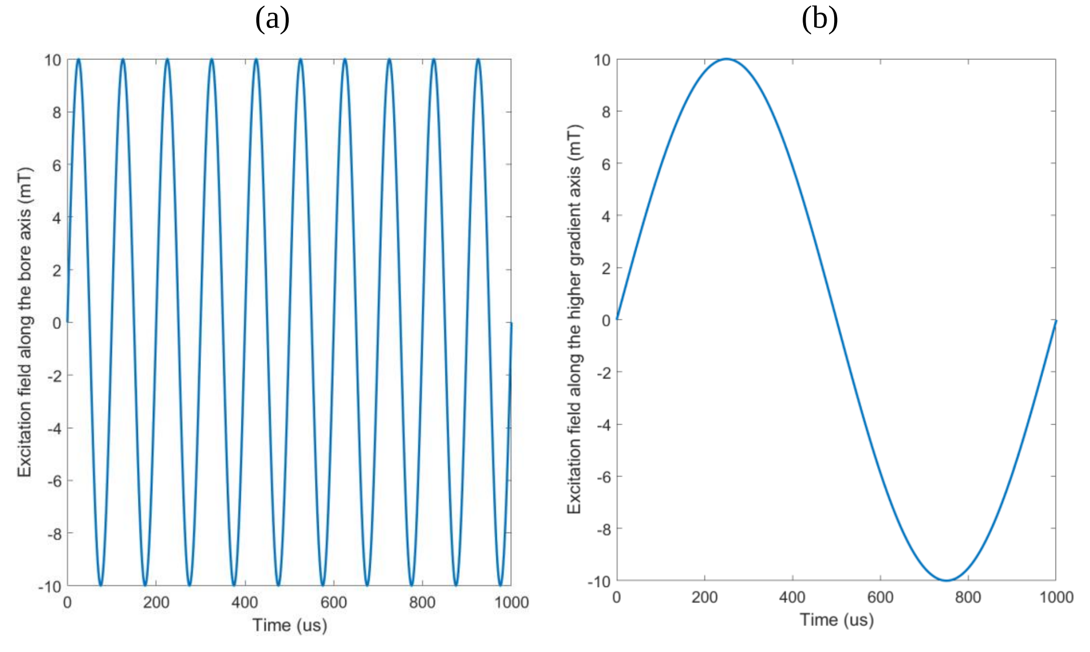

Figure 7.28. Excitation fields for cartesian scanning; (a) Sinusoidal excitation field at 10 kHz along the x-axis, (b) Sinusoidal excitation field at 1 kHz along the z-axis.

The dynamic movement of the FFP is defined by the boundaries of the partial 2D FOV. Partial 2D FOV along the bore axis is [-3.22, +3.22] mm as shown in Figure 7.29. Similarly, partial 2D FOV along the higher gradient field axis is [-1.61, +1.61] mm as shown in Figure 7.29. The frequency of the x-axis drive is ten times higher than the y-axis drive coil. Consequently, the FOV area covered by the combination of both frequencies results in high scanning time due to the slow movement of the y-axis drive coil.

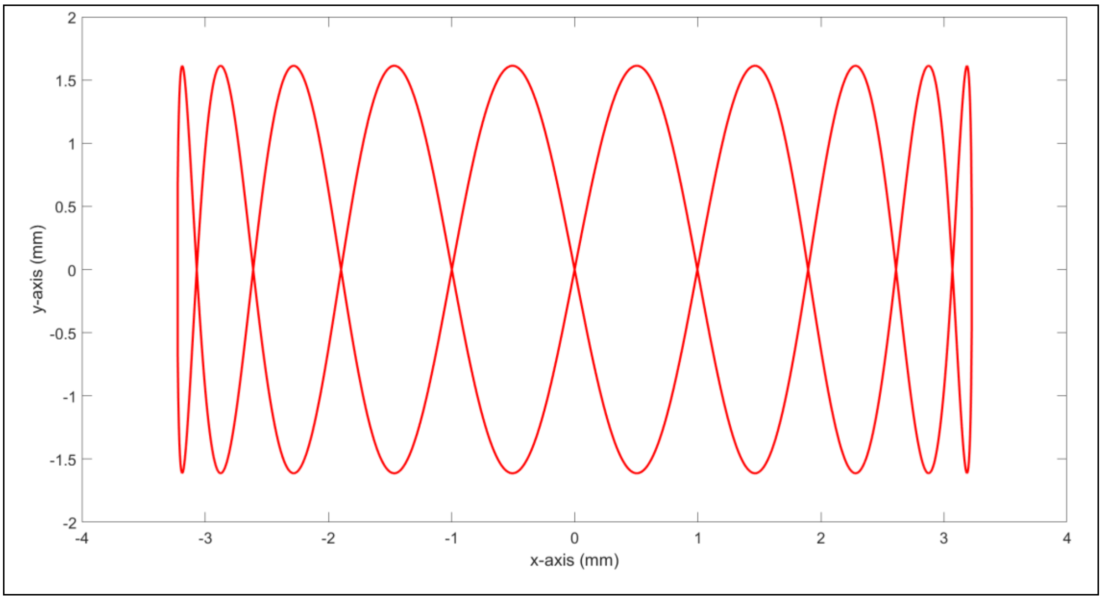

Figure 7.29. 2D partial FOV of cartesian trajectory.

To improve the acquisition time of the covered FOV both drive coils should be operated at high frequencies. Lissajous trajectory provides an opportunity to get scanning in the least possible time. Here, 10 kHz for the x-axis and 9 kHz for the y-axis were chosen for the visualization of the Lissajous trajectory as shown in Figure 7.30.

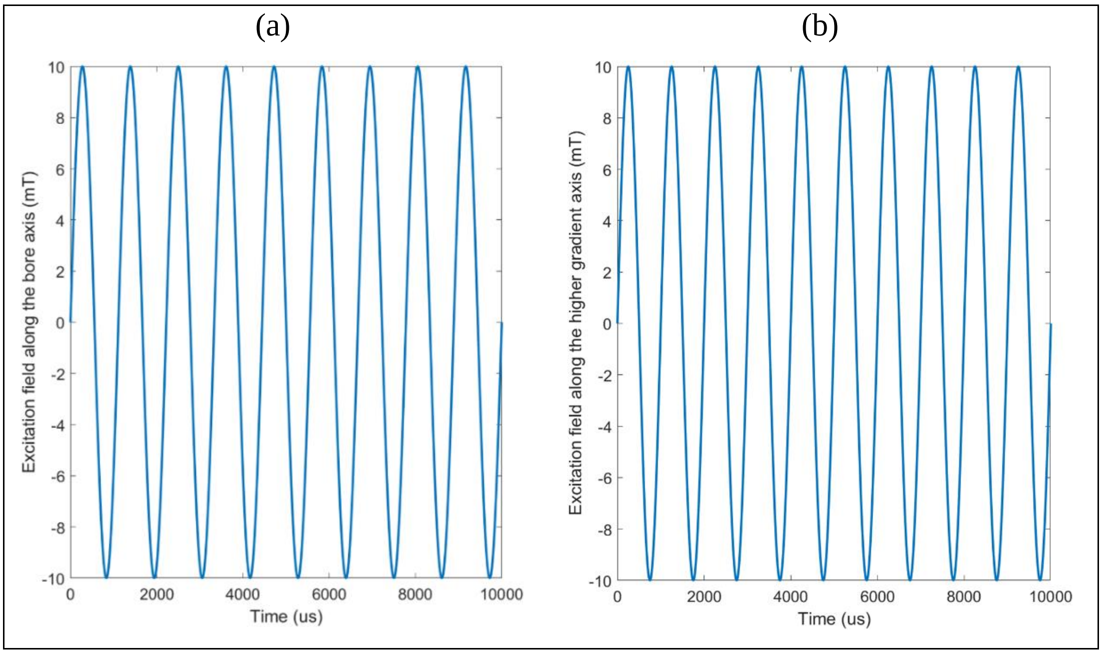

Figure 7.30. Excitation fields for Lissajous scanning; (a) Sinusoidal excitation field at 10 kHz along the x-axis, (b) Sinusoidal excitation field at 9 kHz along the z-axis.

The scanning sequence does not change the extreme limits of the 2D partial FOV as shown in Figure 7.31. The acquisition time of the Lissajous pattern is lower than the cartesian pattern.

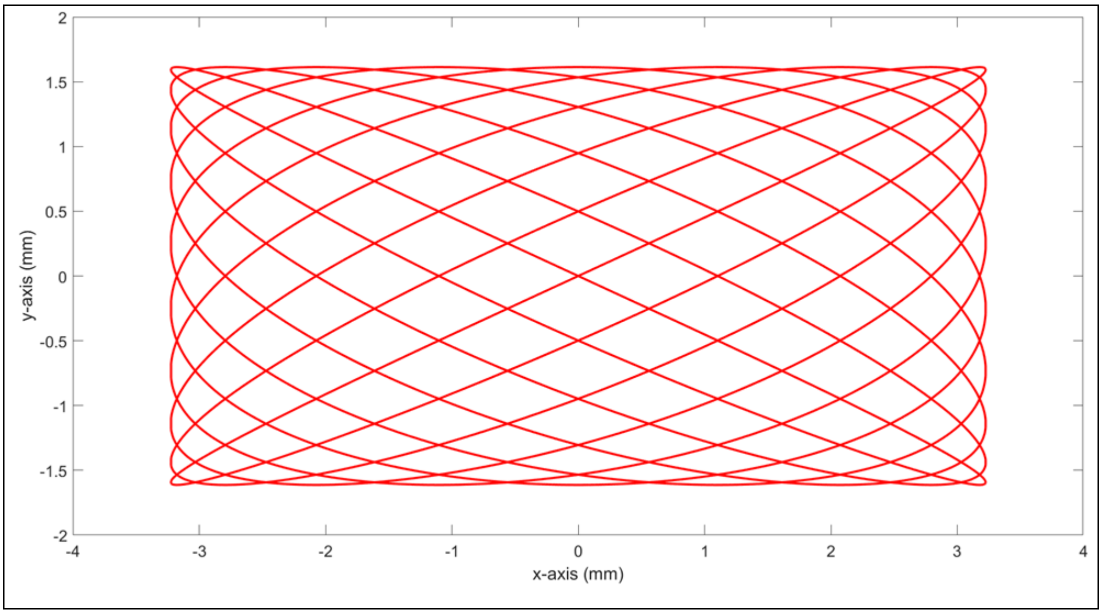

Figure 7.31. 2D partial FOV of the Lissajous trajectory.

8. RESULTS AND RECOMMENDATIONS

Under the scope of this thesis, three prototypes of the MPI scanner were implemented. Initially, numerical simulations of all three devices were carried out with COMSOL Multiphysics. Based on the technical parameters achieved from numerical simulations, their hardware components were constructed. Electronic filters were simulated in LTspice before their integration to the drive and receive coils of all devices. User interfaces were designed in LabView and MATLAB programs to measure sensitivities of the electromagnetic coils and to acquire data. A post-processing algorithm based on X-space was developed in MATLAB for both MPR and MPI scanners.

MPI scanners rely on the magnetic properties of the tracer agents. The response of the MPNs resembles the Langevin function especially the dynamic range is utilized in MPI. In-house MPR was utilized to predict tracer agent behavior in MPI scanner environments. Frequency response provided the 5th/3rd harmonics ratio that should be high to achieve maximum harmonics signals. PSF illustrated the resolution (FWHM, mT) of the SPIONs in response to the sinusoidal excitation field at 4.6 kHz and 9.9 kHz, respectively. This device (i.e., MPR) can easily be adapted at any desired frequency for MPI applications [94]. The relaxation time of the tracer agents was evaluated with MPR. The relaxation time has an inverse relation with excitation frequency. Relative signal of the particle in response to excitation field elaborate the magnetization property. It is a highly significant parameter that was utilized to optimize the synthesis process of new nanoparticles for MPI [95].

In-house MPR is capable to generate a maximum of 20 mT (peak amplitude). So, it cannot fully simulate the expected response of the tracer agents. However, the bias field of higher capacity can be integrated with existing hardware [56]. The evaluation of the selection field effect at any point in the MPI scanners would be feasible with bias field MPR. It has the potential to work as a background signals simulator for MPI scanners.

Next, an in-house MPI scanner with a gradient field of 4.3 T/m was implemented at 9.3 kHz. FFP based spatial encoding was implemented with permanent magnets at an enhanced ratio of 11.25%. Sinusoidal excitation field of 15 mT established the partial FOV from -7 mm to +7 mm along the bore axis (scanning axis). The operating frequency of the MPI scanner was chosen near to the MPR operating frequency to utilize the finding of the MPR device. Two-dimensional phantom images were obtained by integrating a 3D actuator to mechanically translate the scanning objects.

The spatial resolution of the commercially available tracer agents (Perimag and Vivotrax plus) was evaluated at 9.3 kHz. The spatial resolution of the MPI scanners is not only hardware oriented but also affected by tracer agent characteristics. The spatial resolution of the overall PSF for each line was higher than the MPR resolution (FWHM, mT) measurement due to the relaxation time and selection field effects. The relaxation time of the tracer agents causes blurring in MPI images. The MPI image intensity was directly related to iron concentration of the particles similar to the relative signal approach in MPR. The finding of the MPR was in good agreement with the MPI scanner results.

Due to limited FOV, a 3D actuator is inevitable to scan large objects which results in low temporal resolution. Technically FOV can be extended with large excitation fields. However, PNS of the human tissues and SAR of the human body restricts the excitation field [24, 25]. The safe range of the excitation field decreases with an increase in operating frequency. Therefore, FOV can be enhanced with the implementation of focus fields at extremely low frequencies [96]. Overall FOV would be consisting of an array of multiple partial FOVs [97]. The use of a focus field would also speed up the scanning time. It also eliminates the need for mechanical movement along the focus field axis. In addition to this, implementation of the focus field would allow more freedom to apply versatile sequences such as sinusoidal, linear, triangle, and rectangular pulse shaped at low frequencies.

The moderate bore size of the MPI scanner helps to implement a high-sensitive drive and receive coils at low power dissipations. A small-bore size helps to implement receive coil in the proximity of the phantom locations [98]. Similar to the relative signal investigation in MPR, MPI image intensity is dependent on the iron concentration of the sample materials. So, the high sensitivity of the drive and receive coil can pick up signals from low concentrated samples.

Finally, a custom design MPI scanner with 2D FOV was designed and constructed under the scope of this thesis. As compared to the MPI scanner with 1D FOV, bore size, spatial resolution, temporal resolution, and potential applications domain were planned to enhance in an in-house MPI scanner with 2D FOV. Bore size is the highly significant parameter of the MPI scanner that was increased by almost two times. A higher gradient field of 6.2 T/m was implemented with permanent magnets to improve the spatial resolution of the MPI scanner with 2D FOV. Instead of a line scanning with a former MPI scanner, two drive and receive coil systems were integrated to partially scan the 2D area directly. Fundamentally, cartesian and Lissajous scanning trajectories would speed up the scanning time as compared to mechanical movements with 3D actuators.

As the bore size was increased, the sensitivities of the drive and receive coils were reduced that affect the sensitivity of the MPI scanner with 2D FOV. Fortunately, the sensitivities can be compensated with higher operating frequencies such as 25 kHz which is considered as an optimum frequency for MPI applications. FOVs along the bore axis (solenoid drive coil) and along the higher gradient axis (saddle drive coil) were reduced significantly due to the higher gradient field. The integration of a 3D actuator is inevitable to scan large objects or phantoms at the cost of temporal resolution. The objects can be dragged from the fixed FOV with mechanical movement. However, the implementation of focus fields along the excitation fields axes could eliminate the mechanical movement setup. Overall, 2D FOV would be generated from multiple partial FOVs like grid and each box will represent the partial 2D FOV.

The temporal resolution would be increased with 2D FOV as compared to 1D FOV for limited scanning regions. As the scanning region can be extended with the implementation of the focus fields. It also helps to improve the temporal resolution of the MPI scanner with 2D FOV. In addition to this, scanning sequences such as Lissajous trajectory produce high temporal resolution as compared to cartesian trajectory.

FFP based spatial encoding implemented with permanent magnets was followed throughout this thesis. As the size of the MPI scanners increases it is quite difficult to design a selection field with permanent magnets. So, electromagnetic coils are a more appropriate substitute for the implementation of even adjustable selection fields.

Lastly, a medium bore size of the MPI scanner with 2D FOV would open a window for new applications in addition to phantom imaging [99]. In-vitro scanning and in-vivo scanning for small-scale animals such as rats and mice are the potential applications for the MPI scanner with 2D FOV.

REFERENCES

[1] Gleich B., Weizenecker J., (2005), “Tomographic imaging using the nonlinear response of magnetic particles”, Nature, 435, 1214–1217.

[2] Gleich B., (2013), “Principles and applications of magnetic particle imaging”, Doctoral Thesis, University of Lübeck.

[3] Bauer L.M., (2016), “Magnetic nanoparticle characterization for imaging and therapeutic applications”, Doctoral Thesis, Case Western Reserve University.

[4] Bringout G., (2016), “Field Free Line Magnetic Particle Imaging Characterisation and imaging device up-scaling”, Doctoral Thesis, University of Lübeck.

[5] Pablico-Lansigan M. H., Situ S. F., Samia A. C. S., (2013), “Magnetic particle imaging: advancements and perspectives for real-time in vivo monitoring and image-guided therapy”, Nanoscale, 5, 4040-4045.

[6] Massoud T. F., Gambhir S. S., (2003), “Molecular imaging in living subjects: seeing fundamental biological processes in a new light”, Genes and Development, 17, 545–580.

[7] Weizenecker J., Borgert J., Gleich B., (2007), “A simulation study on the resolution and sensitivity of magnetic particle imaging”, Phys. Med. Biol., 52, 6363-6374.

[8] Kherlopian A. R., Song T., Duan Q., Neimark M. A., Po M. J., Gohagan J. K., Laine A. F., (2008), “A review of imaging techniques for systems biology”, BMC Syst Biol., 2 (74), 18700030 .

[9] Weissleder R., (2002), “Scaling down imaging: molecular mapping of cancer in mice”, Nat Rev Cancer, 2, 11–18.

[10] Cox B., Beard P., (2015), “Imaging techniques: super-resolution ultrasound”, Nature, 527, 451–452.

[11] Zheng B., Vazin T., Goodwill P. W., Conway A., Verma A., Saritas E. U., et al., (2015), “Magnetic Particle Imaging tracks the long-term fate of in vivo neural cell implants with high image contrast”, Sci. Rep., 5, 14055.

[12] Nguyen P. K., Riegler J., Wu J. C., (2014), “Stem cell imaging: from bench to bedside”, Cell Stem Cell, 14, 431–444.

[13] Zheng B., See M. P. V., Yu E., Gunel B., Lu K., Vazin T., et al., (2016), “Quantitative magnetic particle imaging monitors the transplantation biodistribution, and clearance of stem cell In Vivo”, Theranostics, 6, 291–301.

[14] Weizenecker J., Gleich B., Rahmer J., Dahnke H., Borgert J., (2009), “Three-dimensional real-time in vivo magnetic particle imaging”, Phys. Med. Biol., 54, L1-L10.

[15] Knopp T., Buzug T. M., (2012), “Magnetic particle imaging: an introduction to imaging principles and scanner instrumentation”, Springer Heidelberg New York Dordrecht London.

[16] Goodwill P. W., Saritas E. U., Croft L. R., Kim T. N., Krishnan K. M., Schaffer D. V., Conolly S. M., (2012), “X-space MPI: magnetic nanoparticles for safe medical imaging”, Adv. Mater., 24, 3870-3877.

[17] Saritas E. U., Good P. W., Croft L. R., Konkle J. J., Lu K., Zheng B., Conolly S. M., (2013), “Magnetic particle imaging (MPI) for NMR and MRI researchers”, 229, 116-126.

[18] Bauer L. M., Situ S. F., Griswold M. A., Samia A. C. S., (2015), “Magnetic particle imaging tracers: state-of-the-art and future directions”, J. Phys. Chem. Lett., 6, 2509–2517.

[19] Song G., Chen M., Zhang Y., Cui L., Qu H., Zheng X., Wintermak M., Liu Z., Rao J., (2018), “Janus iron oxides @ semiconducting polymer nanoparticle tracer for cell tracking by magnetic particle imaging”, Nano Lett., 18, 182-189.

[20] Tay Z. W., Chandrasekharan P., Zhou X. Y., Yu E., Zheng B., Conolly S., (2018), “In vivo tracking and quantification of inhaled aerosol using magnetic particle imaging towards inhaled therapeutic monitoring”, Theranostics, 8(13), 3676-3687.

[21] Tay Z. W., Chandrasekharan P., Chiu-Lam A., Hensley D. W., Dhavalikar R., Zhou X. Y. et al., (2018), “Magnetic particle imaging-guided heating in vivo using gradient fields for arbitrary localization of magnetic hyperthermia therapy”, ACS Nano, 12(4), 3699–3713.

[22] Murase K., Aoki M., Banura N., Nishimoto K., Mimura A., Kuboyabu T., Yabata I., (2015), “Usefulness of magnetic particle imaging for predicting the therapeutic effect of magnetic hyperthermia”, Open J. of Med. Imaging, 05(2), 85-99.

[23] Schmale I., Gleich B., Schmidt J., Rahmer J., Bontus C., Eckart R. et al., (2013), “Human PNS and SAR study in the frequency range from 24 to 162 kHz”, IWMPI, California, USA, 23-24 March.

[24] Saritas E. U., Goodwill P. W., Zhang G. Z., Conolly S. M., (2013), “Magnetostimulation limits in magnetic particle imaging”, IEEE Trans. Med. Imaging”, 32(9), 1600–1610.

[25] Saritas E. U., Goodwill P. W., Conolly S. M., (2015), “Effects of pulse duration on magnetostimulation thresholds”, Med. Phys., 42(6), 3005–3012.

[26] Rahmer J., Geleich B., Schmidt J., Bontus C., Kanzenbach J., Borget J., (2011), "Increased volume coverage in 3D magnetic particle imaging", ISABEL '11: proceedings of the 4th international symposium on applied sciences in biomedical and communication, 132, 1-5, Barcelona, Spain, 26-29 October.

[27] Grüttner M., Knopp T., Franke J., Heidenreich M., Rahmer J., Halkola A. et al., (2013), "On the formulation of the image reconstruction problem in magnetic particle imaging", Biomed. Tech., 58 (6), 583–591.

[28] Goodwill P.W., Conolly S. M., (2011), "Multidimensional X-space magnetic particle imaging", 30 (9), 1581–1590.

[29] Lassenberger A., Scheberl A., Stadlbauer A., Stiglbauer A., Helbich T., Reimhult E., (2017), "Individually stabilized, superparamagnetic nanoparticles with controlled shell and size leading to exceptional stealth properties and high relaxivities", ACS Appl. Mater. Interfaces, 9 (4), 3343–3353.

[30] Bae K. H., Park M., Do M. J., Lee N., Ryu J. H., Kim G. W. et al., (2012), "Chitosan oligosaccharide-stabilized ferrimagnetic iron oxide nanocubes for magnetically modulated cancer hyperthermia", ACS Nano, 6 (6), 5266–5273.

[31] Kolen'Ko Y. V., Banobre-Lopez M., Rodriguez-Abreu C., Carbo-Argibay E., Sailsman A., Pineiro-Redondo Y. et al., (2014), "Large-scale synthesis of colloidal Fe3O4 nanoparticles exhibiting high heating efficiency in magnetic hyperthermia", J. Phys. Chem. C, 118 (16), 8691–8701.

[32] Wang Q., Chen B., Cao M., Sun J., Wu H., Zhao P. et al., (2016), "Response of MAPK pathway to iron oxide nanoparticles in vitro treatment promotes osteogenic differentiation of hBMSCs", Biomaterials, 86, 11–20.

[33] Son B., Kim H. D., Kim M., Kim J. A., Lee J. Shen H. et al., (2015), "Physical stimuli-induced chondrogenic differentiation of mesenchymal stem cells using magnetic nanoparticles", Adv. Healthc. Mater., 4 (9), 1339–1347.

[34] Huong L. T. T., Nam N. H., Doan D. H., Nhung H. T. M., Quang B. T., Nam P. H. et al., (2016), "Folate attached, curcumin loaded Fe3O4 nanoparticles: a novel multifunctional drug delivery system for cancer treatment", Mater. Chem. Phys., 172, 98–104.

[35] Zhang D., Wang J., Wang Z., Wang R., Song L., Zhang T. et al., (2015), "Polyethyleneimine-coated Fe3O4 nanoparticles for efficient siRNA delivery to human mesenchymal stem cells derived from different tissues", Sci. Adv. Mater., 7 (6), 1058–1064.

[36] Lara V. P., Caramelli P., Teixeira A. L., Barbosa M. T., Carmona K. C., Carvalho M. G. et al., (2013), "High cortisol levels are associated with cognitive impairment no-dementia (CIND) and dementia", Clin. Chim. Acta, 423, 18–22.

[37] Kim T., Momin E., Choi J., Yuan K., Zaidi H., Kim J. et al., (2011), “Mesoporous silica-coated hollow manganese oxide nanoparticles as positive T_1 contrast agents for labeling and MRI tracking of adipose-derived mesenchymal stem cells”, J. Am. Chem. Soc., 133 (9), 2955–2961.

[38] Palanisamy S., Wang Y. M., (2019), “Superparamagnetic iron oxide nanoparticulate system: Synthesis, targeting, drug delivery and therapy in cancer”, Dalt. Trans., 48 (26), 9490–9515.

[39] Chandrasekharan P., Tay Z. W., Zhou X. Y., Yu E., Orendorff R., Hensley D. et al., (2018), “A perspective on a rapid and radiation-free tracer imaging modality, magnetic particle imaging, with promise for clinical translation”, Br. J. Radiol., 91 (1091), 1–14.

[40] Kratz H., Mohtashamdolatshahi A., Eberbeck D., Kosch O., Hauptmann R., Wiekhorst F. et al., (2019), “Mpi phantom study with a high-performing multicore tracer made by coprecipitation”, Nanomaterials, 9 (10), 1466.

[41] Bauer L. M., Hensley D. W., Zheng B., Tay Z. W., Goodwill P. W., Griswold M. A., Conolly S. M., (2016), “Eddy current-shielded x-space relaxometer for sensitive magnetic nanoparticle characterization”, Rev. Sci. Instrum., 87, 055109.

[42] Eberbeck D., Dennis C. L., Huls N. F., Krycka K. L., Gruttner C., Westphal F., (2013), “Multicore magnetic nanoparticles for magnetic particle imaging”, IEEE Trans. Magn., 49 (1), 269–274.

[43] Witte K., Gruttner C., Westphal F., (2017), “ Magnetic nanoparticles as tracers for magnetic particle imaging (MPI) ”, micromod Partikeltechnologie GmbH.

[44] Keselman P., Yu E. Y., Zhou X. Y., Goodwill P. W., Chandrasenkharan P., Ferguson R. M. et al., (2017), “Tracking short-term biodistribution and long-term clearance of SPIO tracers in magnetic particle imaging”, Phys. Med. Biol., 62, 3440-3453.

[45] Khandhar A. P., Ferguson R. M., Krishnan K. M., (2013), “Monodisperse magnetite nanoparticle tracers for in vivo magnetic particle imaging”, Biomaterials., 34 (15), 3837-3845.

[46] Reimer P., Balzer T., (2003), “Ferucarbotran (Resovist): a new clinically approved RES-specific contrast agent for contrast-enhanced NRI of the liver:properties, clinical development, and applications”, Eur. Radiol., 13, 1266-1276.

[47] Cao, D., Li, H., Wang, X., Jing, P., et al., (2016), “High saturation magnetization of γ-Fe2O3 nanoparticles by a facile one-step synthesis approach”, Sci. Rep., 6, 32360.

[48] Chikazumi S., Charap S.H., (1978), “Physics of Magnetism”, Krieger Pub Co.

[49] Shliomis M. I., (1972), “Effective viscosity of magnetic suspensions”, Sov.Phys.-JETP, 34 (6), 1291–1294.

[50] Shliomis M. I., (1974), “Magnetic fluids”, Sov.Phys.-Uspekhi, 17 (3), 153–159.

[51] Dieckhoff J., Eberbeck D., Schilling M., Ludwig F., (2016), “Magnetic-field dependence of Brownian and Néel relaxation times”, J. Appl. Phys., 119 (4), 043903.

[52] Deissler R. J., Wu Y., Martens M. A., (2014), “Dependence of brownian and neel relaxation times on magnetic field strength”, Med. Phys., 41 (1), 012301-12 .

[53] Brown W. F., (1963), “ Thermal Fluctuations of a single-domain particle”, Physical Review, 130 (5), 1677-1686.

[54] Yoshida T., Enpuku K., (2009), “Simulation and quantitative clarification of AC susceptibility of magnetic fluid in nonlinear Brownian relaxation region,” Jpn. J. Appl. Phys., 48, 127002-7.

[55] Irfan M., Dogan N., Sapmaz T., Bingolbali A., (2021) “Development of MPI relaxometer for characterization of superparamagnetic nanoparticles”, J. Magn. Magn. Mater., 536 (1), 168082.

[56] Croft L.R., Goodwill P. W., Conolly S. M., (2012), “Relaxation in x-space magnetic particle imaging” IEEE Trans. Med. Imaging, 31 (12), 2335-2342.

[57] Irfan M., Dogan N., Bingolbali A., Aliew F., (2021), “Synthesis and characterization of NiFe2O4 magnetic nanoparticles with different coating materials for magnetic particle imaging (MPI)”, J. Magn. Magn. Mater., 537 (4), 168150.

[58] Almásy L., Creanga D., Nadejde C., Rosta L., Pomjakushina E., Ursache-Oprisan M., (2015), “Wet milling versus co-precipitation in magnetite ferrofluid preparation”, J. Serbian Chem. Soc., 80 (3), 367–376.

[59] Almessiere M.A., Slimani Y., El Sayed H. S., Baykal A., (2018), “Ca^{2+} and Mg^{2+} incorporated barium hexaferrites: structural and magnetic properties”, J. Sol-Gel Sci. Technol., 88 (3), 628–638.

[60] Slimani Y., Almessiere M. A., Nawaz M., Baykal A., Akhtar S., Ercan I., Belenli I., (2019), “Effect of bimetallic (Ca, Mg) substitution on magneto-optical properties of NiFe2O4 nanoparticles”, Ceram. Int., 45 (5), 6021–6029.

[61] Kamble R. B., Varade V., Ramesh K. P., Prasad V., (2015), “Domain size correlated magnetic properties and electrical impedance of size dependent nickel ferrite nanoparticles”, AIP Adv., 5 (1), 017119-13.

[62] Fannin P. C., (2003), “Investigating magnetic fluids by means of complex susceptibility measurements”, J. Magn. Magn. Mater., 258–259, 446–451.

[63] Nikolo M., (1995), “Superconductivity: a guide to alternating current susceptibility measurements and alternating current susceptometer design”, Am. J. Phys., 63 (1), 57–65.

[64] Utkur M., Muslu Y., Saritas E. U., (2019), “Relaxation-based color magnetic particle imaging for viscosity mapping”, Appl. Phys. Lett., 115 (15), 152403-5.

[65] Wu K., Schliep K., Zhang X., Liu J., Ma B., Wang J. P., (2017), “Characterizing physical properties of superparamagnetic nanoparticles in liquid phase using brownian relaxation”, Small, 13 (22), 1–7.

[66] Goodwill P. W., Tamrazian A., Croft L. R., Lu C. D., Johnson E. M., Pidaparthi R. et al., (2011), “Ferrohydrodynamic relaxometry for magnetic particle imaging”, Appl. Phys. Lett., 98 (26), 4–7.

[67] Bozkurt E., Utkur M., Muslu Y., Saritas E. U., (2017), “Manyetik parçacık görüntüleme'de eksitasyon alanı parametrelerinin ekkisi:bir relaksometre çalışması(Effect of drive field parameters in magnetic particle imaging: a relaxometer study)”, 21st National Biomedical Engineering Meeting (BIYOMUT), Istanbul, Turkey, 24-26 November.

[68] Croft L. R., Goodwill P. W., Konkle J. J., (2016), “Low drive field amplitude for improved image resolution in magnetic particle imaging”, Med. Phys., 43 (1), 424–435.

[69] Top C. B., (2020) “An arbitrary waveform magnetic nanoparticle relaxometer with an asymmetrical three-section gradiometric receive coil”, Turkish J. Electr. Eng. Comput. Sci., 28 (3), 1344–1354.

[70] Gleich B., Weizenecker J., Borgert J., (2008), “Experimental results on fast 2D-encoded magnetic particle imaging”, Phys. Med. Biol., 53 (6), N81-N84.

[71] Erbe M., Knopp T., Sattel T. F., Biederer S., Buzug T. M., (2011), “Experimental generation of an arbitrarily rotated field-free line for the use in magnetic particle imaging”, Med. Phys., 38(9), 5200–5207.

[72] Weizenecker J., Gleich B., Borgert J., (2008), “Magnetic particle imaging using a field free line”, J. Phys. D. Appl. Phys., 41 (10), 105009.

[73] Pantke D., Holle N., Mogarkar A., Straub M., Schulz V., (2019), “Multifrequency magnetic particle imaging enabled by a combined passive and active drive field feed-through compensation approach”, Med. Phys., 46 (9), 4077-4086.

[74] Konkle J. J., Goodwill P. W., Hensley D. W., Orendorff R. D., Lustig M., Conolly S. M., (2015), “A convex formulation for magnetic particle imaging X-space reconstruction”, PLoS One, 10 (10), e140136.

[75] Schilling M., Ludwig F., Kuhlmann C., Wawrzik T., (2013), “Magnetic particle imaging scanner with 10-kHz drive-field frequency”, Biomed. Tech., 58 (6), 557–563.

[76] Goodwill P. W., Konkle J. J., Zheng B., Saristas E. U., Conolloy S. M., (2012), “Projection x-space magnetic particle imaging”, IEEE Trans. Med. Imaging, 31 (5), 1076-1085.

[77] Rahmer J., Weizenecker J., Gleich B., Borgert J., (2009), “Signal encoding in magnetic particle imaging: Properties of the system function”, BMC Med. Imaging, 9 (4), 1–21.

[78] Top C. B., Ilbey S., Güven H. E., (2017), “Electronically rotated and translated field-free line generation for open bore magnetic particle imaging:,” Med. Phys., 44 (12), 6225–6238.

[79] Chou C. Y., Ferrage F., Aubert G., Sakellariou D., (2015), “Simple method for the generation of multiple homogeneous field volumes inside the bore of superconducting magnets”, Sci. Rep., 5, 12200.

[80] Basharat M., Ding M., Cai H., Li Y., Fang J., (2017), “Design and Analysis of Multilayer Solenoid Coil for Faraday Modulator”, MATEC Web Conf., 114, 04004.

[81] Schenck J. F., (2000), “Safety of strong, static magnetic fields”, J. Magn. Reson. Imaging, 12 (1), 2–19.

[82] Saritas E. U., Goodwill P. W., Zhang G. Z., Yu W., Conolly S. M., (2012),“Safety limits for human-size magnetic particle imaging systems”, Springer Proc. Phys., 140, 325–330.

[83] Vogel P., Ruckert M. A., Klauer P., Kullmann W. H., Jakob P. M., Behr V. C., (2014), “Traveling wave magnetic particle imaging”, IEEE Trans. Magn., 51 (2), 401-407.

[84] Sattel T. F., Knopp T., Biederer S., Gleich B., Weizerecker J., Borgert J., Buzug T. M, (2009), “Single-sided device for magnetic particle imaging,” J. Phys. D. Appl. Phys., 42 (2), 022001.

[85] Irfan M., Mercan Dogan O., Dogan N., Bingolbali A., (2020), “Position dependent response of Magnetic Nanoparticles using Magnetic Particle Imaging (MPI)”, 2020 Medical Technologies Congress (TIPTEKNO), 1-4, Antalya, Turkey, 19-20 November.

[86] Hoshino Y., (2009), “Tips for coil users”, SAGAMI ELEC Co Ltd, 20091221A, 1–35.

[87] Lu K., Goodwill P. W., Saritas E. U., Zheng B., Conolly S. M., (2013), “Linearity and shift invariance for quantitative magnetic particle imaging”, IEEE Trans. Med. Imaging, 32 (9), 1565–1575.

[88] Knopp T., Biederer S., Sattel T. F., Rahmer J., Weizenecker J., Gleich B. et al., (2010), “2D model-based reconstruction for magnetic particle imaging”, Med. Phys., 37 (2), 485–491.

[89] Knopp T., Sattel T. F., Biederer S., Rahmer J., Weizenecker J., Gleich B., Borgert J., Buzug T. M., (2010), “Model-based reconstruction for magnetic particle imaging”, IEEE Trans. on Med. Imaging, 29 (1), 12-18.

[90] Gräser M., Biederer S., Grüttner M., Wojtczyk H., Tenner W., Sattel T. F. et al., (2011), “Determination of a 1D-MPI-system-function using a magnetic particle spectroscope”, biomedical tech., 56, Lübeck, Germany, 3 March.

[91] Grüttner M., Gräser M., Biederer S., Sattel t. F., Wojtczyk H., Tenner W. et al., (2011), “1D -image reconstruction for magnetic particle imaging using a hybrid system function”, IEEE Nuclear Science Symposium Conference Record, 2545-2548, Valencia, Spain, 23-29 October.

[92] Halkola A., Buzug T., Rahmer J., Gleich B., Bontus C., (2012), “System calibration unit for magnetic particle imaging: focus field based system function”, Springer Proceeding in Physics, 140, 27-31.

[93] Lu K., Goodwill P. W., Zheng B., Conolly S., (2011), “The impact of filtering direct-feedthrough on the x-space theory of magnetic particle imaging”, Medical Imaging: biomedical applications in molecular, structural, and funcation imaging, 79652I, Florida, United States, 15 March.

[94] Kuhlmann C., Khandhar A. P., Ferguson R. M., Kemp S., Wawrzik T., Schilling M., et al., (2015), “Drive-field frequency dependent MPI performance of single-core magnetic nanoparticle tracers,” IEEE Trans. on Magnetics, 51 (2), 6500504.

[95] Malhotra A., Von Gladiss A., Behrends A., Friedrich T., Neumann A., Buzug T. M., Lüdtke-Buzug K., (2019), “Tracking the Growth of Superparamagnetic Nanoparticles with an In-Situ Magnetic Particle Spectrometer (INSPECT)”, Sci. Rep., 9, 10538.

[96] Gleich B., Weizenecker J., Timminger H., Bontus C., Schmale I., Rahmer J., Schmidt J., Kanzenbach J., Borgert J., (2010), “Fast MPI demonstrator with enlarged field of view”, Proc. ISMRM, 18, 218, Stockholm, Sweden, 1 May.

[97] Schmale I., Rahmer J., Gleich B., Kanzenbach J., Schmidt J., Bontus C., Woywode O., Borgert J. (2011), “First phantom and in vivo MPI images with an extended field of view”, Medical Imaging 2011: Biomedical Applications in Molecular, Structural, and Functional Imaging, 7965, 796510, Florida, USA, 9 March.

[98] Kosch O., Paysen H., Wells J., Ptach F., Franke J., Wockel L., Dutz S., Wiekhorst F., (2019), “Evaluation of a separate-receive coil by magnetic particle imaging of a solid phantom”, Journal of Magnetism and Magnetic Materials, 471, 444-449.

[99] Hensley D., Tay Z. W., Dhavalikar R., Zheng B., Goodwill P., Rinaldi C., Conolly S., (2017), “Combining magnetic particle imaging and magnetic fluid hyperthermia in a theranostic platform”, Phys. Med. Biol., 62, 3483-3500.

[100] Irfan M., Mossa H., Dogan N., (2021), “Analog filters for Enhanced Signal Reception of Magnetic Particle Imaging (MPI) Scanner”, 2021 Medical Technologies Congress (TIPTEKNO), 1-4, Antalya, Turkey, 04-06 November.

BIOGRAPHY

Muhammad Irfan completed his undergraduate studies in Electronics (Electrical) Engineering at COMSATS University Islamabad (Abbottabad Campus), Pakistan in 2013. He started his master's studies in Electro-Optical systems Engineering at Kocaeli University in 2014 and completed it in 2016. In the same year, he started his Ph.D. studies at Electronics Engineering of Graduate School of Natural and Applied Sciences at Gebze Technical University. He worked in “Development of the Medical Imaging Device Based on Magnetic Particle Imaging (MPI)”, TUBITAK (Grant No: 115E776 & 115E777) projects between June 2018-November 2021. During his Ph.D. studies, he got thorough experience in Magnetic Particle Imaging techniques for medical applications.

APPENDICES

Appendix A: Publications Within the Scope of Thesis Study

Irfan M., Mercan Dogan O., Dogan N., Bingolbali A., (2019), “Modeling and Simulation of Wide Range Homogeneous Selection Field for 3D MPI Scanner”, American Association of Physicists in Medicine (AAPM), 46 (6), 141-142, Texas, USA, 14 - 18 July.

Irfan M., Mercan Dogan O., Dogan N., Bingolbali A., (2020), “Position dependent response of Magnetic Nanoparticles using Magnetic Particle Imaging (MPI)”, 2020 Medical Technologies Congress (TIPTEKNO), 1-4, Antalya, Turkey, 19-20 November.

Irfan M., Dogan N., Bingolbali A., (2021), “Magnetic Particle Spectrometer for Diagnosis of Magnetic Nanoparticles”, American Association of Physicists in Medicine (AAPM), 48 (6), 393, Virginia, USA, 25 - 29 July.

Balcı F., Bingolbali A., Dogan N., Irfan M., (2021), “Optimization of Fill Factor Equation in Halbach Design”, Tech. Phys. Lett., 47, 158–161.

Irfan M., Dogan N., Bingolbali A., Sapmaz T., (2021), “Development of MPI relaxometer for characterization of superparamagnetic nanoparticles”, Journal of Magnetism and Magnetic Materials, 536, 168082.

Irfan M., Dogan N., Bingolbali A., Aliew F., (2021), “Synthesis and characterization of NiFe2O4 magnetic nanoparticles with different coating materials for magnetic particle imaging (MPI)”, Journal of Magnetism and Magnetic Materials, 537, 168150.

Irfan M., Mossa H., Dogan N., (2021), “Analog filters for Enhanced Signal Reception of Magnetic Particle Imaging (MPI) Scanner”, 2021 Medical Technologies Congress (TIPTEKNO), 1-4, Antalya, Turkey, 04-06 November.

Appendix B: Magnetic Particle Relaxometer (MPR) axiliary data

Table B1. 1: Odd Harmonics of MPR at 9.9 kHz.

	Vivotrax			Perimag			Synomag		
Frequency (kHz)	5 mT	10 mT	15 mT	5 mT	10 mT	15 mT	5 mT	10 mT	15 mT
29.7	1.000	1.000	1.000	1.000	1.000	1.000	1.000	1.000	1.000
49.5	0.326	0.384	0.448	0.369	0.511	0.598	0.316	0.467	0.572
69.3	0.135	0.201	0.224	0.160	0.291	0.378	0.114	0.240	0.335
89.1	0.061	0.130	0.141	0.076	0.181	0.256	0.044	0.135	0.208
108.9	0.028	0.086	0.105	0.039	0.119	0.183	0.018	0.081	0.138
128.7	0.013	0.057	0.082	0.020	0.081	0.136	0.009	0.049	0.096
148.5	0.006	0.038	0.064	0.011	0.056	0.104	0.005	0.031	0.069
168.3	0.004	0.026	0.049	0.006	0.040	0.082	0.003	0.020	0.050
188.1	0.003	0.016	0.033	0.003	0.025	0.057	0.001	0.011	0.033

Table B1. 2: Odd Harmonics of MPR at 4.6 kHz.

	Vivotrax			Perimag			Synomag		
Frequency (kHz)	5 mT	10 mT	15 mT	5 mT	10 mT	15 mT	5 mT	10 mT	15 mT
13.8	1.000	1.000	1.000	1.000	1.000	1.000	1.000	1.000	1.000
23.0	0.316	0.346	0.431	0.387	0.536	0.621	0.299	0.446	0.564
32.2	0.136	0.179	0.201	0.170	0.316	0.405	0.114	0.232	0.331
41.4	0.064	0.119	0.121	0.079	0.201	0.280	0.045	0.134	0.210
50.6	0.032	0.081	0.091	0.036	0.132	0.201	0.019	0.081	0.141
59.8	0.016	0.054	0.073	0.016	0.090	0.149	0.008	0.049	0.098
69.0	0.008	0.035	0.057	0.008	0.061	0.112	0.004	0.030	0.069
78.2	0.004	0.023	0.044	0.006	0.042	0.085	0.002	0.019	0.049
87.4	0.001	0.012	0.027	0.005	0.025	0.055	0.001	0.010	0.030